FINAL REPORT

Superconducting Magnetic Tensor Gradiometer System for Detection of Underwater Military Munitions

SERDP Project MR-1661

JUNE 2012

Stephen Billings
Sky Research, Inc.

This document has been cleared for public release

SERDP
DOD ▪ EPA ▪ DOE

This report was prepared under contract to the Department of Defense Strategic Environmental Research and Development Program (SERDP). The publication of this report does not indicate endorsement by the Department of Defense, nor should the contents be construed as reflecting the official policy or position of the Department of Defense. Reference herein to any specific commercial product, process, or service by trade name, trademark, manufacturer, or otherwise, does not necessarily constitute or imply its endorsement, recommendation, or favoring by the Department of Defense.

Contents

CONTENTS ..... **III**

FIGURES v
TABLES x

1 EXECUTIVE SUMMARY **1**

2 EXTENDED SUMMARY **3**

3 INTRODUCTION **13**

4 BACKGROUND **13**

5 PLANAR GRADIOMETER **14**

5.1 FLIP-CHIP GRADIOMETER USING S-SHAPED COUPLING COIL 15
5.2 DEVICE FABRICATION AND CHARACTERISATION 17
5.3 GRADIOMETER DESIGN AND SPECIFICATIONS 21
5.3.1 The readout gradiometer *21*
5.3.2 Flip-chip antenna *27*
5.4 DESIGN C 32
5.4.1 Electrical connection *34*
5.4.2 SQUID Readout - Flux-Locked Loop - Magnicon *35*
5.4.3 AC vs DC biasing modes *35*
5.4.4 Determining the gradient sensitivity of the flip-chip gradiometer *38*

6 MAGNETIC TENSOR GRADIOMETER **42**

6.1 SYSTEM OVERVIEW 42
6.2 BRIEF DESCRIPTION OF OPERATION 43
6.3 ANCILLARY REFERENCE SENSORS – 3 MM SQUID MAGNETOMETERS 46
6.4 WIRING 47
6.5 RF SHIELDING 48
6.6 ACQUIRING DATA – DUAL CHANNEL 24-BIT ADC 49
6.7 THEORETICAL ASPECTS OF CALIBRATION, REFERENCING AND FIELD COMPENSATION 51
6.8 CALIBRATION AND REFERENCING CORRECTIONS OF SENSOR OUTPUTS 54
6.8.1 Field calibration and imbalance corrections *54*
6.8.2 Gradient calibration and offset corrections *57*
6.8.3 Effect of gradiometer offsets on gradient tensor determination *57*
6.8.4 Effect of finite size of gradiometer array *58*
6.9 LAB CALIBRATION - STATIC TESTING OF THE HTSTG IN LABORATORY CONDITIONS 61
6.10 DYNAMIC TESTING OF THE HTSTG IN LABORATORY CONDITIONS 65
6.11 BALANCE – COMMON MODE REJECTION 67

7 WEST HEAD FIELD TRIAL **69**

7.1 MEASUREMENT DETAILS 72
7.2 MAGNETIC DIPOLE PASSES WITH THE SYSTEM STATIONARY 74
7.3 SMALL ANGLE TILTING IN THE GEOMAGNETIC FIELD 75
7.4 MAGNETIC DIPOLE PASSES WITH THE SYSTEM UNDERGOING TILTING 79
7.5 ANALYSIS OF RESULTS 83

8 GLOBAL FEEDBACK SYSTEM **89**

9 WAVE INDUCED EFFECTS ON TENSOR MEASUREMENT **91**

9.1 SUMMARY OF WORK 91
9.1.1 Electric and magnetic fields in and around an insulating spherical capsule *91*
9.1.2 Effect of an ellipsoidal cavity *96*
9.1.3 Application to removal of noise due to ocean swells *99*
9.1.4 New methods for determination of dipole location and moment vector *99*

10 CONCLUSIONS AND FURTHER WORK **103**
REFERENCES **105**
PUBLICATION LIST **107**

Figures

Figure 1. Noise plot of all six gradiometers, used in the Magnetic Tensor Gradiometer (see example on the right), measured while magnetically shielded in the laboratory. The plots show that all six sensors have a noise performance either better than or close to the specified 2 pT /m / √Hz at 10 Hz. The magnetic shielding did not completely eliminate all background magnetic interference as is seen by the signals at ~ 15 Hz, 50 Hz (and higher order harmonics). 5

Figure 2. Electrical representation of the flip-chip gradiometer. 5

Figure 3. Six planar gradiometers were arranged in a pyramidal structure to enable determination of the full magnetic tensor gradient. 6

Figure 4. The full tensor system is comprised of six gradiometers and nine magnetometers. Signals are sampled using a 16 channel, 24-bit, ADC and recorded using a control PC. 7

Figure 5. Noise performances of four of six gradiometers operating unshielded at West Head(B) were found to be comparable with that of the shielded noise performance in the laboratory (A).Wind induced noise is believed to have influenced the unshielded noise performance of G2 and G5. 7

Figure 6. The full tensor system is shown sitting on a “tilt” table (A). The orange coloured electrical conduit was laid to form a fixed path for a magnet to travel along is shown on the left hand side of (B). 8

Figure 7. Static case: magnet of moment ~ 6 Am^2 moving passed the sensor system. Tensor components calculated from individual planar gradiometer responses (A). Comparison of calculated scaled moment vs forward modelled calculation of scaled moment (B). 8

Figure 8. While the system was in motion, the non-ideal common mode rejection of the Earth’s background field by all planar gradiometers gave rise to unwanted signals (A). Correction for this unwanted signal was provided via the signals associated with the linked movement of vector magnetometers (B). 9

Figure 9. Comparison of uncompensated gradiometer signal (blue), calculated common mode signal (red) and corrected gradiometer signal (green) for three differing sets of correction coefficients: (A) based on laboratory measurements, (B) based on field measurements and (C) including a dB/dt term. 10

Figure 10. Moving platform case – calculated tensor components (A) and comparison of calculated scaled moment and the forward modelled calculation of scaled moment (B). 10

Figure 11. Moving platform case – calculated path of moving magnet. 11

Figure 12. Non-tilting platform – calculated path of moving magnet, without referencing corrections (A) and with inappropriate referencing corrections for magnet fields, derived from tilt tests (B). 11

Figure 13. Schematic representations of two types of 1st-order gradiometer: (a) an axial gradiometer inductively coupled to the SQUID via a flux transformer and (b) a planar gradiometer with a directly coupled pickup loop (not shown to scale). 14

Figure 14. Electrical representation of the flip-chip gradiometer. 16

Figure 15. Custom built 2-channel noise measurement probe with a mounted device ready to test, with LEMO connectors 18

Figure 16. The shielded room at the CSIRO Lindfield site. 18

Figure 17. Close up of the I-V curve used to determine the critical current I_C of the SQUID device. 19

Figure 18. I-V curve used to determine the normal resistance R_N of the SQUID device. 19

Figure 19. V-Φ curve used to determine the peak to peak voltage modulation depth ΔV. 20

Figure 20. The Rubens coil set at the CSIRO Lindfield site. 20

Figure 21. The directed coupled readout SQUID gradiometer. The substrate step area is shown in pink. 22

Figure 22. The original dc SQUID loop design. 22

Figure 23. The read out gradiometer original and new pickup loop design. 23

Figure 24. The modified SQUID designs. Three in total incorporated into three separate gradiometers. 24

Figure 25. A close-up photo of the SQUID 2 loop under the microscope. 24

Figure 26. The unshielded gradient noise spectra of both devices described in Table 1, using dc biasing technique only. Gradiometer design B, despite having a slightly higher intrinsic flux noise, showed approximately 25% improvement in gradient field sensitivity due to its improved signal coupling. 27

Figure 27. The original and the new design for the gradiometric pickup loop antenna. 29

Figure 28. Flip-chip configuration of the readout gradiometer and gradiometric flux transformer. 29

Figure 29. The gradient field sensitivity of the flip-chip gradiometer, design A, with two different stand-offs d ~ 0.77 mm and d ~ 30 μm in comparison with the readout gradiometer alone. The inset photograph shows the flip-chip coupled device. 30

Figure 30. (a) Coupling efficiency between the input coil and the readout gradiometer as the stand-off d is varied. The response plateaus at approximately d ~ 150 μm (inset shows an illustration of the setup (b) the experimental setup using an input coil fabricated on a 10 x 10 mm substrate. 31

Figure 31. The gradient field sensitivity of the flip-chip gradiometer, design B, in comparison with the readout gradiometer. The inset shows a photograph of the flip-chip coupled device. 32

Figure 32. A comparison of the gradiometric antenna design C with design B. 33

Figure 33. Six design C gradiometric antennas before flip-chipping. 33

Figure 34. (a) Two readout gradiometers with Au on Mylar connections and (b) a finished flip-chip gradiometer showing a close up of the Au on Mylar between the readout and the antenna. 34

Figure 35. Shows a picture of the Magnicon FLL electronics setup. 35

Figure 36. Flux noise spectral density of gradiometer G3 measured inside three layers of mu-metal shielded using both the basic dc biasing and the ac biasing technique (note the broad peaks in the spectrum between 10-30 Hz are caused by a variable speed rotating magnet in the next room). 36

Figure 37. A readout device with its pickup loop removed. 38

Figure 38. A schematic showing the experimental setup for measuring the response of the readout gradiometer to a well defined magnetic source, at a standoff *r*. The source was made from two 2 m lengths of wire, separated by 15 mm, positioned in the plane of the gradiometer. 39

Figure 39. The readout gradiometers (with and without the flip-chip antenna) response to a defined magnetic source. The flip-chip device shows a ~28.7 times improvement over that of the readout gradiometer (JLOM14(I) #5) 39

Figure 40. The measured gradient noise of a readout gradiometer (#5) before and after it has been flip-chip coupled shown both inside mu-metal shielding and completely unshielded. The gradient noise is extrapolated from the flux noise.(note curve “unshielded with antenna” is dc biased only). 40

Figure 41. Schematic diagram of the tensor gradiometer system. 42

Figure 42. (a) Sketch of the tensor gradiometer with planar gradiometer, G, on the slanting faces of the polygonal pyramid (from Eschner and Ludwig, 1995b). (b) Optimal geometry for a hexagonal pyramid. 43

Figure 43. (a) Picture of the Dewar, pyramid (dimensions shown) and gradiometer holders prior to mounting and assembly of the system. (note shown also is the mini Dewar which allows room temperature AMR sensors to be positioned at the centre of the pyramid designed for use with a feedback system). (b) a picture of an assembled flip-chip gradiometer showing the position of the heater coils. 44

Figure 44. Wiring for the full system, with a total 108 wires (54 twisted pairs). 45

Figure 45. The hexagonal pyramid with six gradiometers dismounted and mounted inside the Dewar. The wiring is connected to the outside via five 24-way LEMO connectors. 45

Figure 46 (a) shows the YBCO pattern on the 3 mm dc SQUID magnetometers used as reference sensors. (b) Shows the positioning of the field sensors on system using a wire diagram representation (which includes the gradiometer sensors also) and (c) shows the field noise spectra for a typical 3 mm magnetometer, unshielded and shielded in the lab and also in a remote test location (West Head). 46

Figure 47. (a) The wiring diagram for the dc SQUID gradiometers using Magnicon electronics and (b) the pin connection diagram for the 24-way 3-channel LEMO connector. 47

Figure 48. Plots showing the normalised response of the gradiometers to an applied 8 Hz uniform magnetic field for (a) the original aluminium shielding and (b) the new silver shielding. 48

Figure 49. (a) Picture of the in-house developed 24-bit ADC and (b) the 24-bit dual channel ADC. 49

Figure 50. A flow diagram of the in-house developed dual ADS1258 24-bit ADC. 50

Figure 51. Schematic plan view of the hexagonal pyramidal array of gradient and field sensors, defining the azimuthal angles of upward normals to the sloping faces of the pyramid, relative to the instrument X axis (X referencing magnetometer axis). 51

Figure 52. Cross-section of a sloping face of the hexagonal prism, defining co-ordinate axes for individual sensors. The magnetometer and gradiometer on face *k* measure $B_{x'_k}$ and $B_{x'_k z'_k}$ respectively. 52

Figure 53. (a) The 2.5 m outer diameter, tri-axial Ruben's coil set in the Lindfield CSIRO laboratory and (b) mu-metal shielding used to measure the intrinsic noise of the devices. 61

Figure 54. Gradient noise plot of all six gradiometers, used in the Magnetic Tensor Gradiometer, measured while magnetically shielded in the laboratory. The plots show that all six sensors have a noise performance either better than or close to the specified 2 pT/m / √Hz at 10 Hz. The magnetic shielding did not completely eliminate all background magnetic interference as is seen by the signals at ~ 15 Hz, 50 Hz (and higher order harmonics). 62

Figure 55. Gradient noise plot of all six gradiometers, used in the Magnetic Tensor Gradiometer, measured while unshielded in the noisy laboratory environment. 62

Figure 56. The measured gradient sensitivity of a flip-chip gradiometer (G5) shown both with and without the antenna, inside mu-metal shielding and unshielded (using ac biasing). 64

Figure 57. (a) Top view of the system showing the orientation of the sensors (green indicates operating sensors red non-operational) and with respect to the plane of tilting. (b) The tensor gradiometer system mounted on the tilt table at the centre of the Ruben's coil set showing the tilt as a roll on a westerly heading. 65

Figure 58. Top plot: the raw output from the gradiometers (note G2 not included) while tilted in the lab. Bottom plot: the tilt angle as a function of time. 66

Figure 59. (a) the gradiometer output (G4) (green) and the estimated common mode signal calculated from the balancing routine using the reference SQUID magnetometers (red) and (b) the gradiometer output (green) and the balanced gradiometer signal (red) the system tilting unshielded in the open lab. 66

Figure 60. (a) the gradiometer output (G4) (green) and the estimated common mode signal calculated from the balancing routine using the reference SQUID magnetometers (red) and (b) the gradiometer output (green) and the balanced gradiometer signal (red) the system tilting unshielded in the open lab with an applied uniform field at 2 Hz. 67

Figure 61. LHS: Rubens coil set used to apply the uniform field to the device and RHS shows a diagram of the fields applied to the device. 68

Figure 62. Gradient noise spectra of all six planar gradiometers taken after initial cool down at West Head field trial site. 69

Figure 63. (a) A Google map image showing the route take to the West Head trial site from the Lindfield labs with the inset showing the exact location of the system. (b) shows a number of photos from the trial. Top left: intial cooling of the system using LN_2 showing the system mounted on the tilt table and drive shaft to a dc motor mounted on a tripod. Right shows a close up of the system. 70

Figure 64. Schematic diagram of the magnetic puck run setpup used in the West Head trial to simulate a magnetic anomaly passing by the system. The close up top down view of the inside of the Dewar shows the relative positioning of all the sensors with respect to the track with magnetometer M9 orientated parallel. 71

Figure 65. Gradient noise spectra for G1 measured inside three layers of mu-shielding in the lab, unshielded in the lab and unshielded at the West Head test site. 72

Figure 66. (a) the raw gradient fields measured by the six gradiometers as the magnetic puck is passed by at a average speed of ~ 2.66 m/s, (b) the extracted five independent tensor components, (c) calculated scaled moment plotted with the theoretical moment and (d) the tracking of the magnet for puck run #12 using the tensor components. 74

Figure 67. While the system was in motion, the non-ideal common mode rejection of the Earth's background fields shown in (a) for all planar gradiometers. Correction for this unwanted signal was provided via the signals associated with the linked movement of vector magnetometers shown in (b) for the in-field calibration. 75

Figure 68. (a)-(f). Corresponds to gradiometer G1-G6 respectively, LHS: shows the gradiometer output (green) and the estimated common mode signal calculated from the "lab" balancing routine using the reference SQUID magnetometers (red). RHS: The gradiometer output (green) and the balanced gradiometer signal (red) 77

Figure 69. shows the raw gradient measured signal (blue) for each of the six gradiometers G1-6, the estimated common mode signal obtained using lab field calibration (red) and the balanced gradiometer output (green). 79

Figure 70. shows the raw gradient measured signal (blue) for each of the six gradiometers G1-6, the estimated common mode signal obtained using the field calibration *with* time derivatives (red) and the balanced gradiometer output (green) 80

Figure 71. shows the raw gradient measured signal (blue) for each of the six gradiometers G1-6, the estimated common mode signal obtained using the field calibration *without* time derivatives (red) and the balanced gradiometer output (green). 81

Figure 72. Shows the estimated common mode signal obtained from the lab (red), the field calibration with dB/dt term included (green) and without the dB/dt term included (red) for each of the six gradiometers G1-6. 82

Figure 73. Comparison of the measured signal from G6 with the output predicted from the referencing magnetometer outputs*, including* time derivative terms. 83

Figure 74. Residual signals from G6 after removal of the referencing correction including and excluding time derivatives. In this case incorporation of time derivative terms makes negligible difference. 83

Figure 75. Comparison of the measured signal from G5 with the output predicted from the referencing magnetometer outputs, with time derivative terms (left) and without them (right).....84

Figure 76. (a) Referencing correction for G5 (blue), decomposed into contributions of magnetometer readings (red) and time derivative terms (green). (b) Residual signals from G5 after removal of the referencing correction. In this case incorporation of time derivative terms makes a significant difference. 84

Figure 77. Referencing-corrected signals for all gradiometers, using the lab coefficients and field obtained coefficients with and without inclusion of time derivative terms. 85

Figure 78. (a) the extracted five independent tensor components from the balanced gradiometer outputs using time derivative field derived coefficients, (c) calculated scaled moment plotted with the theoretical moment and (d) the tracking of the magnet for puck run #30 using the tensor components. 86

Figure 79. Non-tilting platform – calculated path of moving magnet, without referencing corrections (a) and with inappropriate referencing corrections for magnet fields, derived from tilt tests (b). 87

Figure 80 Noise spectra for the AMR sensor in shielding and unshielded to provide first stage noise reduction with 3 axis device shown in top right hand corner. 89

Figure 81 (a) A pair of nested spherical coils wound on hemispherical formers (Everett & Osemeikhian, 1966) and (b) a tri-axial Hemholtz coil set 90

Figure 82. Electric field profile, parallel to the uniform applied field, passing through the centre of a spherical cavity. 94

Figure 83. Magnetic gradient tensor elements along a vertical profile through the centre of a spherical cavity within a horizontal current flow distribution of limited depth extent. 95

Figure 84 Comparison of the gradiometric antenna design (C) used in the tensor gradiometer system and a newly designed antenna with improved baseline and effective area. 104

Tables

Table 1 Summary of fabricated and tested flip-chip gradiometer designs A-C, and future design D. 4

Table 2 Summary of the overall readout gradiometer device performance using modelled parameters including the 3 new SQUID designs. 25

Table 3. Readout gradiometer design measurement results 26

Table 4. Gradiometric flip-chip antenna optimization. 28

Table 5. Summary of the six flip-chip devices (note H1 and H4 were not determined using this method) 41

Table 6. Effects of finite size of planar gradiometers and of gradiometer array (source moment 1 Am²) 59

Table 7. A summary of the results obtained for each gradiometer device (designated G1-G6). The table gives the gradient sensitivity achieved at two different stages of the project for shielded and unshielded environments. Note for the December 2010 measures the unshielded measurements were performed using non-optimum dc biasing only. 63

Table 8. The achieved increase in gradient sensitivity using the gradiometric antenna. 64

Table 9. Lists both the individual balance and the system calibration determined balance. 68

Table 10. List of the various runs taken at West Head. 73

Table 11. Results from applying the in-field derived coefficients to Run 30. 88

1 Executive Summary

There may be as many as one million acres of the marine environment that are potentially contaminated by UXO. These environments vary significantly with respect to water depth, sea floor morphology, and geologic regimes. Current deployment modes place sensors 1 to 2 m above the sea floor, restricting detection capabilities, equivalent to that of airborne platforms in terrestrial applications. In this project we developed a High Temperature Superconducting Tensor Gradiometer (HTSTG). The system has inherently higher sensitivity and immunity to external noise than conventional magnetic sensor systems, thus improving detection performance in the difficult marine environment. The system also has enhanced characterization abilities as the location and magnetic moment of a target can be determined definitively by gradient tensor measurements at a few locations along a profile. This characteristic provides a significant advantage in the marine environment, which is difficult to regularly sample due to the effects of wind, waves and currents on the tow-vessel or deployment platform.

As noted on page 23, the first milestone of this project was to demonstrate a sensitivity of 2 pT /m /√Hz at 10 Hz in laboratory conditions, when measured in a mu-metal shielding enclosure.

- Measured sensitivities of six-gradiometers ranged from 1.25 pT rms/ m / √Hz and 2.28 pT rms/ m / √Hz at 10 Hz with four of the six achieving sensitivities of < *2 pT /m /√Hz at 10 Hz.*

The second milestone was to demonstrate full tensor measurements, while the system was both stationary and in motion, in laboratory conditions.

- This milestone has proven more difficult to demonstrate unambiguously. The total system was operated unshielded in the Earth's field. Four of the six gradiometers met the target sensitivity while sitting motionless in the Earth's field. The two remaining gradiometers noise performance was believed to have been by influenced by wind induced noise – i.e. by motion effects.

- The issue of the sensitivity of the complete gradiometer in terms of the individual device sensitivities is somewhat complex (described in Section 6.8). However we can determine that as the gradient falls off as the fourth power of the distance, the uncertainty in the measurement of the gradient is proportional to the fifth power of the distance; i.e. falls off rather slowly [SERDP Report MM-1643]. If ALL the devices were 14% less sensitive than the specification, the detection range would only drop from 4 m to 3.87 m, i.e. by 3%. This degrading of performance is conservative, since most of the devices have better than the specified sensitivity.

- Magnetometers used to provide compensation for the motion effects in the gradiometer signals have been shown capable of removing 99.4% of the gradiometer's motion induced signals.

- Accurate calculation of the system's compensation coefficients is critical to ensure that calculated tensor components are free of motion induced signals.

- These compensation coefficients need to be determined in a low gradient field environment.

- A further improvement of system's common mode performance by a factor of up to 100 to 500 is required to ensure that the intrinsic sensitivity of the system can be realised from a moving platform.

- For limited platform movement, such as might be expected in an underwater capsule, use of global feedback field cancellation coil may provide a means to meet this improvement.

A continuation of the project to trial proposed better techniques to determine the compensation coefficients is recommended. A further continuation to examine the benefits of trialling a global feedback scheme using feedback coils with open coil structure is also recommended. This proposed continuation would enable an unambiguous demonstration of Milestone Two. The continuation would also lead to an underwater trial of the system where the extended detection range and characterization capabilities of the HTSTG system could be demonstrated.

2 EXTENDED Summary

Project Objectives are to develop an HTSTG for detection and discrimination of ordnance in the marine environment (in water depths up to 20 m).

Specific research objectives and challenges included:

- Fabricate a high temperature superconducting (HTS) gradiometer with a sensitivity of 2pT/m / √Hz at 10 Hz in field-cooled conditions, measuring over a bandwidth of 0.1 to 30 Hz;
- Design and fabricate a cryogenic housing for the HTSTG system that can be deployed in a tow-fish and submerged to depths of up to 20 m;
- Develop and validate algorithms for wave-induced magnetohydrodynamic noise (a potentially significant noise source in the shallow marine environment);
- Validate a new dipole-tracking algorithm used with the HTSTG that is both robust and computationally undemanding;
- Conduct an underwater trial with the system that demonstrates the feasibility of the system.

Key Milestones for the projects are:

1. Sensors demonstrate unshielded sensitivity of 2 pT / m / √Hz at 10 Hz in the laboratory.
2. Full tensor measurements, while the system was both stationary and in motion, in laboratory conditions.
3. Underwater towed system demonstrates stability control
4. Initial Underwater system ready for deployment
5. Trial data demonstrates proof of concept.

As achievement of the first two milestones constituted a go / no go decision point for this project, the remainder of this extended summary focuses on progress towards meeting these two goals.

Milestone 1: Sensors demonstrate sensitivity of 2 pT / m / √Hz at 10 Hz in the laboratory.

Achieving the target sensitivity was done by optimising a number of critical gradiometer design parameters. Figure 2 shows an electrical representation of the flip-chip gradiometer indicating the adjustable parameters. The methodology was to increase the geometrical area A_{PL} of the pickup loops as much as possible while simultaneously reducing their inductance L_{PLA} as much as practical. Table 1 shows the evolution of the flip-chip gradiometer from design A to the final design C used in the system field trial. The table also shows an alternative larger area design (D) which has not yet been fabricated. This untested design is expected to have an achievable white noise floor that is significantly less than the target specification of 2 pT / m / √Hz.

Table 1 Summary of fabricated and tested flip-chip gradiometer designs A-C, and future design D.

	Design A	Design B	Design C	Design D
Outer dimensions	**38 x 20 mm2**	**38 x20 mm2**	**46 x 20 mm2**	**48 x 48 mm2**
Baseline *l*	**18.49 mm**	**18.0 mm**	**22.5 mm**	**33.2 mm**
Pick-up Loop Inductance L_{PLA}	58.23 nH	41.30 nH	44.98 nH	-
Input Loop Inductance L_{IN}	6.66 nH	5.76 nH	5.76 nH	5.76 nH
Area A_{PL} (one pick-up loop)	380 mm^2	380 mm^2	460 mm^2	1152 mm^2
Effective Area A_{EFF} (one pick-up loop)	**0.24 mm^2**	**0.57 mm^2**	**0.64 mm^2**	**0.89 mm^2**
Electrical contact	Wire bonds	Wire bonds	Indium /Au on Mylar	Indium /Au on Mylar
Gradient Sensitivity $S^{1/2}_G$ at 10Hz (Best shielded)	**6.7 pTm^{-1}Hz$^{-1/2}$ (measured)**	**2.9 pTm^{-1}Hz$^{-1/2}$ (measured)**	**1.25 pTm^{-1}Hz$^{-1/2}$ (measured)**	**0.7 pTm^{-1}Hz$^{-1/2}$ (estimate)**

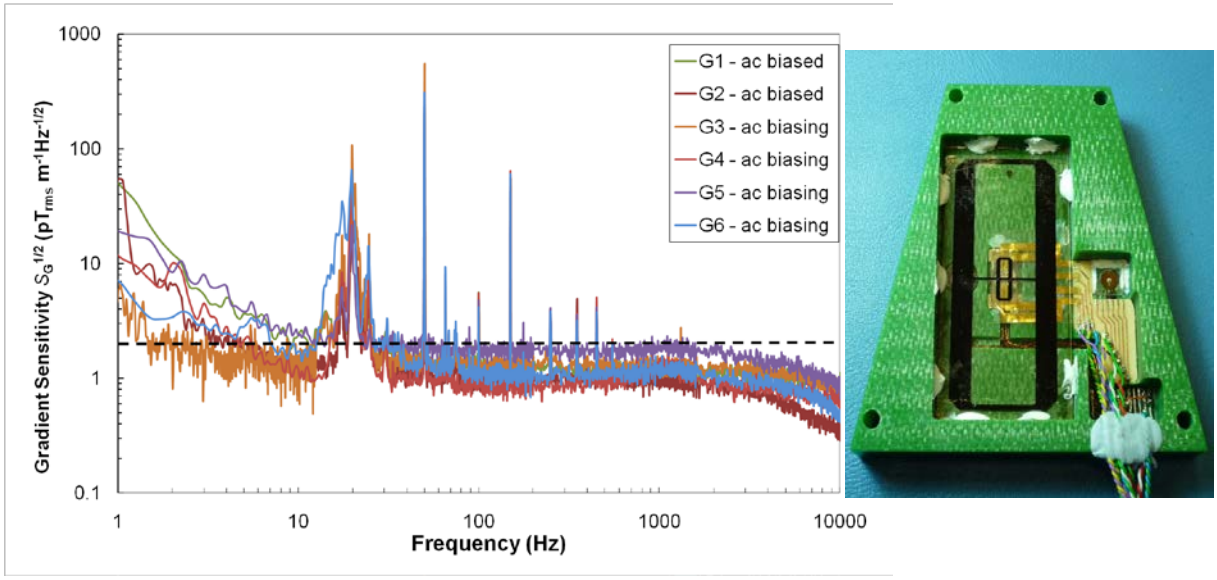

Figure 1. Noise plot of all six gradiometers, used in the Magnetic Tensor Gradiometer (see example on the right), measured while magnetically shielded in the laboratory. The plots show that all six sensors have a noise performance either better than or close to the specified 2 pT /m / √Hz at 10 Hz. The magnetic shielding did not completely eliminate all background magnetic interference as is seen by the signals at ~ 15 Hz, 50 Hz (and higher order harmonics).

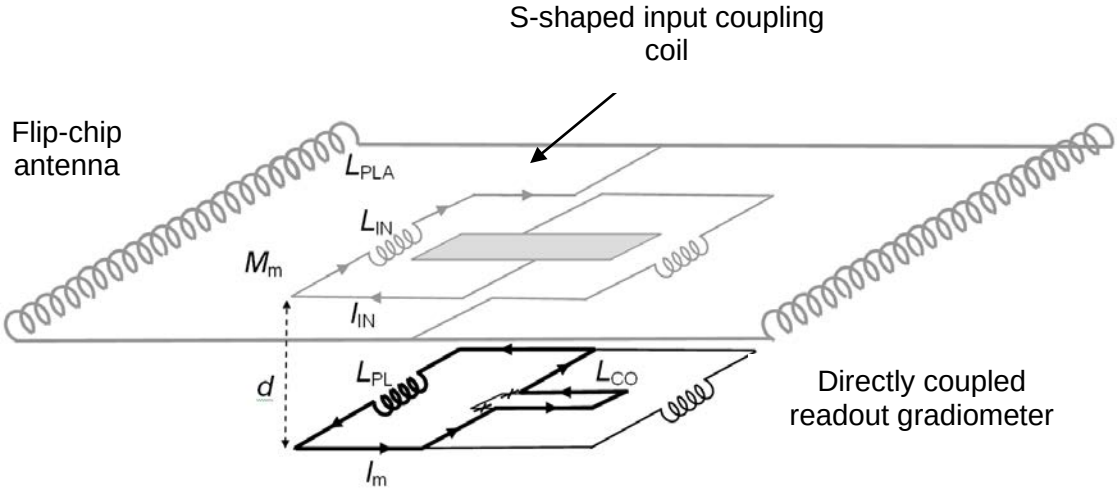

Figure 2. Electrical representation of the flip-chip gradiometer.

Six flip-chip gradiometers were fabricated using the design C antenna. This design formed the basis of the tensor gradiometer described in this report. When measured in a laboratory, while shielded inside a multilayer mu-metal magnetic shield, the measured sensitivity of the six gradiometers ranged between 1.25 pT rms/ m / √Hz and 2.28 pT rms/ m / √Hz. Measured unshielded, in a low noise environment sited well away from any cultural noise sources, the measured sensitivity ranged between 1.51 pT rms/ m / √Hz and 2.72 pT rms/ m / √Hz, see Figure 1. The gradient sensitivity milestone of < 2 pT / m / √Hz at 10 Hz was met by four of the six gradiometers, measured shielded in the lab.

Milestone 2: Full tensor measurements, while the system was both stationary and in motion, in laboratory conditions.

This milestone has proven more difficult to demonstrate successfully. In the full system, six planar gradiometers are arranged in a pyramidal structure to enable determination of the full magnetic tensor, see schematic Figure 3. These components form part of the full magnetic tensor gradiometer shown schematically in Figure 4.

The full system was used to track a moving magnetic target both while the system was stationary and while the system was moving in a cyclical motion, chosen to simulate the type of movement that might be experienced when the system is deployed in an underwater housing.

Due to the imperfect common mode performance of the individual gradiometers, it is necessary to compensate these sensors using auxiliary vector magnetometers. Two types of compensation sensors were included in the system, a type HMC 1053, 3-axes AMR sensor that provide magnetic vector information and multiple SQUID magnetometers that act as variometers, i.e. provide a measure of the change in vector field.

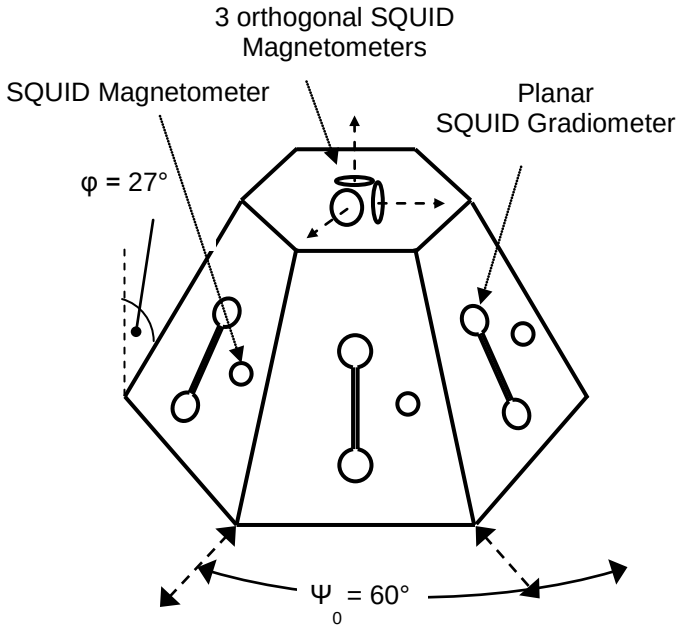

Figure 3. Six planar gradiometers were arranged in a pyramidal structure to enable determination of the full magnetic tensor gradient.

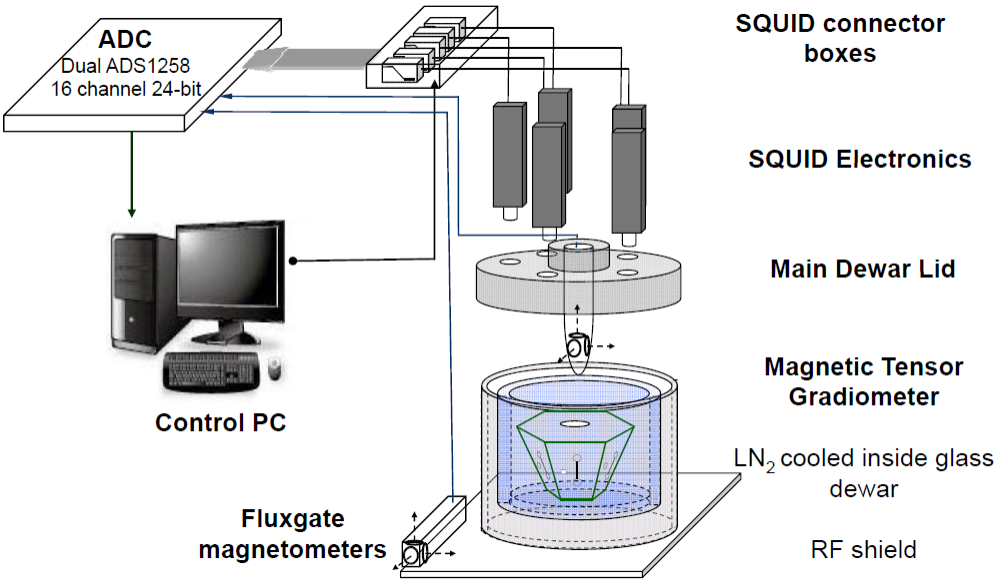

Figure 4. The full tensor system is comprised of six gradiometers and nine magnetometers. Signals are sampled using a 16 channel, 24-bit, ADC and recorded using a control PC.

Due to the existence of large background magnetic gradient fields that degraded the overall achievable noise performance, the CSIRO laboratory environment proved non-ideal for undertaking the "proof-of-concept" trials, see Figure 5. Thus the key set of "laboratory" experiments were undertaken at "West Head", a site located approximately one hour drive from the CSIRO's Lindfield laboratory in the Ku-ring-Gai Chase National Park. This site was chosen for its remote location from human habitation and deep underlying nonmagnetic sandstone deposits giving low magnetic background gradients.

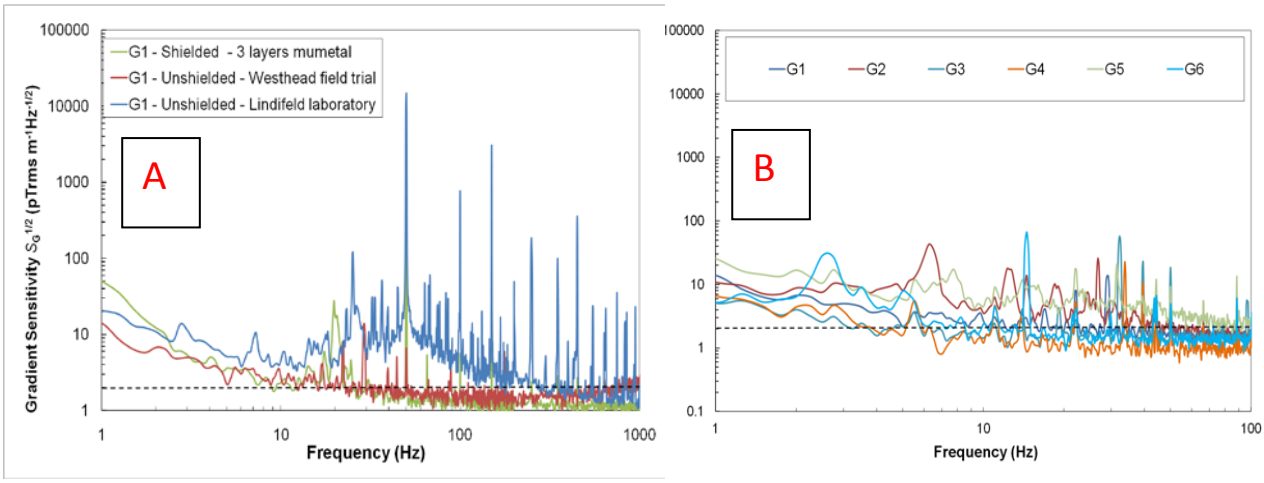

Figure 5. Noise performances of four of six gradiometers operating unshielded at West Head(B) were found to be comparable with that of the shielded noise performance in the laboratory (A).Wind induced noise is believed to have influenced the unshielded noise performance of G2 and G5.

Key experiments undertaken at West Head were the detection and location of a moving magnet whilst the system was both stationary and in motion. Figure 6 shows the system deployed at West Head. Electrical conduit was use to confine the magnet to a known path for

the series of experiments. The closest point of approach between the magnet and the sensor system was 2 m (6.56 feet).

Figure 6. The full tensor system is shown sitting on a "tilt" table (A). The orange coloured electrical conduit was laid to form a fixed path for a magnet to travel along is shown on the left hand side of (B).

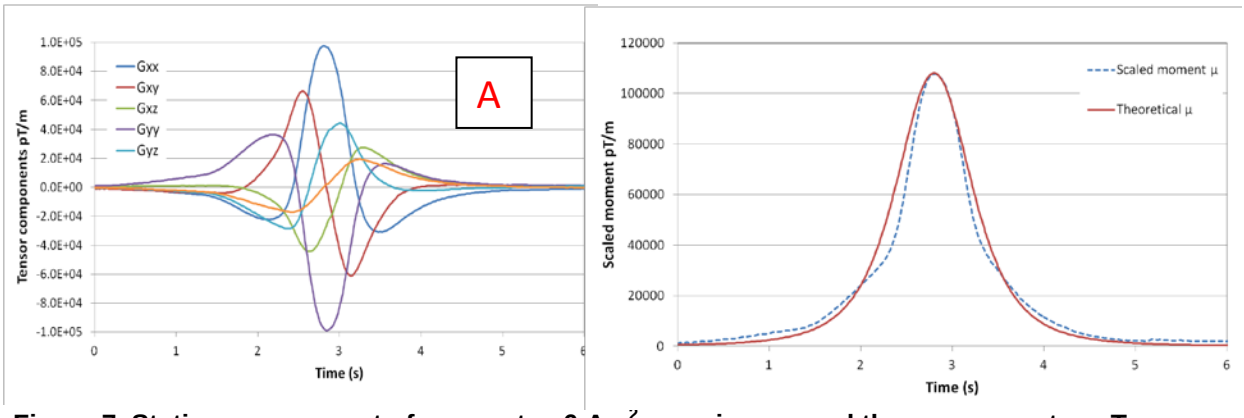

Figure 7. Static case: magnet of moment ~ 6 Am^2 moving passed the sensor system. Tensor components calculated from individual planar gradiometer responses (A). Comparison of calculated scaled moment vs forward modelled calculation of scaled moment (B).

From data collected using the control PC, individual measured gradient components were used to calculated the full tensor with the system both stationary and in motion. For the stationary case, with no compensation applied, the calculated scaled moment was a reasonable match to a forward modelled calculation of the scaled moment, see Figure 7.

Motion trials showed that the individual planar gradiometers had some residual sensitivity to the background field, see Figure 8. This residual sensitivity compromised the calculated tensor components. The level of residual sensitivity proved to be very dependent on the method used to determine the coefficients that correct for the unwanted gradiometer common mode sensitivity via the observed magnetometer signals. Correction terms were initially determined using known uniform and gradient fields generated inside the CSIRO laboratory. In hindsight it appears that the intercalibration of the gradiometers and the referencing coefficients (which correct the measured gradiometer outputs for common mode signals) was perturbed by induced magnetization of ferrous materials in the laboratory walls,

subfloor or ceiling spaces, which produced anomalous fields and gradients in phase with the slowly varying coil fields.

A differing set of coefficients was generated using the relationship between the unwanted, common mode, gradiometer signals and the response of the magnetometers while the system was tilted in the Earth's field at West Head. This second set of coefficients proved to be non-unique, as rotating the sensor approximately 45° on the moving platform produced another set of compensation coefficients. The reason for this is multicollinearity of gradiometer outputs and referencing magnetometer signals, which all vary in tandem as the system tilts. The best fit referencing coefficients for tilting within a single plane are therefore ambiguous – many alternative choices would work as well for that motion. A universally applicable set of referencing coefficients requires tilting in several different directions to resolve this ambiguity, or else application of accurately known, highly uniform fields and gradients in a magnetically clean environment.

Another refinement in developing the compensation coefficients proved to be including a term relating to the magnetic field components' time derivatives as additional terms in the correction algorithm. Figure 9 shows the high dependence on the correction of an individual gradiometer signal on the choice of compensation coefficients. An estimate of the effectiveness of compensation was derived by calculating the rms residual for an equally weighted combination of gradiometer outputs (as is used in calculation of the gradient tensor). For an uncorrected common mode signal of ~41 nT/m this residual was ~240 pT/m. This represents removal of 99.4% of the common mode response by the referencing. While apparently successful at the level of individual gradiometers, this compensation distorted results of the scaled moments derived from the calculated full tensors, see Figure 10. This result suggests the need for a more effective scheme for calibrating the system and calculating the compensation coefficients than was realised using the laboratory coil sets for generating the calibration signals; signals that were influenced by nearby magnetisable materials.

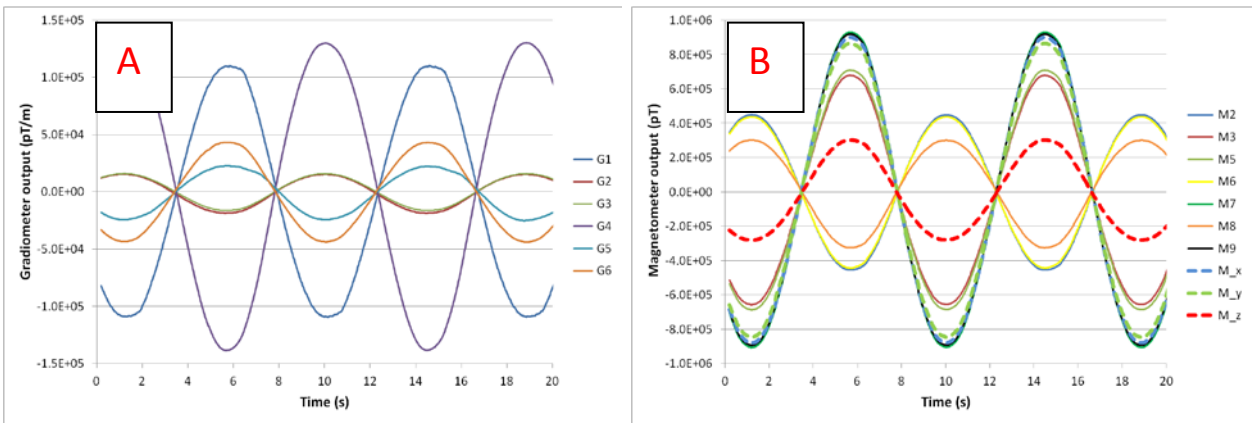

Figure 8. While the system was in motion, the non-ideal common mode rejection of the Earth's background field by all planar gradiometers gave rise to unwanted signals (A). Correction for this unwanted signal was provided via the signals associated with the linked movement of vector magnetometers (B).

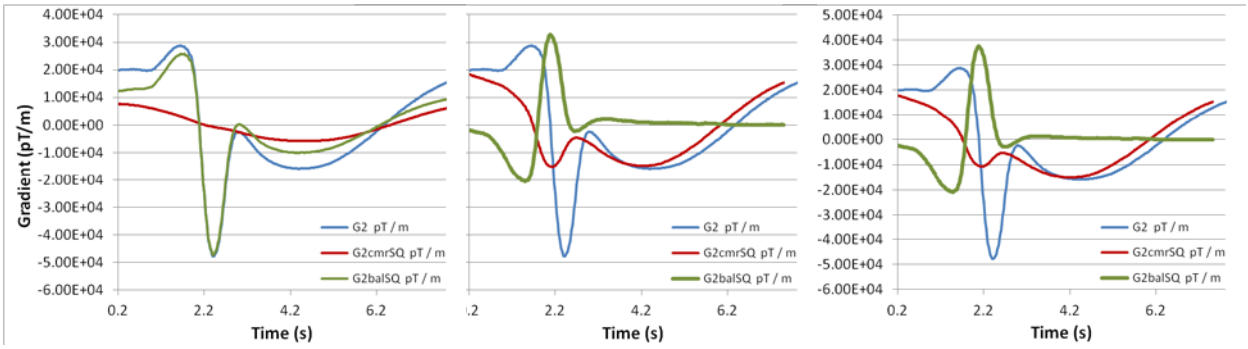

Figure 9. Comparison of uncompensated gradiometer signal (blue), calculated common mode signal (red) and corrected gradiometer signal (green) for three differing sets of correction coefficients: (A) based on laboratory measurements, (B) based on field measurements and (C) including a dB/dt term.

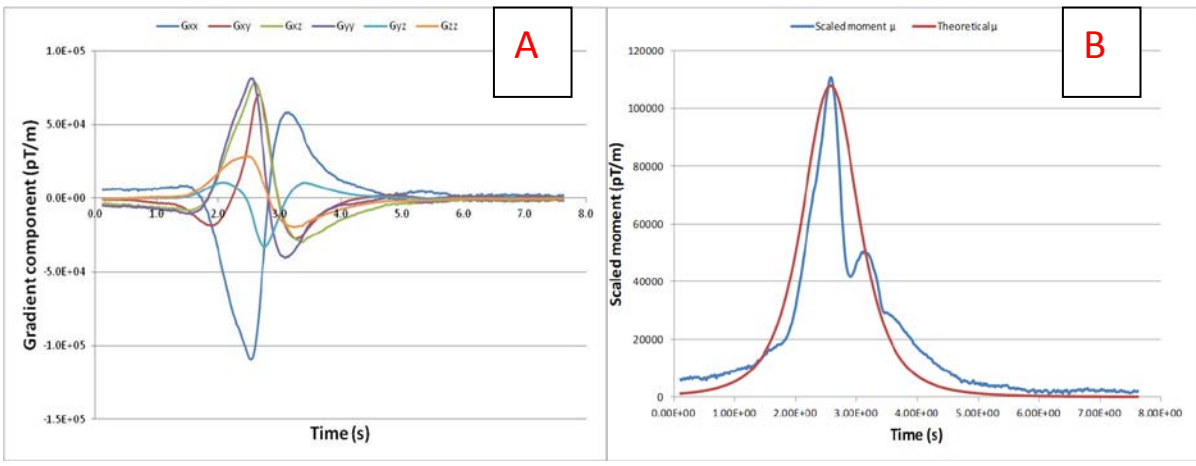

Figure 10. Moving platform case – calculated tensor components (A) and comparison of calculated scaled moment and the forward modelled calculation of scaled moment (B).

Comparison of the referencing-corrected gradient tensor elements with forward modelling of these elements for a magnet moving uniformly at its measured average speed showed quite good agreement in anomaly shapes, but with some systematic differences in relative anomaly amplitudes. These differences are attributed to inaccuracies in the intercalibration of the different gradiometers, due to the perturbations of the laboratory gradients. Assuming this to be the case, the anomaly amplitudes were renormalised to match the correct relative amplitudes and then used to invert for the magnet positions at successive measurement times. The results seem to support this assumption, because the inverted magnet positions track the inferred motion quite well, which would not be the case if the forms of the tensor element anomalies were badly distorted.

The major eigenvectors lie close to the plane containing the track and the sensor, which dips ~6° towards the track, and systematically rotate as the magnet moves past. The intermediate eigenvectors are consistently subvertical, approximately perpendicular to this plane, as they should be according to dipole tracking theory. Thus the inverted positions

always lie close to this plane when the dipole signature is clearly present. The results, projected onto this plane are plotted below, see Figure 11. The dots represent successive positions at 0.02 s intervals and the dashed line represents the actual path. For an approximately 5 m segment of the track around the closest point of approach, the magnet appears to move progressively along a path that meanders around the correct track. The smoothness of the path suggests that random noise is not significantly affecting the results, so the errors appear to be systematic. This is not surprising given (i) the roughness of the "calibration", and (ii) the imperfect removal of common mode effects arising from the dipole fields, for which the appropriate referencing coefficients had not been determined.

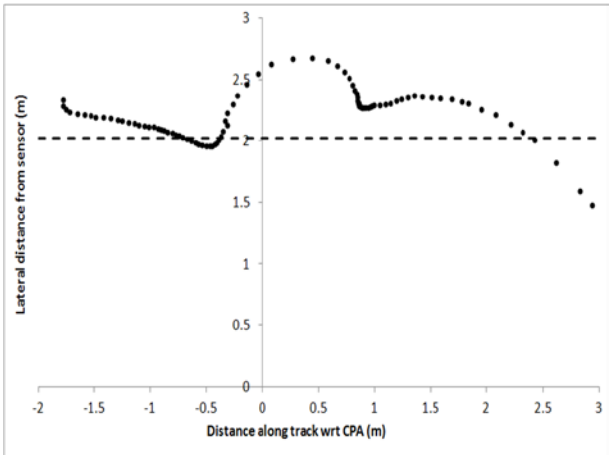

Figure 11. Moving platform case – calculated path of moving magnet.

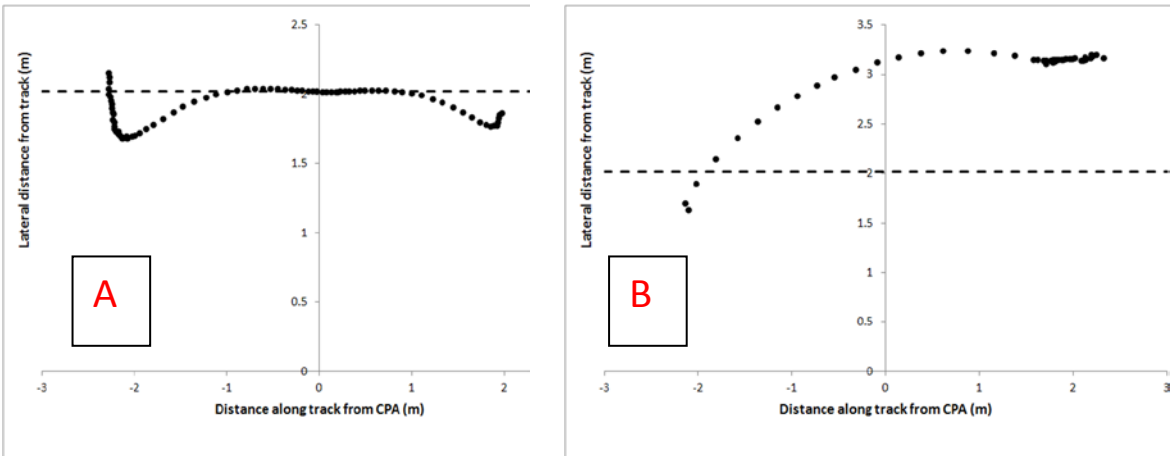

Figure 12. Non-tilting platform – calculated path of moving magnet, without referencing corrections (A) and with inappropriate referencing corrections for magnet fields, derived from tilt tests (B).

Figure 12(A) shows a similar analysis for a stationary sensor, without any referencing corrections being applied. The results are quite good, but apparent changes in speed (some of which may be real) and relatively small, but systematic, errors in position are evident.

These probably arise from the common mode effects of the magnet fields, which are uncompensated in these data. Figure 12(B) shows results for the same run, this time using inappropriate referencing coefficients derived from a tilt test. The systematic trend away from the correct track shows the importance of determining the correct referencing coefficients.

Meeting the required specification for the instrument requires further reduction of the common mode response by two orders of magnitude. This might be achieved by using a Rubens coil set, or another similar coil set, which when configured as part of a global feedback system, could be used to reduce to local field by two orders of magnitude. It can be shown that to meet the instrument specifications by correcting the measured gradients to an accuracy of ~1 pT/ m, the coil currents must be known to one part in ~10^4 (e.g. to 10 µA in 100 mA) if the field uniformity factor is 10^{-5}.

Next Steps

- Calibration in a low gradient field environment is essential to improve the performance of the HTSG system.

Possible alternatives to the initial laboratory calibration technique are under consideration. For example a spinning magnet, placed at differing several source-sensor separations, should provide sufficient data to uniquely separate the common mode and gradient signals and thus provide more accurate calibration and referencing coefficients for the compensation algorithm.

- Investigate the use of field cancellation techniques to reduce the sensitivity of the HTSG to movement in the Earth's field.

Measurements of the uncompensated common mode response in the gradiometer outputs due to small tilts, of about 1°, in the full geomagnetic field indicate that the required sensitivity specification can be met if the field seen by the devices is substantially reduced. If motions can be restricted to 5°, with associated uncompensated field variations less than ~5000 nT, averaging 5 samples at intervals of 0.02 s will give rms noise of ~2 pT/m, ten times a second, provided a field cancellation factor of ~500 can be achieved.

Field cancellation factors of this order can probably be achieved by relatively open feedback coil geometries, for example triaxial Helmholtz or Rubens coil configurations. The requirements for field uniformity across the instrument are not too stringent, provided the responses of the individual devices are calibrated in terms of measured feedback currents. The requirements for field cancellation can be relaxed somewhat if the common-mode-rejection-ratio of the devices is improved, which can probably be achieved by improvements in design or fabrication.

Detailed Report: SERDP MM1661

3 Introduction

There may be as many as one million acres of the marine environment that are potentially contaminated by UXO. These environments vary significantly with respect to water depth, sea floor morphology, and geologic regimes. Current deployment modes place sensors 1 to 2 m above the sea floor, restricting detection capabilities, equivalent to that of airborne platforms in terrestrial applications. In this report we describe the development of a High Temperature Superconducting Tensor Gradiometer (HTSTG). The system has inherently higher sensitivity and immunity to external noise than conventional magnetic sensor systems, thus improving detection performance in the difficult marine environment. The system also has enhanced characterization abilities as the location and magnetic moment of a target can be determined definitively by gradient tensor measurements at a few locations along a profile. This characteristic provides a significant advantage in the marine environment, which is difficult to regularly sample due to the effects of wind, waves and currents on the tow-vessel or deployment platform.

The first milestone of this project is to have the high temperature superconducting (HTS) gradiometers demonstrate a sensitivity of 2 pT /m /√Hz at 10 Hz in laboratory conditions. The second milestone is to achieve full tensor measurements, static and in motion, in laboratory conditions.

The target gradient sensitivity of 2 pT /m / √Hz at 10 Hz (unshielded) was chosen based on an analysis of detection range for different size munitions (Clark et al., 2009). High temperature SQUIDs were chosen as they are easier to deploy, using liquid nitrogen rather than liquid helium for cooling. The HTS materials are used to form intrinsic planar gradiometers. To increase sensitivity, the planar gradiometer is inductively coupled to a larger gradiometric flux transformer using a flip-chip configuration. Planar gradiometers only measure the off-diagonal components of the gradient tensor; however, the full magnetic gradient tensor can be calculated from planar gradiometers located on the faces of a pyramidal prism.

4 Background

High temperature superconducting quantum interference devices (SQUIDs) were chosen for the gradiometer as they would inherently provide higher sensitivity and immunity to external noise than conventional magnetic sensor systems. A survey of the literature shows that various sensor types have be used in magnetic tensor gradiometers developed for UXO detection: magnetoresistive (MR) (Czipott, 2002), fluxgate (Kumar et al., 2004), and superconducting quantum interference device (SQUID) sensors (Clem et al., 2001; Keene et al., 2005). SQUID sensors are the most sensitive of the three types. All of these prior systems use multiple sensors and calculate the gradients, either in software or electronically, which can be prone to error.

Keene et al. (2005) described a high temperature SQUID tensor gradiometer aimed at magnetic anomaly detection (MAD) from a moving platform. This system calculates the gradients by subtracting the output of two magnetometers. Sensitivities of 80 pT /m /√Hz at 1 Hz and 1 pT /m /√Hz in the white noise region were achieved while undergoing rotational motion (pitch, roll and yaw) of ±5º in the field (Humphrey et al., 2005).

SQUIDs can be configured as highly balanced intrinsic gradiometers which measure the gradient directly. Stolz et al. (2006) describes a full-tensor SQUID gradiometer system designed for airborne geophysical applications which uses low temperature SQUID gradiometers.. This system achieved a white noise level of 0.6 pT /m /√Hz with a corner frequency at 0.3 Hz, measured in a magnetically shielded room.

Eschner and Ludwig (1995a) showed that by using at least five planar gradiometers positioned on at least three non-parallel surfaces, one can calculate all components of the gradient tensor. Our design uses of an array of six planar SQUID gradiometers positioned on the slant faces of a hexagonal pyramid. This provides data redundancy leading to an over-determined system of linear equations for calculating the tensor components.

5 Planar Gradiometer

A first order intrinsic gradiometer detects the difference in flux measured by two spatially separated pickup loops (magnetometers) along a certain axis.

There are many ways to configure a gradiometer; the pickup loops can be inductively or directly coupled to the readout SQUID as shown in Figure 13. In the former, coupling to the SQUID is usually optimised using a multi turn input coil (a common technique used with LTS materials but difficult to achieve with HTS materials). The gradiometer can be axial and designed to measure on-axis gradients such as $\partial B_z/\partial z$ (as shown in Figure 13 (a)) or planar and designed to measure off-axis gradients such as $\partial B_x/\partial z$ (as shown in Figure 13 (b)).

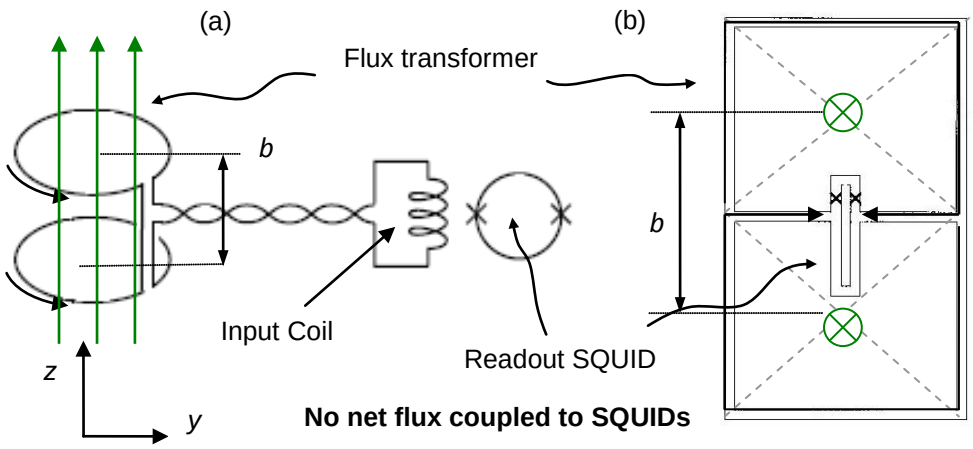

Figure 13. Schematic representations of two types of 1st-order gradiometer: (a) an axial gradiometer inductively coupled to the SQUID via a flux transformer and (b) a planar gradiometer with a directly coupled pickup loop (not shown to scale).

In both these cases a uniform magnetic field perpendicular to the pickup loops will couple an identical flux into each loop setting up identical screening currents which will cancel and thus couple zero net flux into the SQUID. Magnetic fields generated from distant sources of magnetic interference are approximately uniform at the gradiometer, and therefore are rejected. Magnetic signals generated in close proximity to the gradiometer will have a significant first order gradient, $\partial B/\partial z$, resulting in more magnetic flux being coupled to the

loop closer to the source and therefore a net signal being coupled to the SQUID. The SQUID output will be proportional to the field gradient.

For HTS devices, Single-layer directly-coupled devices have thus been favoured due to the simplicity of their fabrication and relatively high sensitivity. One drawback is the limited baseline achievable due to the size of available HTS substrates – the typical baseline for directly coupled is 0.3-1 cm. One way to get around this problem is to use a flip-chip arrangement

5.1 Flip-chip gradiometer using S-shaped coupling coil

The sensitivity of a SQUID gradiometer is given as:

$$S_G^{1/2} = \frac{S_\Phi^{1/2}}{lA_{EFF}}, \qquad (1)$$

where $S_\Phi^{1/2}$ is the spectral flux noise of the SQUID, l the gradiometer baseline and A_{EFF} the effective area of one pickup loop. To improve the overall gradient field resolution, we can first couple to a low noise SQUID and, second, increase the device responsivity ($l \times A_{EFF}$ product). For a planar configuration, one way to increase the responsivity is to inductively couple the SQUID to a much larger flux transformer in a flip-chip arrangement. Directly coupled devices of this size are rarely fabricated due to the cost of large substrates and the unreliability of the SQUID fabrication process. Because the readout SQUID devices can be placed on small substrates, a number of devices can be fabricated and tested, ensuring that sufficient good devices are obtained at a lower cost.

The gradiometer configuration we have used is based on an early flip-chip design by Faley et al. (1997) which uses a small directly coupled gradiometer as the readout sensor. The readout gradiometer is inductively coupled to a long baseline gradiometric transformer via an S-shaped input coil. Using this arrangement Faley attained a gradient sensitivity of 4 pT/ m/ $Hz^{1/2}$ at frequencies above 10 Hz and 10 pT/ m/ $Hz^{1/2}$ at 1 Hz. A similar flip-chip design has also been demonstrated previously by Tian et al. (1999), achieving a gradient sensitivity of 7.3 pT/ m/ $Hz^{1/2}$ in the white noise region and 59.6 pT/ m/ $Hz^{1/2}$ at 1 Hz using a multilayer flux transformer on a 2 inch wafer.

This flip-chip design has a number of advantages over conventional flip-chip arrangements which are generally inductively coupled to a small dc washer SQUID. For one, using a gradiometer readout sensor inherently makes the device more stable and less sensitive to background noise when operating in unshielded and mobile environments while doubling the effective input area due to having input to two gradiometer loops instead of a single loop when using a magnetometer. The device balance, $b = A_{PAR}/A_{EFF}$, where A_{PAR} is the device's parasitic effective area to uniform fields, is also improved due to the central 1 mm wide strip on the input coil which shields the SQUID (see design in Figure 14). Note that A_{PAR} is a combination of the response from the SQUID, A_{SQ}, and any uniform field response arising from defects or imperfections in the pick-up loop structure A_{DEF}

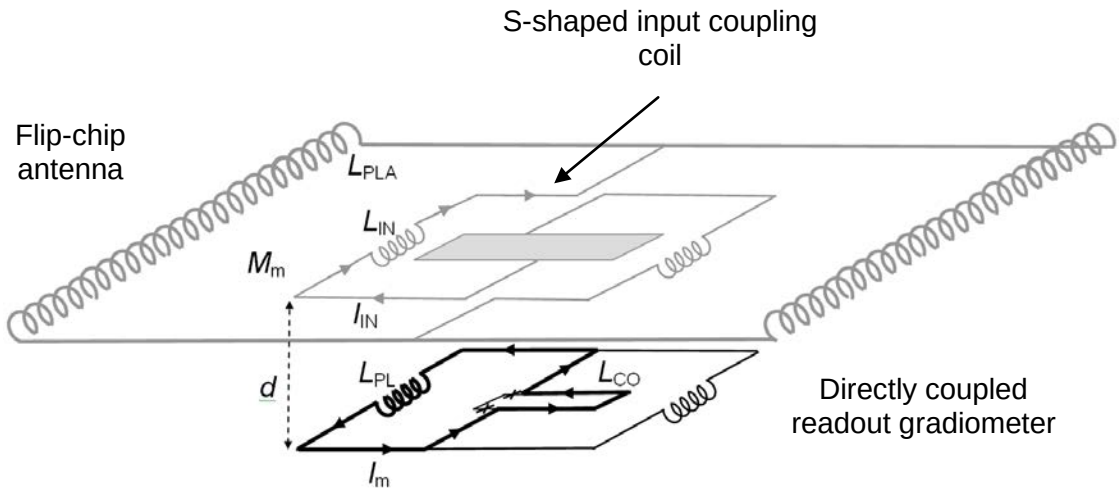

Figure 14. Electrical representation of the flip-chip gradiometer.

Figure 14 shows an electrical representation of the overall flip-chip gradiometer. It shows an input current I_{IN}, flowing through the input coil L_{IN} which is coupled by a mutual inductance, M_m, to the readout gradiometer's pickup loop, L_{PL}. The mutual inductance between the input coil and the readout gradiometer is given by

$$M_m = \alpha_1 \sqrt{L_{IN} L_{PL}}, \tag{2}$$

where α_1 is the coupling coefficient between the two and is ideally equal to 1. High values of α_1 are realised by minimising the separation d and through precise alignment of the superconducting coils. The current flowing in the input coil induces a current I_m in the gradiometer pickup loop, directly coupling a flux $\Phi = L_{CO} I_m$ into the SQUID inductance L_{CO}.

The mutual inductance between in the input coil inductance L_{IN} and the SQUID inductance L_{SQ} is negligible compared to the mutual inductance between the input coil and the pickup loop and thus can be neglected. Therefore

$$\left(L_{PL} + L_{CO}\right) I_m + M_m I_{IN} = 0 \tag{3}$$

and

$$\left| I_m \right| = \left(\frac{M_m}{L_{PL} + L_{CO}} \right) I_{IN}. \tag{4}$$

Since $L_{CO} << L_{PL}$ and $\Phi = L_{CO} I_m$

$$\Phi = \left(\frac{L_{CO} M_m}{L_{PL}} \right) I_{IN} \tag{5}$$

The current through the input coil I_{IN} is given by the applied flux $\Phi_{APP} = A_{PL}B_{APP}$ in the gradiometer antenna pickup loop divided by its inductance L_{PLA}.

The coupled SQUID inductance, $L_{CO,}$ is related to the SQUID inductance, $L_{SQ,}$ by:

$$L_{CO} = \alpha\, L_{SQ} \tag{6}$$

where the coupling coefficient, α, represents the fraction of the SQUID loop to which the pickup loop signal is coupled. Note also that the mismatch between the coupled SQUID inductance, L_{CO}, and the pickup loop inductance, L_{PL} determines the effective area of the pickup loop, given as

$$A_{EFF} = \left(\frac{\alpha L_{SQ}}{L_{PL}}\right) A_{PL} \tag{7}$$

where A_{PL} is the sensing area of the pickup loop (the geometrical area plus the effect of flux focusing). A full analysis of this flip-chip device design is given by Tian et al (1999).

5.2 Device Fabrication and Characterisation

The SQUID read out gradiometers are patterned using CSIRO's standard UV photolithography and Ar ion beam milling/etching (Foley et al., 1999) in our in-house clean room facility. The SQUID junctions use high performance patented step edge junction technology to generate the Josephson junctions in the dc SQUID. The high quality YBCO thin films (average film thickness ~220 nm, J_c ~ 3 MA/cm^2) were deposited by co-evaporation (Theva Gmbh, Germany) on polished MgO substrates.

For testing, each device was mounted on a testing PCB which contains a sapphire heater chip, mounting is initially done using double sided sticky tape subsequently (after initial testing) using silicon gel. Electrical connection is made from the Au contact pads to a PCB board using ultrasonically bonded Al wire (48 µm thick). The device is loosely encapsulated using a milled PCB cap incorporating a 9 turn modulation coil. The probe used to electrically test the devices is shown in Figure 15. This custom built two channel probe enabled the testing of both the gradiometer and in-plane magnetometer simultaneously.

Each SQUID device is tested to determine its electrical characteristics, namely its current-voltage (I-V) and Voltage (modulation)-Flux (V-Φ) curves, from which we can estimate the dc SQUID's I_c, R_N and ΔV values. Examples of typical curves are shown in Figure 17, Figure 18 and Figure 19. These parameters give a good indication of how the device will perform in terms of flux noise (sensitivity) and stability (when unshielded). Testing of the intrinsic parameters is performed inside mu-metal shielding and the rf shielded room (shown in Figure 15) to provide shielding from the Earth's magnetic field and other sources of broadband interference which can directly affect the intrinsic performance.

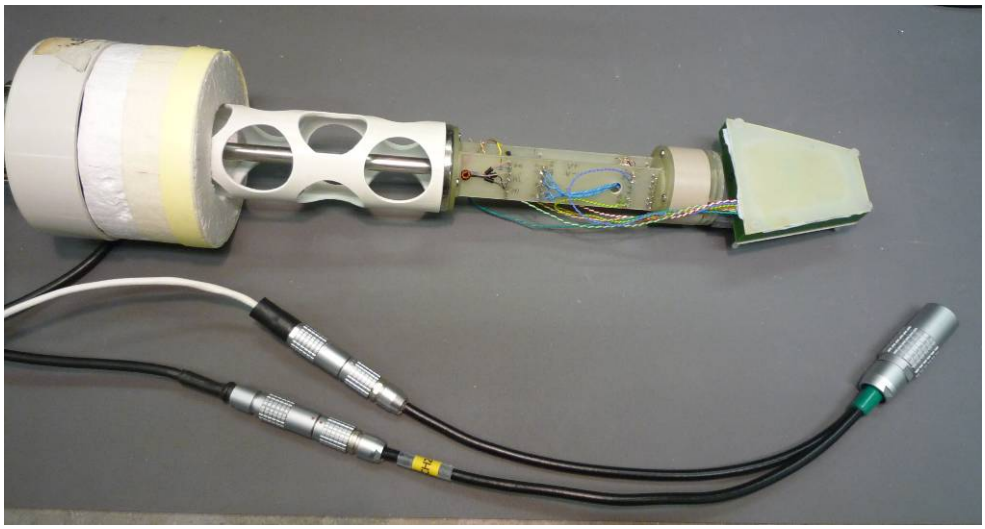

Figure 15. Custom built 2-channel noise measurement probe with a mounted device ready to test, with LEMO connectors .

Figure 16. The shielded room at the CSIRO Lindfield site.

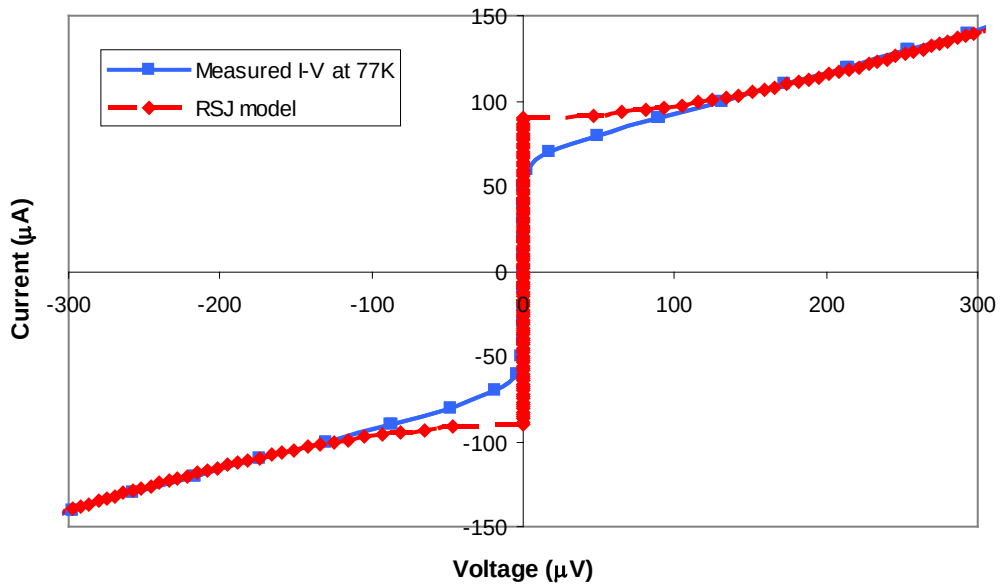

Figure 17. Close up of the I-V curve used to determine the critical current I_C of the SQUID device.

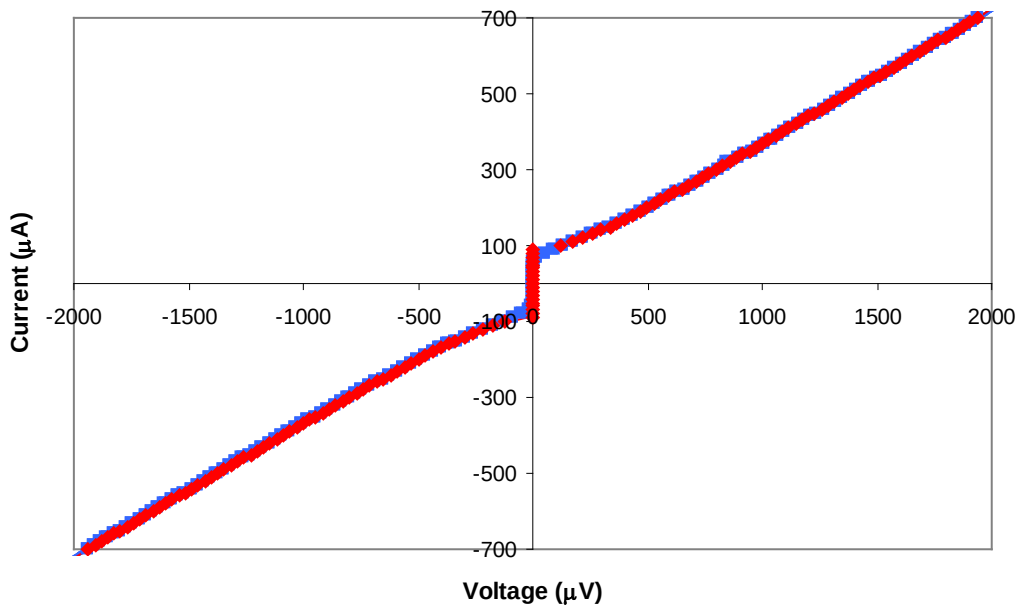

Figure 18. I-V curve used to determine the normal resistance R_N of the SQUID device.

Subsequent measurement of the SQUID's intrinsic flux noise was performed inside 6-layers of mu-metal, where the SQUID noise can be considered to be independent of the gradiometer pickup loops. This is because, ideally, there are no magnetic gradients inside the mu-metal shielding.

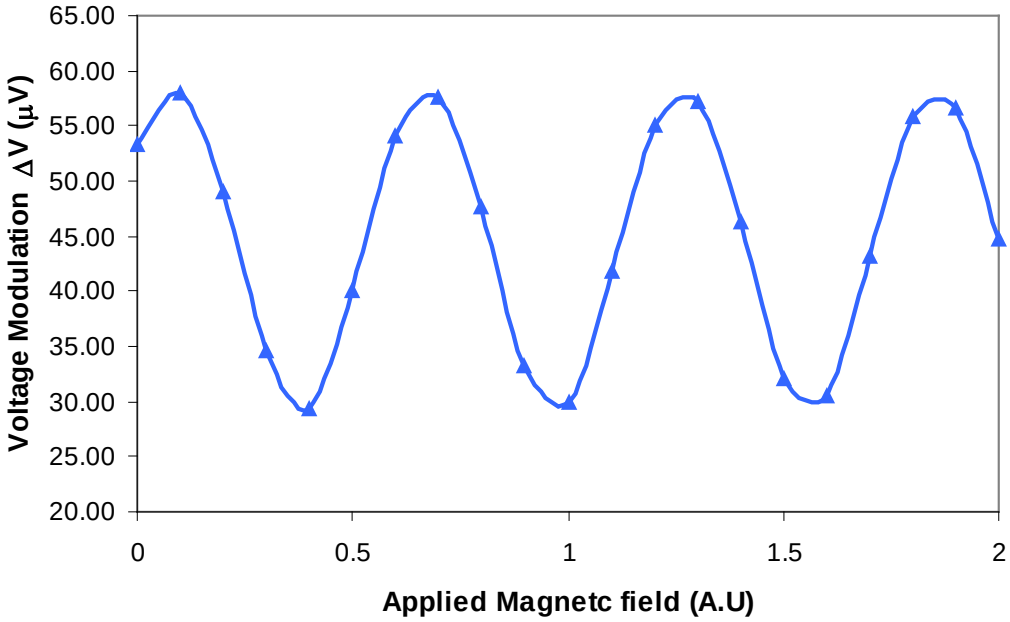

Figure 19. V-Φ curve used to determine the peak to peak voltage modulation depth ΔV.

Figure 20. The Rubens coil set at the CSIRO Lindfield site.

Further testing of gradiometer's unshielded performance including measurements of the parasitic and effective areas was carried out inside our Rubens coil set (Figure 20). The coils provide an area of highly uniform field (better than 1:1000 over a ±5 cm central volume) allowing accurate a.c. field responses to be measured (discussed further in section 6.9)

5.3 Gradiometer design and specifications

We investigated the performance of three separate gradiometric transformer and readout device designs, which we have called Designs A, B and C. The following sections describe details of the readout gradiometer and the flip-chip gradiometer designs.

5.3.1 THE READOUT GRADIOMETER

The single–layer, directly coupled, readout gradiometers are based on a design which was originally developed at CSIRO a number of years ago. The readout gradiometers have an area of 3 mm × 8 mm allowing two devices to be fabricated per 10 mm × 10 mm MgO substrate and diced after fabrication.

As shown in equation (1), the overall gradient sensitivity is directly proportional to the SQUID flux noise, $S_{\Phi}^{1/2}$. Therefore to ensure the optimum gradient sensitivity we must first minimize the flux noise. The spectral density of the flux noise is approximately given by:

$$S_{\Phi}^{1/2} \approx \frac{(16k_{\mathrm{B}}TR_{\mathrm{N}})^{1/2}}{V_{\Phi}} \qquad (8)$$

where the expression V_{Φ} ($\approx R_{\mathrm{N}}/L$) is the maximum slope of the transfer function at optimum bias current and $(16k_{\mathrm{B}}TR_{\mathrm{N}})^{1/2}$ represents the spectral density of the voltage noise. From this we can see that noise is reduced by decreasing the SQUID inductance and increasing the normal state resistance of the junctions. CSIRO's step-edge technology was used to form the SQUID's Josephson junction grain boundaries (Foley et al., 1999); this technique has proven to routinely produce SQUIDs with excellent junction parameters. A number of SQUID gradiometers have been fabricated (with varying SQUID inductances L_{SQ}) which show voltage modulation depths in the region of 10-30 μV with high $I_{\mathrm{C}}R_{\mathrm{N}}$ products ranging from 150-200 μV (having reasonably high normal state resistances R_{O} (=$2R_{\mathrm{N}}$) values from ~6-15 Ω).

For optimum flux noise performance, the inductance of the SQUID loop L_{SQ} must lie within a range such that the hysteresis parameter $\beta_L = I_{\mathrm{O}}L_{\mathrm{SQ}}/\Phi_0 \sim 1$, where I_{O} is the SQUID critical current, and Φ_0 is the flux quantum. Given that our SQUID critical currents I_{O} (=$I_{\mathrm{C}}/2$) generally range from ~10-40 μA, optimized noise performance (where β_{L} =1) will be for devices with the SQUID inductances of ~25-105 pH. Lower inductance generally leads to lower noise levels but at the cost of reducing the signal coupled to SQUID due to the increased inductance mismatch between it and the pickup loop, L_{PL}. In order to maximise the coupling of I_m to the SQUID, we modelled the inductance of the readout gradiometer using FASTHENRY[1], an inductance extraction software package. All inductance values shown in subsequent tables were extracted from models generated using FASTHENRY.

[1] FASTHENRY inductance software package, from Whitely Research Inc.

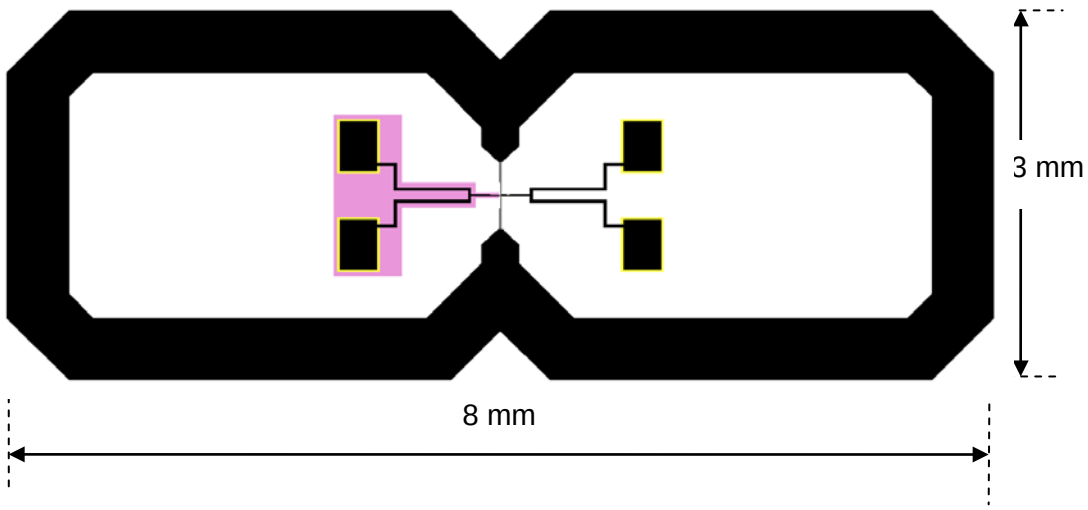

Figure 21. The directed coupled readout SQUID gradiometer. The substrate step area is shown in pink.

The original gradiometer design is shown in Figure 21. The gradiometer baseline is 3.7 mm with a pickup loop track width of 0.5 mm. The pickup loop inductance L_{PL} is ~ 6.66 nH and the effective sensing area of the pickup loop A_{EFF} is roughly ~14 mm^2. The pickup loop is directly coupled to a single narrow line-width dc SQUID (Figure 22) located in the centre of the device. The dc SQUID has an inner loop length of 65 µm, a loop line width of 4 µm, and 2 µm wide Josephson junctions. The SQUID inductance is L_{SQ} = 73.26 pH and the coupling inductance is L_{CO} = 45.69 pH, resulting in an inductance mismatch between L_{CO} and L_{PL} of ~1/145. This effectively reduces the pickup sensing area to A_{EFF} = 14 mm^2/145 = ~0.096 mm^2.

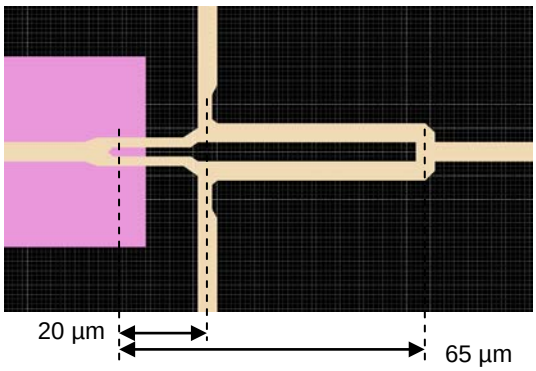

Figure 22. The original dc SQUID loop design.

The SQUID area A_{SQ} can be considered a parasitic area as it gives an unwanted response to uniform fields. Parasitic areas also include contributions due to imperfections and asymmetries in the pickup loops which add or subtract to the SQUID's effective area. Simply taking the SQUID's geometrical area A_{SQ} = 300 µm^2 (and neglecting any other parasitic areas), we estimate the gradiometer balance $b = A_{PAR} / A_{PL} \sim A_{SQ} / A_{PL}$ = 330 µm^2/0.096 mm^2 = ~1/290.

The original gradiometer design will obtain high gradient field sensitivity but we were able to improve its performance by reducing the inductance mismatch between the SQUID and the pickup loop, and by increasing the effective area of the readout sensor. Three adjustments were made to the original design:

- The track width of the pickup loop was increased from 0.5 mm to 0.7 mm on the sides but kept constant (0.5 mm) at both ends of the gradiometer so as not to affect the baseline (see Figure 23).
- The uncoupled track length was reduced to 10 µm for each SQUID.
- The SQUID loop length was increased to increase L_{CO}. Three different total loop lengths 67 µm, 82 µm and 100 µm (shown in Figure 24) were compared.

Four different SQUIDs were loop lengths varying from 67 µm to 100 µm were fabricated and tested. The results are summarised in Table 2.

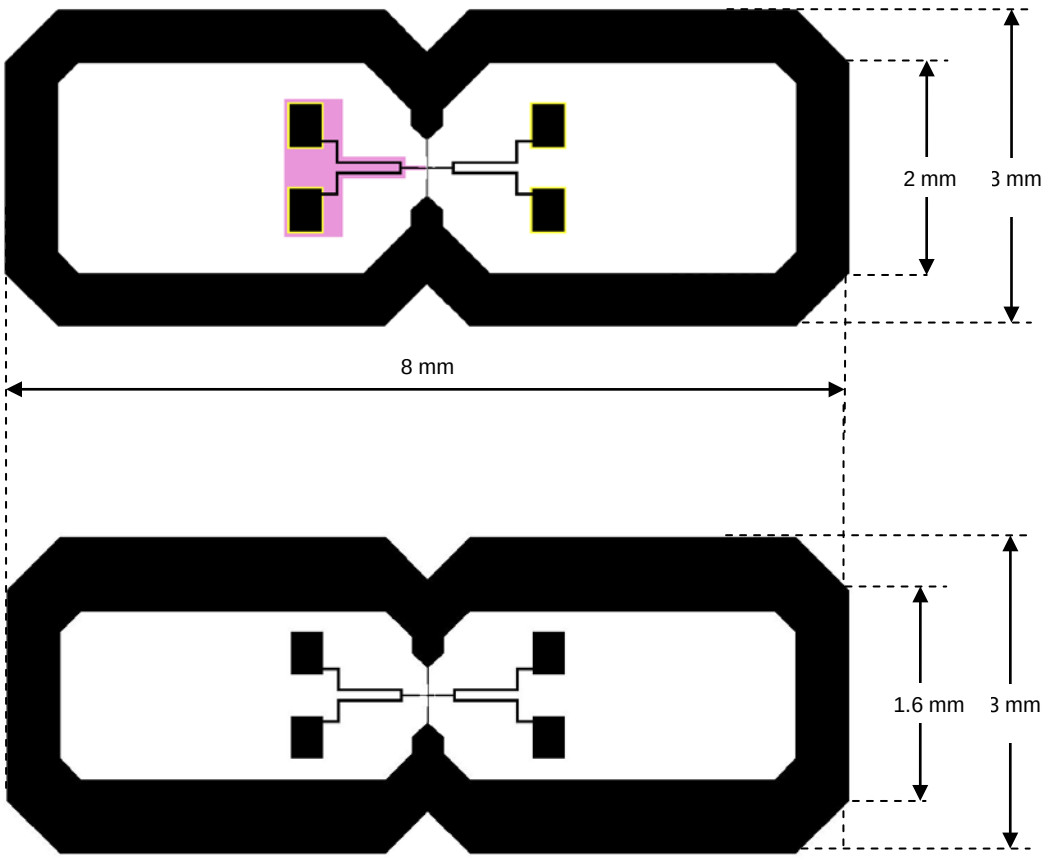

Figure 23. The read out gradiometer original and new pickup loop design.

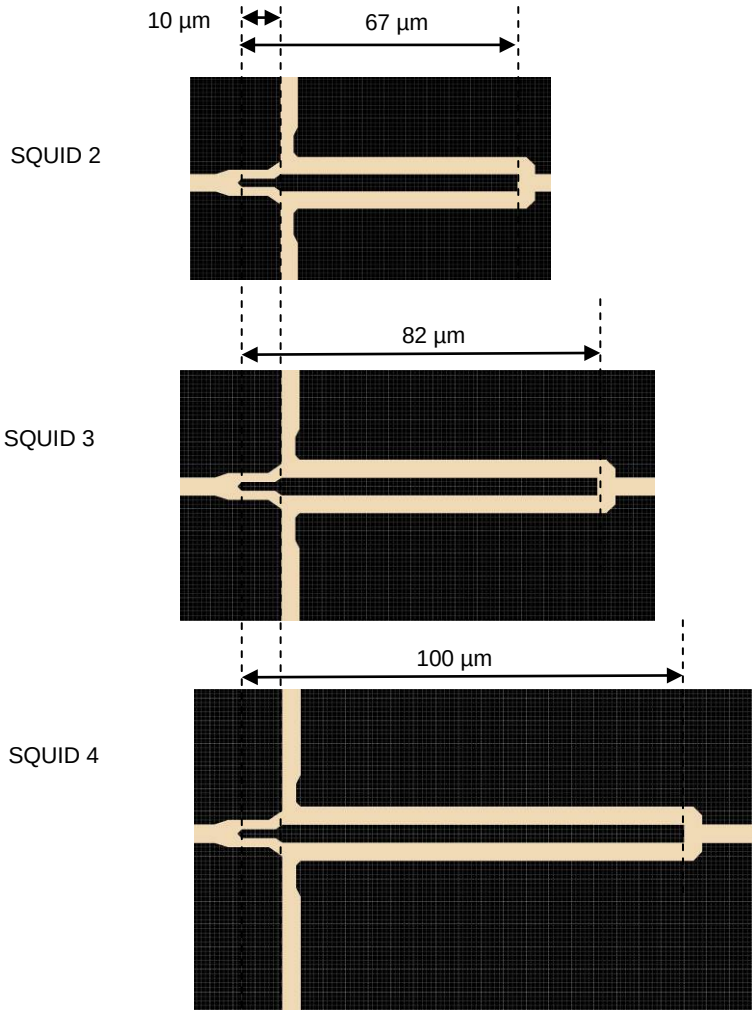

Figure 24. The modified SQUID designs. Three in total incorporated into three separate gradiometers.

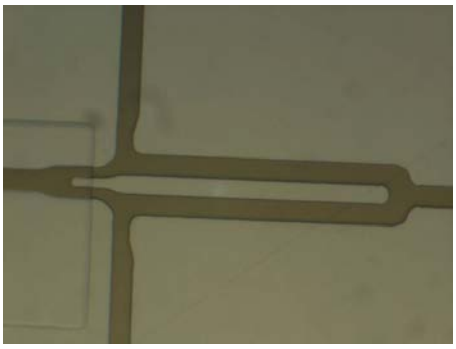

Figure 25. A close-up photo of the SQUID 2 loop under the microscope.

Table 2 Summary of the overall readout gradiometer device performance using modelled parameters including the 3 new SQUID designs.

Parameter	SQUID 1	SQUID 2	SQUID 3	SQUID 4
Baseline (cm)	0.37	0.37	0.37	0.37
SQUID loop length (μm)	65	67	82	100
Uncoupled SQUID loop length (μm)	20	10	10	10
SQUID inductance L_{SQ} (pH)	73.26	72.12	90.56	102.1
Coupled SQUID inductance L_{CO} (pH)	45.69	55.12	78.74	88.2
Pick-up loop inductance L_{PL} (nH)	6.66	5.76	5.76	5.76
Inductance mismatch	~1/145	~1/97	~1/73	~1/65
Effective area A_{MAG} of one pick-up loop (mm^2)	0.096	0.145	0.192	0.215
Theoretical SQUID flux noise ($\mu\Phi_0 Hz^{-1/2}$)	10	10	10	10
Projected Gradient Sensitivity* fT cm^{-1} $Hz^{-1/2}$ (white)	582	385	291	260

* based on theoretical SQUID noise

Further testing was carried out on the two designs which showed the lowest flux noise: the original design (SQUID 1 in Table 2 and the new design (SQUID 3 in Table 2). These designs were given the names Design A and Design B respectively. Table 3 details results of these two designs. Design B has a SQUID with loop length of 82 μm and is superior in overall performance to Design A. Design B shows a slightly poorer common mode rejection or balance of approximately 1/340 compared to 1/240 for Design A due to the larger area SQUID. Figure 26 shows the unshielded gradient noise spectra for both designs using dc biasing only (see Section 5.4.3 for further details). Although Design A had a lower flux noise 12 μΦ /√Hz than Design B's 19 μΦ /√Hz, Design B achieved a better gradient sensitivity of 64.8 pT/cm/√Hz at 1 kHz due to its improved signal coupling as shown in Table 3

Achieving a low flux noise is crucial for high sensitivity devices. The influence of SQUID inductance *L* (geometrical size) leads to a trade off where between flux noise and signal coupling. We have found that increasing the SQUID dimensions/inductance does marginally increase the sensitivity but at a cost to the noise. Reliably producing devices with low flux noise is difficult with increased inductance therefore we have chosen to design devices with design B pickup loops using SQUID 3 for all future work.

Table 3. Readout gradiometer design measurement results

	Design A	**Design B**
Gradiometer		
dc SQUID	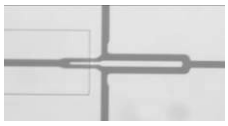	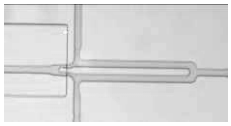
SQUID inductance L_{SQ}	73.26 pH (SQUID1)	90.56 pH (SQUID3)
Coupled SQUID inductance L_{CO}	45.69 pH	78.74 pH
Pick-up loop inductance L_{LP}	6.66 nH	5.76 nH
Inductance mismatch	~1/145	~1/73
Measured effective area A_{EFF}	0.083 mm^2	0.164 mm^2
Measured parasitic effective area A_{PAR}	340 μm^2	483 μm^2
Lowest measured SQUID flux noise $S_{\Phi}^{1/2}$	12 $\mu\Phi_0$Hz$^{-1/2}$	19 $\mu\Phi_0$Hz$^{-1/2}$
Gradient Sensitivity $S_G^{1/2}$ at 1 kHz	808 fT cm^{-1} Hz$^{-1/2}$	648 fT cm^{-1} Hz$^{-1/2}$

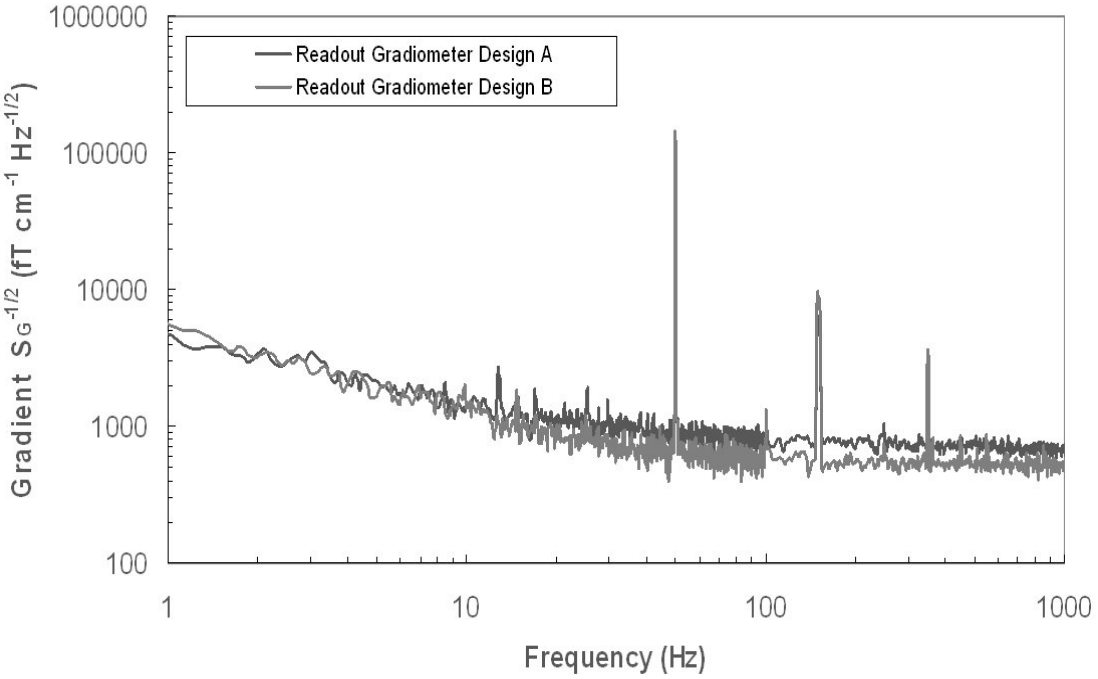

Figure 26. The unshielded gradient noise spectra of both devices described in Table 1, using dc biasing technique only. Gradiometer design B, despite having a slightly higher intrinsic flux noise, showed approximately 25% improvement in gradient field sensitivity due to its improved signal coupling.

5.3.2 FLIP-CHIP ANTENNA

The original (A) and the second design (B) for the gradiometric flip-chip antenna are shown in Figure 27. The gradiometer antenna structure extends an area of 40 mm × 20 mm which is directly coupled to an S-shaped coupling coil. In accordance with Peiselt et al. (2003), the input coil (at the centre of the gradiometer) is designed to be congruent with the readout SQUID gradiometer's pickup loop to maximize coupling. The internal 0.5 mm wide strip of the antenna provides good coupling to the pickup loop of the readout gradiometer and additionally shields the dc SQUID, reducing the parasitic response to uniform field and improving the balance. The gradiometric antenna has an intrinsic balance of ~10^3 due to about a 1 µm precision of the photolithography.

Again, as for the readout gradiometer, the outer dimensions of the antennas' pickup loops remain the same for both designs, whereas the inner dimensions were varied to increase the inductance matching. This is detailed in Table 4. The gradiometric pickup loop antenna side track width was increased from 1 mm to 4 mm and the end track width increased to 2 mm.

In order to achieve good coupling between the two superconducting YBCO layers, a flip-chip configuration is used which requires the readout gradiometer and antenna to be mounted with their superconducting layers face to face, as shown in Figure 28. In order to protect the surface of the devices, a 1.6 µm thick passivation layer of silicon dioxide (SiO_2) is deposited on the surface of the gradiometric antenna using a spin on glass (SOG) mixture. SiO_2 is chosen as it easy to deposit, electrically insulating, mechanically hard, has a similar thermal expansion coefficient as YBCO, and will not chemically react with the YBCO. This layer also helps to hermetically seal the device improving the stability over time.

The readout gradiometer and the gradiometric antenna are optically aligned under a microscope to a precision of better than ±0.2 mm and held in position using silicon rubber. An additional 22 μm layer of Mylar is placed in between the two to provide extra protection for the gradiometer surface.

Table 4. Gradiometric flip-chip antenna optimization.

	Design A	**Design B**
Baseline	18.49 mm	18 mm
Pick-up loop inductance L_A	58.23 nH	41.30 nH
Input loop Inductance L_{IN}	6.66 nH	5.76 nH
Area A_{PL} of one pick-up loop	380 mm^2	380 mm^2
Effective area A_{MAG} of one pick-up loop (coupled to gradiometer)	0.24 mm^2	0.57 mm^2

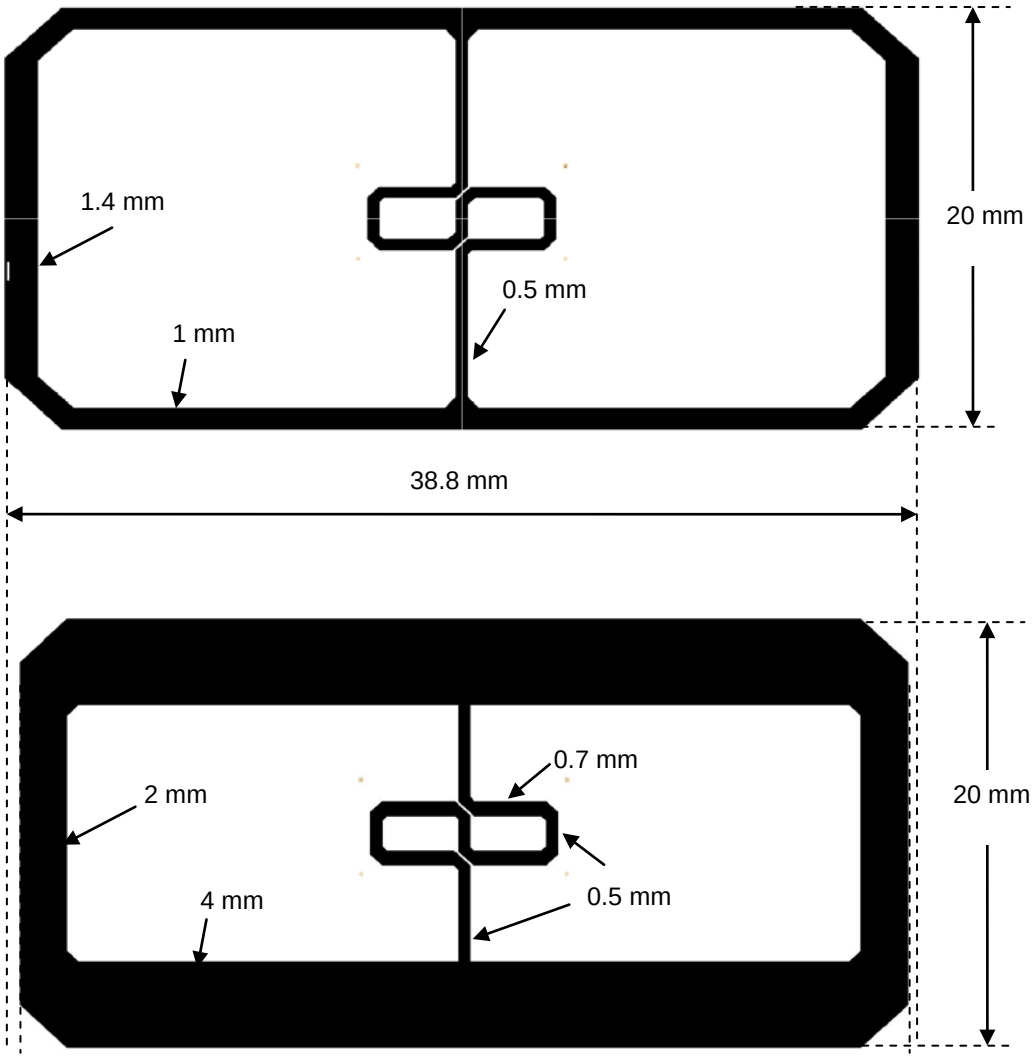

Figure 27. The original and the new design for the gradiometric pickup loop antenna.

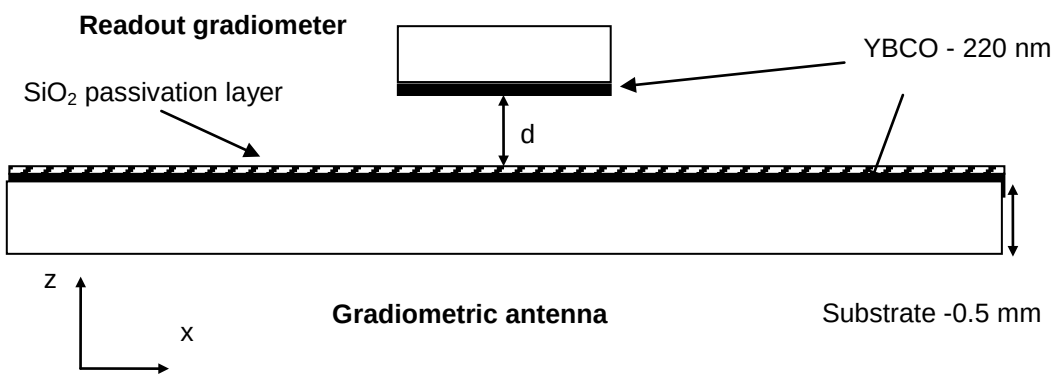

Figure 28. Flip-chip configuration of the readout gradiometer and gradiometric flux transformer.

The devices were calibrated by positioning the centre of the gradiometer a set distance above a pair of parallel current carrying wires 2.5 m in length. The response to this known gradient field was measured for the readout gradiometer and repeated using the flip-chip gradiometer. The increase in signal gain directly relates to the overall gain in gradient sensitivity.

-

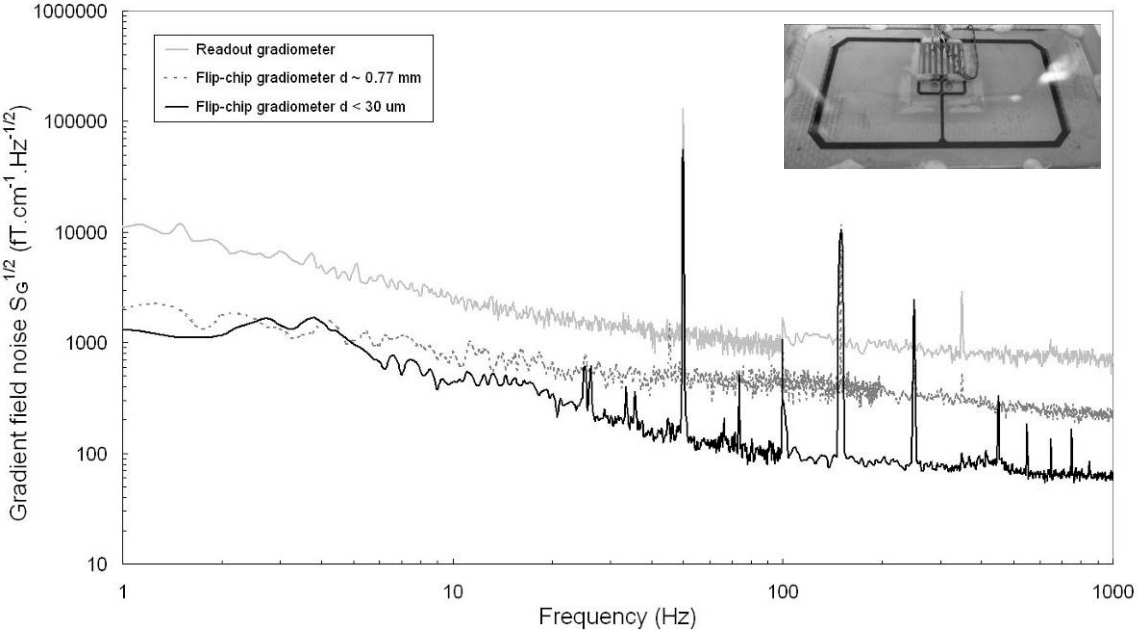

Figure 29. The gradient field sensitivity of the flip-chip gradiometer, design A, with two different stand-offs d ~ 0.77 mm and d ~ 30 µm in comparison with the readout gradiometer alone. The inset photograph shows the flip-chip coupled device.

The initial flip-chip test (shown in Figure 29) was made using device design A with a standoff *d* of ~0.77 mm. This test showed a factor of 5 increase in the gradient field sensitivity with the flip-chip gradiometer compared to that of the readout gradiometer. In the flip-chip arrangement, the readout gradiometer was operated as normal in the flux-locked loop (FLL) mode and modulated using a coil mounted underneath the housing. All subsequent noise spectra were measured in an unshielded magnetic environment and using dc biasing method only. The second test was performed with a spacing $d < 30\ \mu m$ as detailed above and yielded further increase in sensitivity to give a $S_G^{1/2}$ (flip-chip) $\approx S_G^{1/2}/12$. This gave a gradient sensitivity of 6.7 pT/cm/Hz$^{1/2}$ in the white noise region and 43.0 pT/cm/Hz$^{1/2}$ at 10 Hz.

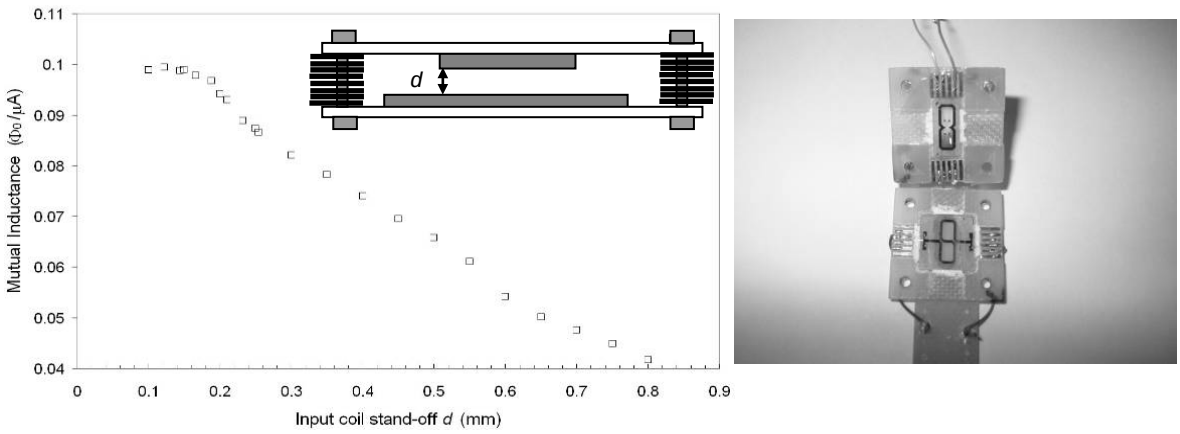

Figure 30. (a) Coupling efficiency between the input coil and the readout gradiometer as the stand-off d is varied. The response plateaus at approximately d ~ 150 µm (inset shows an illustration of the setup (b) the experimental setup using an input coil fabricated on a 10 x 10 mm substrate.

These initial tests prompted an investigation of the coupling efficiency between the input coil and the gradiometer. Using the setup in Figure 30(b), we devised a simple experiment to precisely vary the spacing *d* from 0.8 mm to a minimum standoff of 0.1 mm using several 50 μm thick layers of Mylar stacked together as illustrated in the inset of Figure 30(a). This was then repeated using 22 μm thick layers from a standoff of ~0.154 mm. A successive Mylar layer was removed prior to each cooling cycle. After cooling with liquid nitrogen, the SQUID was operated in a flux locked loop inside three layers of mu-metal shielding and the current required to couple $1\Phi_0$ into the SQUID loop was measured. The results are shown in Figure 30(a). The response plateaus at a separation of ~ 150 μm implying that the optimum coupling has been reached.

Gradiometer B was fabricated and tested in the same manner as A. This improved flip-chip gradiometer design showed an increased gradient sensitivity of ~19.5 over that of the readout gradiometer B as shown in Figure 31 with an overall lowest gradient sensitivity of ~29 fT cm^{-1} $Hz^{-1/2}$ in the white noise region and 170 fT cm^{-1} $Hz^{-1/2}$ at 10 Hz.

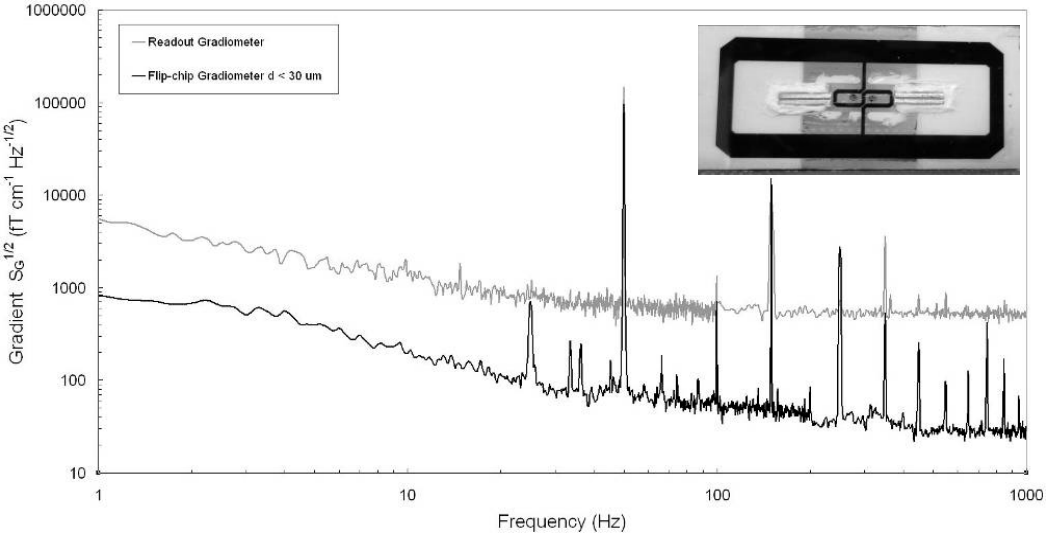

Figure 31. The gradient field sensitivity of the flip-chip gradiometer, design B, in comparison with the readout gradiometer. The inset shows a photograph of the flip-chip coupled device.

5.4 Design C

As it is difficult to guarantee a low flux noise value for every SQUID device we fabricate, we have further improved the coupling efficiency of the antenna to ensure high sensitivity when in flip-chip configuration. The gradiometric antenna for design C was improved in two ways: (1) an increase in the geometrical area A_P from 380 mm^2 to 460 mm^2 (an increase of ~20%); and (2) an increase in the baseline l from 18.5 mm to 22.5 mm (again a ~20% increase), compared to design B (note the availability of larger sapphire substrates (50 mm x 50 mm) on the market allowed for the increased dimensions). Figure 32 shows the comparative dimensions of both design B and C. This input coil dimensions remain unchanged. Given the gradient sensitivity $S_G^{1/2}$ varies as $S_\Phi^{1/2} / (A_{EFF} \times l)$, where $S_\Phi^{1/2}$ is the SQUID's flux noise, A_{EFF} is the effective sensing area and l is the baseline, we have the potential to improve the gradient sensitivity by as much as 40% with a constant flux noise.

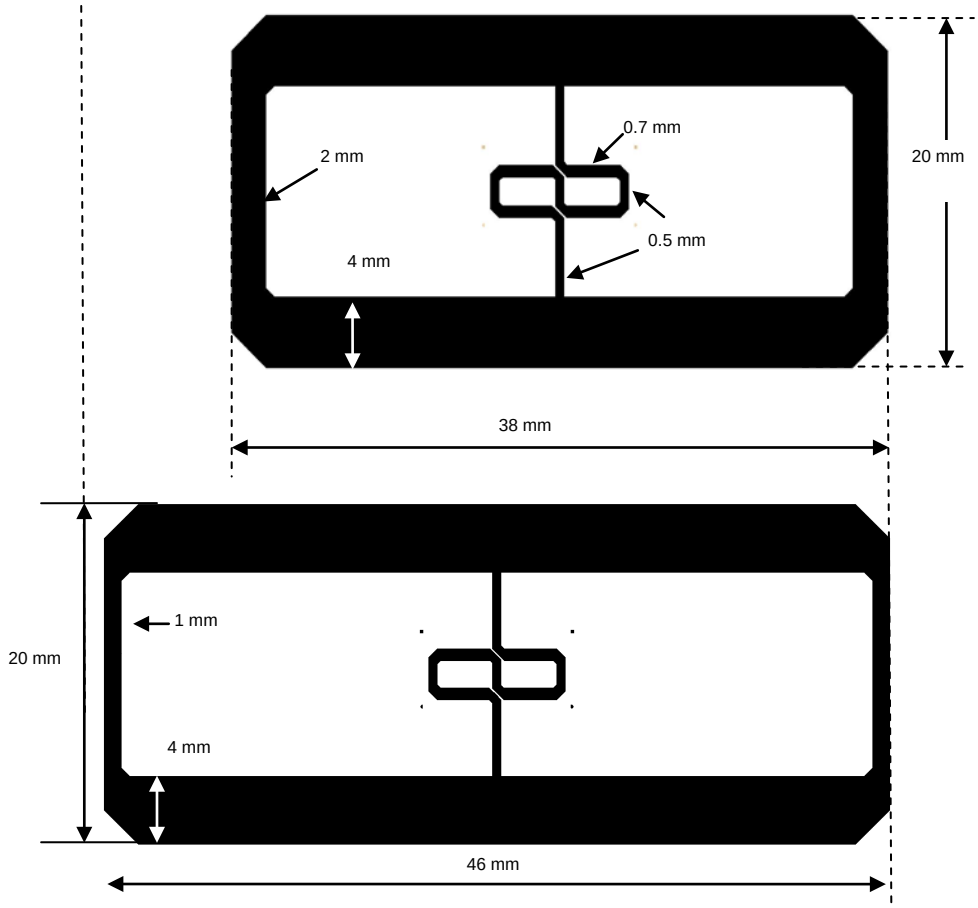

Figure 32. A comparison of the gradiometric antenna design C with design B.

Six of these devices were fabricated as before using UV photolithography and chemical wet etching. Instead of using a layer SiO_2 to passivate these devices a 3 μm layer of photoresist was used. The SiO_2 had shown some signs of deterioration on the other devices perhaps due to the age of the product used. Figure 33 shows the six gradiometric antenna prior to spinning-on of the passivation layer and mounting in the holders.

Figure 33. Six design C gradiometric antennas before flip-chipping.

5.4.1 ELECTRICAL CONNECTION

Electrical connection to the read-out gradiometer of the initial two flip-chip gradiometers (design A and B) was made by milling out two 1 mm holes in the antenna substrate above the Au contact pads and ultrasonically bonding fine Al wire (33 μm in diameter) to a copper strip on a nearby PCB. This method, although effective in the short term, after several thermal cycles may eventually damage the antenna substrate by deepening the slightly cracked area around the milled holes. Therefore, an alternate method was sought. From Figure 30 we can see that standoff distances of up to 150 μm have little effect on the coupling to the device. Given this information we investigated several methods to make connections to the readout device including insulating silver paint strip-lines with thin layers of Mylar, thinned silver wire and Au sputtered on Mylar. Au on Mylar proved to be the most reliable and reproducible. A 5-10 μm thick layer of Au was sputtered on 50 μm Mylar in our IBE vacuum chamber. Thicker layers of Au tended to be less flexible on the Mylar and would peel away. The gold was then patterned by a quick UV photolithography process using a simple photo mask and chemically etched. The resulting flexible "thin film" wire strips had low electrical resistance < 0.1Ω. Small beads of indium were used to make connection to the contact pads of the readout gradiometer. Press contact between the Au on Mylar and the readout was made on a hot plate at 125 C which, aside from helping to make good electrical contact, also ensures that the indium forms a bond with both Au layers providing good adhesion. On the opposite end, the Au layer makes contact to a copper pad, again using an indium solder joint, on a PCB mounted into the holder as shown in finished device with the flip-chip antenna on top. The overall separation between the two layers is ~85 μm. Figure 34(a) shows two photographs take under the microscope of the electrical connection using the Au on Mylar prior to flip-chip coupling of the gradiometric antenna. Figure 34(b) shows the device mounted in the holder.

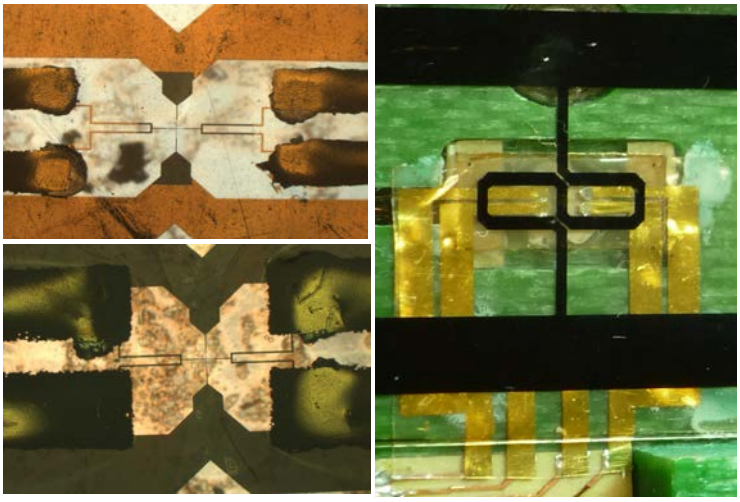

Figure 34. (a) Two readout gradiometers with Au on Mylar connections and (b) a finished flip-chip gradiometer showing a close up of the Au on Mylar between the readout and the antenna.

5.4.2 SQUID READOUT - FLUX-LOCKED LOOP - MAGNICON

The SQUID gradiometers are operated using a read-out scheme known as a Flux-Locked Loop (FLL). Since the output of a SQUID as a function of applied flux is nonlinear and periodic, the FLL can be employed to linearise the V-Φ response and also significantly increase the dynamic range. The flux feedback opposes the flux being measured to the keep the flux at the SQUID constant: the output voltage V_{OUT} measured across the feedback resistor R_F becomes a linear function of the measured flux. The FLL enables one to track changes in flux corresponding to many flux quanta, and also to detect changes in flux corresponding to a tiny fraction of a flux quanta thus increasing the dynamic range of the SQUID significantly. Another major benefit of the FLL is that the voltage noise of a good pre-amplifier becomes negligible compared with the transformer amplified voltage noise output of the SQUID. FLL operation thus enables the measurement of the intrinsic noise characteristics of the dc SQUID. We are using FLL electronics supplied by Magnicon GmbH. Figure 35 shows the setup electronics for a three channel system. Five of these systems are required for the 15 sensor OCEANMAG system. Note one pc connection cable can be used when the connector boxes are daisy chained together.

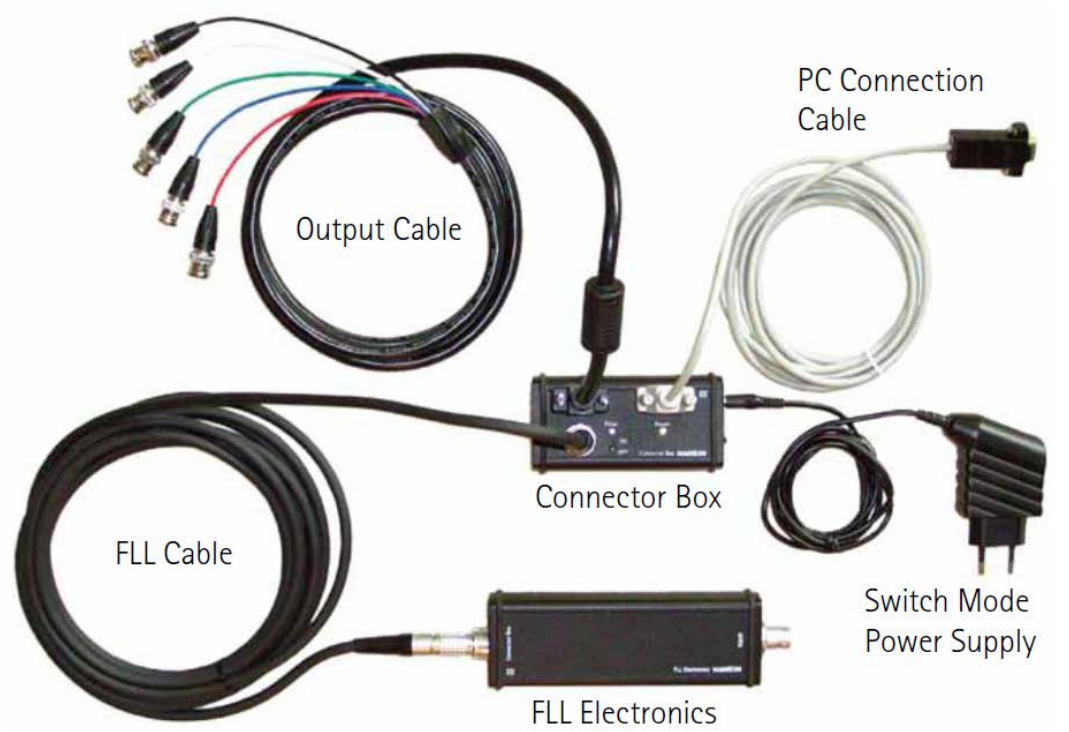

Figure 35. Shows a picture of the Magnicon FLL electronics setup.

5.4.3 AC VS DC BIASING MODES

In addition to the intrinsic white flux noise which is essential flat out to MHz, HTS SQUIDs exhibit a strong frequency dependent noise contribution, in the form of 1/*f* noise that can degrade SQUID performance at low frequencies. The onset of this noise commonly known as the 1/*f* knee usually depends on the nature of the SQUID, thin-film quality and the

operating temperature, but can also be dependent on the ambient magnetic field when the SQUID in cooled.

There are two known sources of intrinsic noise in dc SQUIDs which have a 1/*f* dependence. The first source arises from fluctuations in the critical current I_C of the junctions. These fluctuations are believed to be related to the trapping and releasing of charge carriers by defects in the barrier which raise and lower the barrier potential, in turn affecting the critical current of the junction changing the level between discrete values similar to random telegraph noise. Fortunately, this noise source can be substantially suppressed by using an AC bias reversal technique. Using the ac-bias technique the SQUID is biased with a current periodically switched between $+I_B$ and $-I_B$ at a frequency of f_B, while the feedback electronics lock the flux in the SQUID. This technique is highly effective at removing excessive levels of 1/f noise in our step edge junctions as demonstrated in Figure 36 which shows the same device noise using both the basic dc biasing and the ac biasing technique. dc biased the 1/f knee extends out well beyond 1 kHz where using ac biasing the response remains flat down to roughly 4-5 Hz. This measurement was taken inside three layers of mu-metal shielding.

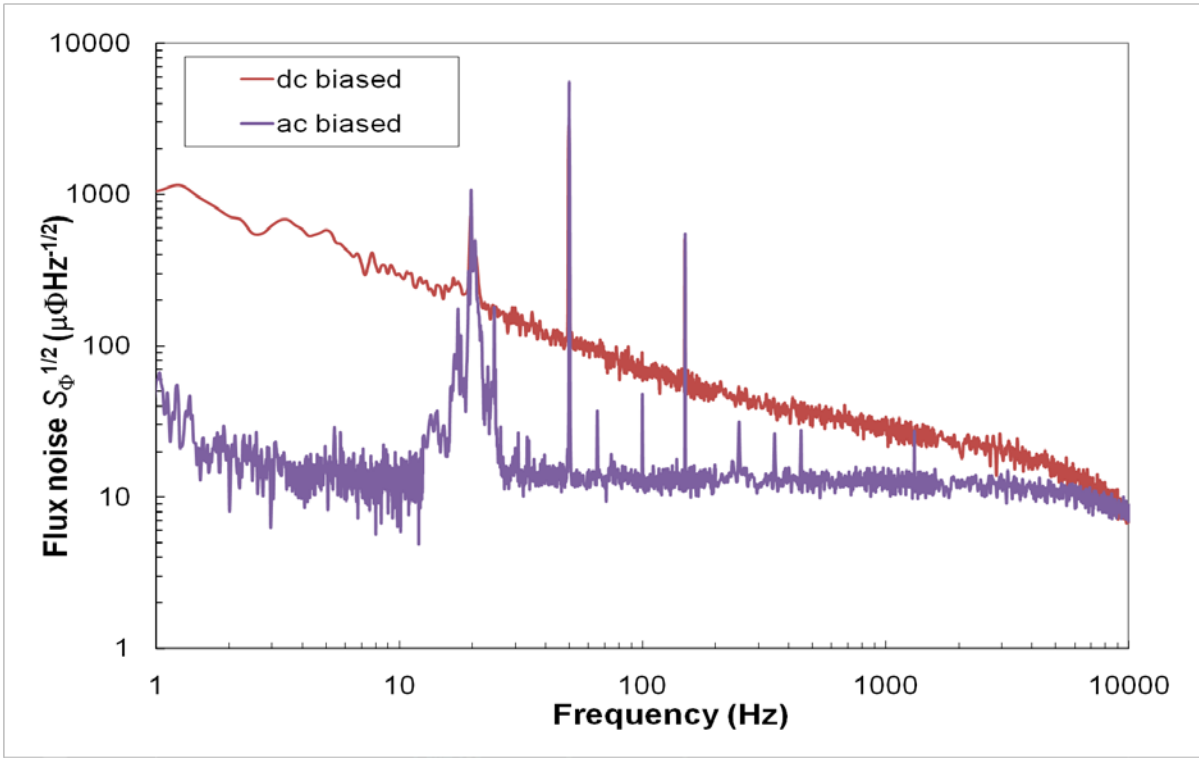

Figure 36. Flux noise spectral density of gradiometer G3 measured inside three layers of mu-metal shielded using both the basic dc biasing and the ac biasing technique (note the broad peaks in the spectrum between 10-30 Hz are caused by a variable speed rotating magnet in the next room).

The second source of 1/*f* noise, which is worth mentioning here, arises from thermally activated hopping of flux between pinning sites in the superconducting thin-film of the SQUID. These flux vortices are usually pinned at defect sites such as an impurity in the material, but in the presence of thermal excitations the vortex can jump to the next site. The distribution of the pinning site activation energies has a broad Lorentzian spectrum, which results in a 1/*f* distribution. The flux motion due to vortex hopping couples to the SQUID as real flux, and therefore cannot be eliminated by the ac bias modulation. A number of

precautions have been taken to reduce this source of noise. The microstructural quality of the thin film is important as we can restrict the movement of the vortices by increasing the thermal energy required for a vortex to leave a pinning site. Higher quality films contain a high density of effective intrinsic pinning sites therefore we have ensured that the film quality we use is of the highest standard. From the design point of view we use only narrow linewidth SQUIDs for all our devices, by reducing all track widths $w \leq 4$ μm theoretically flux vortices cannot become trapped in the thin film as it is energetically unfavourable for them to penetrate. We have seen this to be true when cooled in fields of up to 100 μT. In unshielded conditions the film edge quality plays an important role in vortex entry. Poor quality edges (generally referring to smoothly bevelled edges) tend to provide low-energy sites where flux vortices can enter and nucleate which reduces the threshold for field exclusion for narrow linewidth structures. The edges should be vertical to give the highest field threshold. We have paid particular attention to ensure our edge quality is good when fabricating.

Figure 36 highlights the necessity of using effective ac biasing on all devices to obtain the best low frequency performance for our devices. Initially we experienced difficulties in optimising the SQUID tuning parameters and reliably locking some of the devices in the ac biasing mode. However, through dialogue with Magnicon we resolved these issues and as a result have much greater control over the setup parameters, such as increased bias voltage Vb, bias flux Phib and offset flux Phi0 ranges to optimise the best working point for each device. Issues arose in some devices from increased offset resistance from the wiring resulting in an offset voltage in the AC biasing mode, compensation voltage offsets have now been pre-programmed in the software for each channel on start-up allowing each device to lock into ac biasing mode without retuning.

In an unshielded environment, in which the SQUID is exposed to the magnetic noise of the environment an important figure of merit is the slew rate, i.e. the maximum rate of change of flux the system is able to track without losing lock. If the electronics cannot change the feedback current fast enough, it is possible that they could end up at a different point on the V-Φ curve (same V, different Φ). This artefact is commonly known as flux jumping. We have measured a slew rate of ~2.7 mT/s using the Magnicon electronics in conjunction with a 3 mm SQUID magnetometer which will be more than sufficient to track field changes experienced in motion during a magnetic survey unless in a highly perturbed environment.

The devices were individual tested prior to assembly of the tensor system. These tests included shielded and unshielded noise measurements, field gradient calibration, parasitic field and gradient area calculation. This testing was carried out on the read-out gradiometer before and after the antenna was flip-chip coupled.

Testing the intrinsic noise of the devices is done inside several layers of mu-metal shielding also with rf shielding.

Figure 40 shows test results for device #5. Note: the increase in noise with the antenna in an unshielded environment is a combination of the critical current fluctuations from the use of DC biasing and increased background noise sensitivity of the lab environment. AC biasing could be achieved at that time in shielding only.

5.4.4 DETERMINING THE GRADIENT SENSITIVITY OF THE FLIP-CHIP GRADIOMETER

The sensitivity of the flip-chip gradiometers was calculated in two separate ways. In the first method, various parameters from the devices such as SQUID noise $S_\Phi^{1/2}$, effective area A_{EFF} and flip-chip gain were used to indirectly determine the gradient sensitivity. In the second method we determined the voltage to gradient field transfer functions by applying known gradient fields (note this was performed after the system was assembled, the method is fully discussed in section 6.9).

Individual testing

As discussed Section 5.1, the gradient field sensitivity, $S_G^{1/2}$, of the flip-chip gradiometers is proportional to $S_\Phi^{1/2} / (A_{EFF} \times l)$, where $S_\Phi^{1/2}$ is the SQUID's flux noise, A_{EFF} is the effective sensing area and l is the baseline. Determining the actual effective sensing area of the flip-chip by direct measurement is difficult as this involves removing one of the device pickup loops (effectively destroying the device) and measuring the response to a known calibrated field. This might be out the question for the large antenna due to the cost of such a structure; however, it was possible to remove a pickup loop from a readout device instead. Figure 37 shows one such device where the one of the loop has been chemically wet etched using orthophosphoric acid.

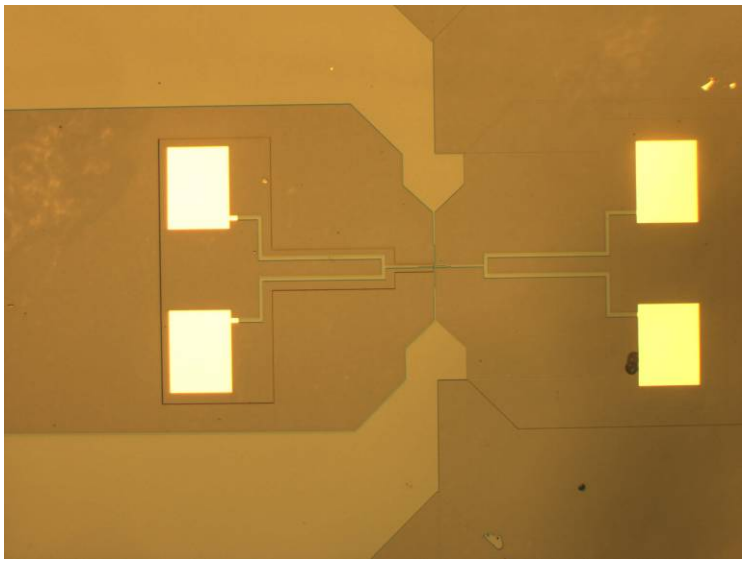

Figure 37. A readout device with its pickup loop removed.

The measured effective area of the SQUID readout design B incorporating SQUID 2 was 0.122 mm^2 and the same design B incorporating SQUID 3 was 0.164 mm^2. Using this effective area, the baseline and the measured flux noise, we can infer the gradient sensitivity for the readout gradiometer of the same design. The response of the readout gradiometer to a well defined magnetic source, at a constant standoff r, was measured. The source chosen was made from two 2 m lengths of wire separated by 15 mm in the plane of the gradiometer as schematically shown in Figure 38. An ac current at 8 Hz was passed through one wire and back through the other generating a diagonal gradient field.

This measurement was then repeated using the flip-chip device with the same standoff. Comparing the two responses gives a measure of the increased responsivity. The plot shown in Figure 39 gives the response of the readout gradiometer with and without the antenna coupled showing that an increase of 28.7 was obtained for device #5. Given the increase in

sensing area and baseline of the design C antenna over design B, the improvement in responsivity (that is the ($A_{EFF} \times l$) product) was expected to be as much as 40% over our previous design (B). Test measurements confirm this to be closer to 50-55%. These flip-chip devices show an average of increase of ~31 times the response seen by the read-out gradiometer alone (compared with ~19.5 for design B). Using this we can estimate the gradient sensitivity $S_G^{1/2}$ of the device. For device #5, shown in Figure 39 , $S_G^{1/2}$ ~ 2.3 pT m^{-1} $Hz^{-1/2}$ at ~10 Hz (in shielding) based on a $S_\Phi^{1/2}$ of ~ 16 $\mu\Phi_0$ $Hz^{-1/2}$.

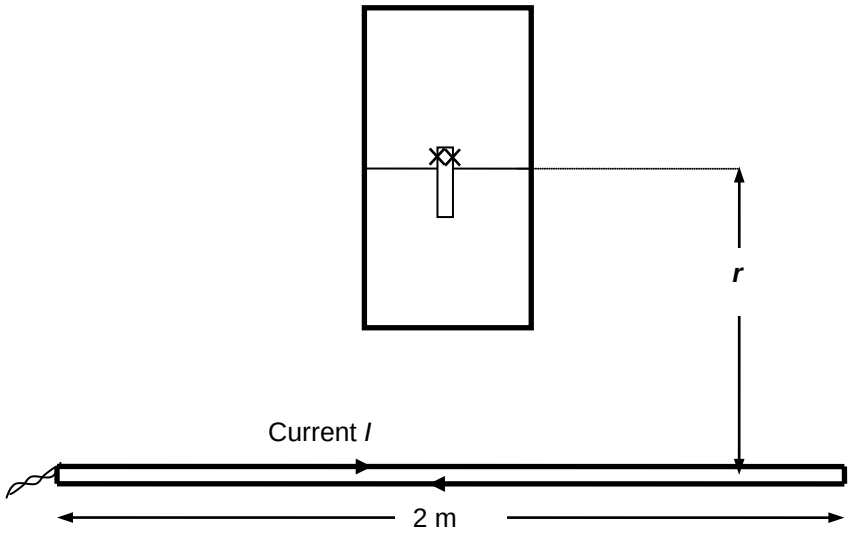

Figure 38. A schematic showing the experimental setup for measuring the response of the readout gradiometer to a well defined magnetic source, at a standoff *r*. The source was made from two 2 m lengths of wire, separated by 15 mm, positioned in the plane of the gradiometer.

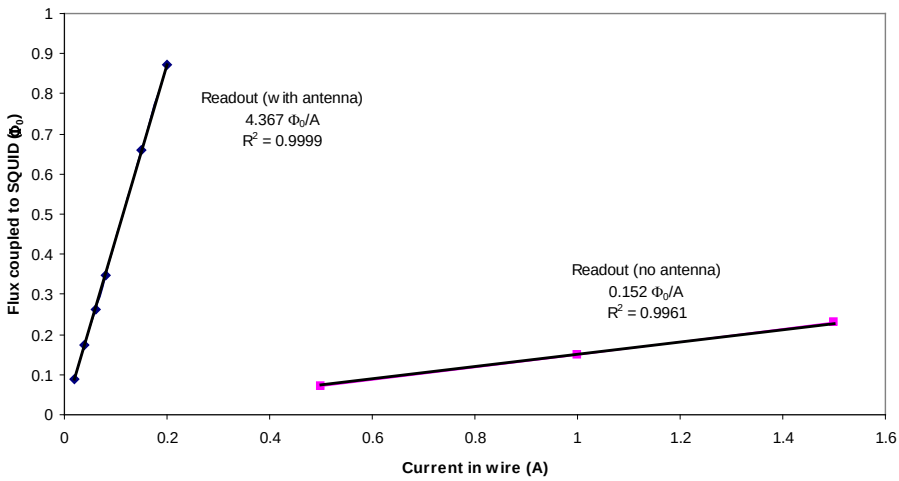

Figure 39. The readout gradiometers (with and without the flip-chip antenna) response to a defined magnetic source. The flip-chip device shows a ~28.7 times improvement over that of the readout gradiometer (JLOM14(I) #5)

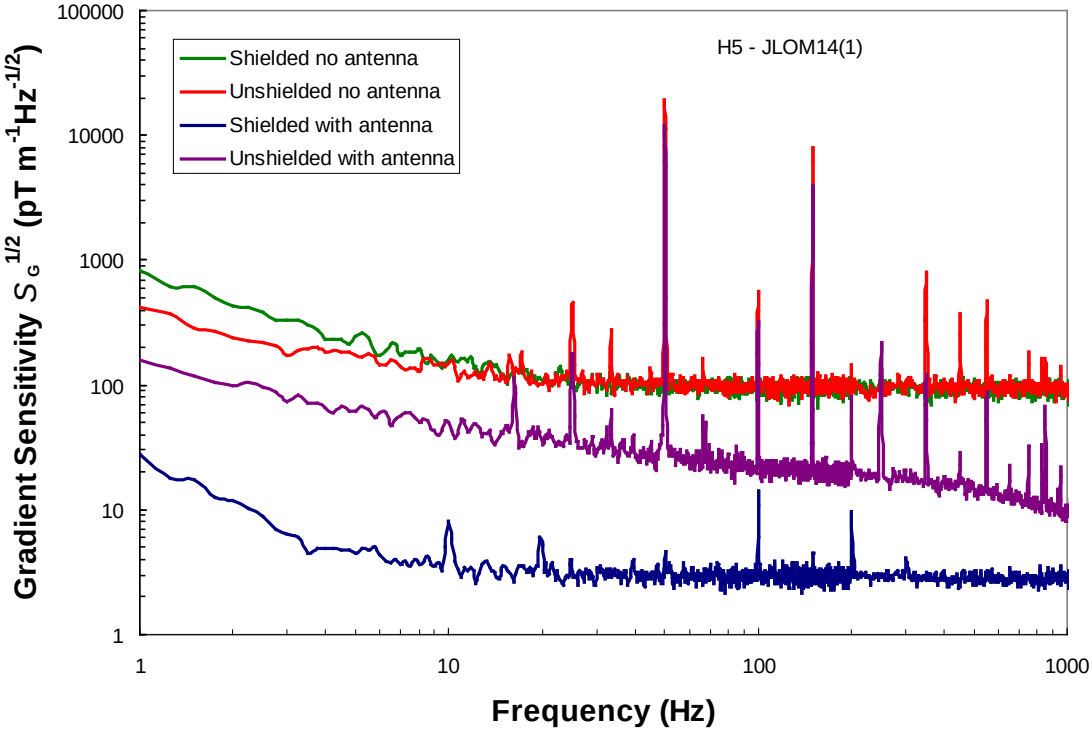

Figure 40. The measured gradient noise of a readout gradiometer (#5) before and after it has been flip-chip coupled shown both inside mu-metal shielding and completely unshielded. The gradient noise is extrapolated from the flux noise.(note curve "unshielded with antenna" is dc biased only).

Note, initial unshielded device testing in the open laboratory (and also in shielded environments in several layers of mu-metal shielding which provides good low frequency shielding), revealed strong suppression of the voltage-flux modulation in a number of the devices. This behaviour was indicative of the presence of large amounts of rf interference. Efforts were made to shield the test system from rf interference which improved individual device performances dramatically. Based on this experience, we added additional RF shielding to the Dewar which holds the pyramid (this issue is further discussed in Section 6.5). Table 5 summarised the six flip-chip gradiometers fabricated, however gain factors were not directly measured for G1 and G4. The values shown in Table 5 are determined using the average gain of 31.5. The best performing device has a gradient sensitivity ~ 1.95 pTm^{-1}Hz$^{-1/2}$ (determined using this calibration method) at 10 Hz in a shielded environment.

Table 5. Summary of the six flip-chip devices (note H1 and H4 were not determined using this method)

	Ic (μA)	Rn (Ω)	ΔV (μV)	$S_\Phi^{1/2}$ @ 10 Hz ($\mu\Phi Hz^{-1/2}$)	Gain factor	$S_G^{1/2}$ @ 10 Hz ($pTm^{-1}Hz^{-1/2}$) Shielded AC biased	$S_G^{1/2}$ @ 10 Hz ($pTm^{-1}Hz^{-1/2}$) Unshielded
G1	45	5.6	29	12	31.5*	2.19*	55*
G2	35	6.6	6.2	16	28.7	3.30	45
G3	30	6	18	14	30.9	2.07	48
G4	17	5.5	23	12	31.5*	2.77*	51*
H5	30	7.2	7	16	32.4	2.26	44
H6	20	5.6	9.8	13.5	33.5	1.95	42

* Gain factors were not directly measured for G1 and G4, values shown are determined using the average gain 31.5.

The following section describes the full tensor system assembly and aspects dealing with system calibration and testing.

6 Magnetic tensor gradiometer

6.1 System overview

Figure 41 shows a basic schematic diagram of the Tensor gradiometer system. The superconducting tensor gradiometer is mounted inside an evacuated LN_2 glass Dewar in cased with a rf shielded housing. The main lid contains the connection to the SQUID electronics, the outputs of which are recorded by a 24-bit ADC. Both the acquisition and SQUID electronics are controlled from the pc, allowing the user to monitor the SQUID outputs and capture data quickly and easily.

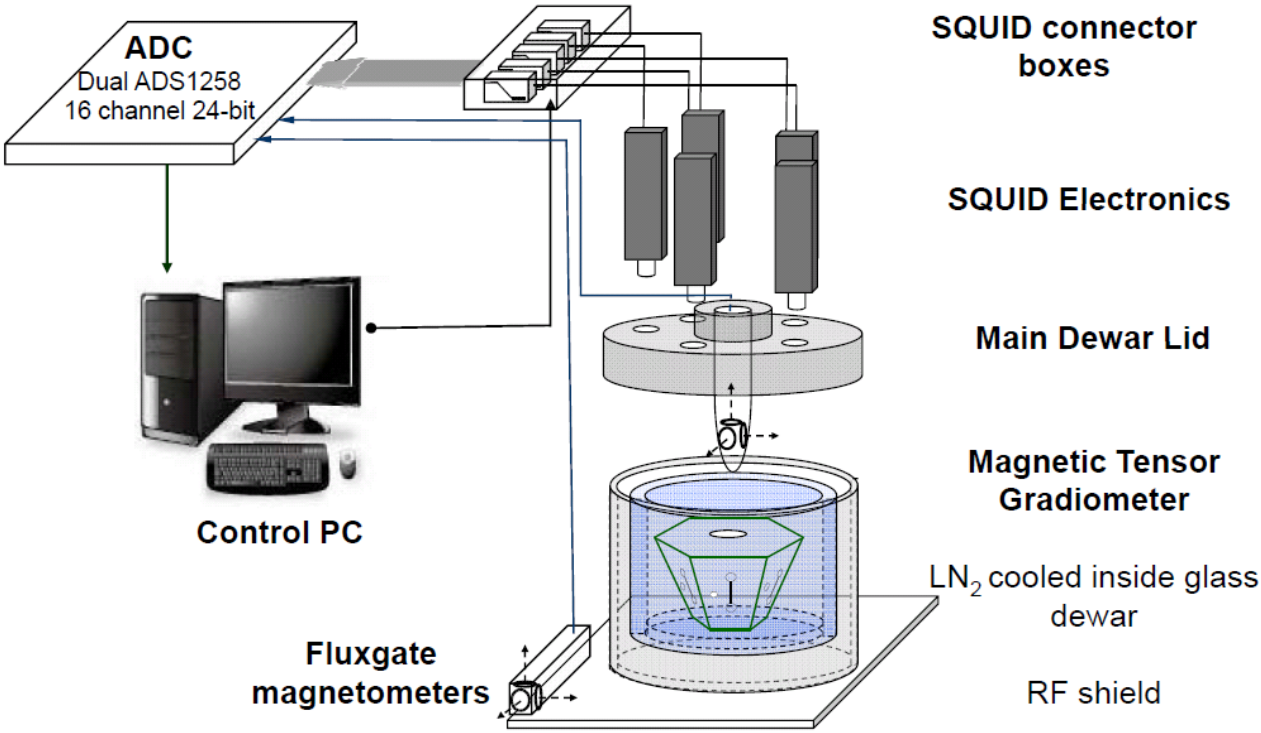

Figure 41. Schematic diagram of the tensor gradiometer system.

The Dewar lid contains five 24-way LEMO connectors to which the Magnicon SQUID electronics can be plugged either directly into or via 1.5 m long extension cables (included to allow for a feedback coil set to surround the system). Each Magnicon electronics set contains three channels thus enabling a total of fifteen individual SQUIDs to be modulated simultaneously. The OCEANMAG system is mounted inside the glass Dewar using a base plate which is glued to the glass and the pyramid mounted to this using nylon screws. The top of the truncated hexagonal pyramid is attached at the base of the Dewar (thus the system is essentially upside down) as shown in Figure 43 and Figure 44, this allows easy access to wiring from the outside without having to dismount the system completely. The outside casing is constructed from molded plastic and the inside is coated with several thin layers of silver paint which provided good rf shielding. The inside of the Dewar lid also coated in a similar fashion and electrically connected to the base and the LEMO connectors thus completely surrounding the system (see later section 6.5 for more information).

6.2 Brief description of operation

The gradient tensor of the magnetic field **B** has nine components

$$\mathbf{G} = \begin{bmatrix} B_{xx} & B_{xy} & B_{xz} \\ B_{yx} & B_{yy} & B_{yz} \\ B_{zx} & B_{zy} & B_{zz} \end{bmatrix} = \begin{bmatrix} \frac{\partial B_x}{\partial x} & \frac{\partial B_y}{\partial x} & \frac{\partial B_z}{\partial x} \\ \frac{\partial B_x}{\partial y} & \frac{\partial B_y}{\partial y} & \frac{\partial B_z}{\partial y} \\ \frac{\partial B_x}{\partial z} & \frac{\partial B_y}{\partial z} & \frac{\partial B_z}{\partial z} \end{bmatrix} \tag{9}$$

For quasi-static field measurements in air (or free space), where conduction currents and convection currents are absent and displacement currents are negligible, the magnetic gradient tensor is symmetric as well as traceless. In this case, the tensor only has five independent components (e.g., B_{xx}, B_{yy}, B_{xy}, B_{xz}, B_{yz}). These include two diagonal and three off-diagonal components. Due to the ceramic nature of HTS materials using conventional technology, we can easily only form planar devices, gradiometers of which only measure the off-diagonal components of the gradient tensor which makes it difficult to determine the diagonal components. However, Eschner and Ludwig (1995a) showed that by using at least five planar gradiometers positioned on at least three non-parallel surfaces, one can calculate all components of the gradient tensor (Figure 42(a)). Clark (2008) confirms that the optimal inclinations of pyramidal faces, as described in this patent, are about 30° for arrays of five gradiometers on a pentagonal pyramid or for six gradiometers on a hexagonal pyramid. Our design uses an array of six planar SQUID gradiometers positioned on the slant faces of a truncated hexagonal pyramid (Figure 42(b)). This provides data redundancy leading to an over-determined system of linear equations for calculating the tensor components.

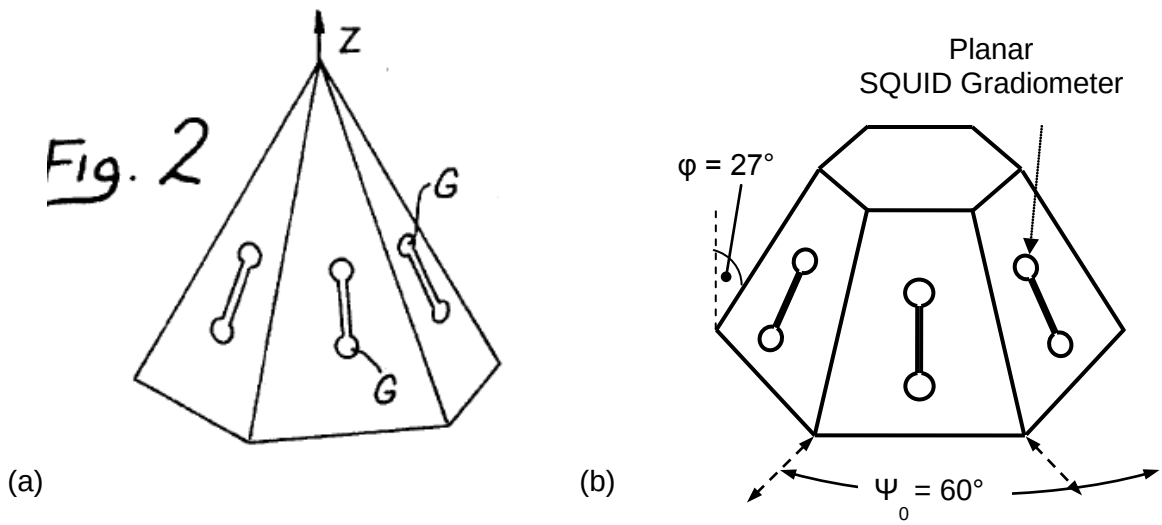

Figure 42. (a) Sketch of the tensor gradiometer with planar gradiometer, G, on the slanting faces of the polygonal pyramid (from Eschner and Ludwig, 1995b). (b) Optimal geometry for a hexagonal pyramid.

The fibreglass hexagonal pyramid frame is shown in Figure 43(a) prior to assembly of the system. Also shown is the mini-Dewar design to house 3 orthogonal AMR sensors and maintain at room temperature (see Section 8 Global feedback system for further information). There are six gradiometer housings for each face of the pyramid. In addition to a gradiometer and a magnetometer, each housing has integrated modulation coils, three individually designed heaters and a PCB connector, as shown in Figure 43(b).

There are the three “on-chip” heater coils: two for the gradiometer and one for the magnetometer. These three heaters, made from bifilar wound Constantan wire, are wired in series to allow simultaneous heating of both devices to release trapped magnetic flux (potential source of excess 1/f noise). The gradiometer antenna has a large heater coil placed along the central baseline which releases flux from both loops simultaneously. Heating might be necessary if the devices see a sudden change in magnetic field which can lead to a decrease in device stability and increased noise. Heating times are of the order of 8-10 s for the flip-chip gradiometer and a further 20 s for re-cooling.

The modulation coil for the gradiometer is a small 3 turn coil underneath one pickup loop of the readout gradiometer. This provides good coupling of the FLL feedback signal with an average coupling coefficient of ~ 60 $\mu A/\Phi_0$. The magnetometer has an integrated superconducting feedback coil.

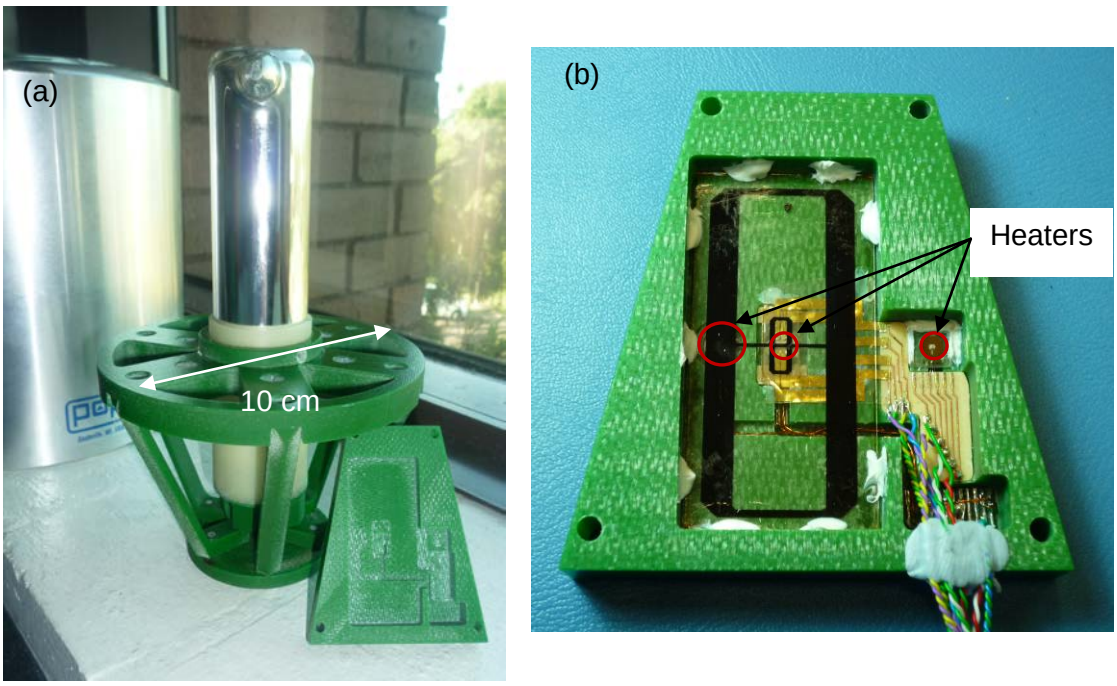

Figure 43. (a) Picture of the Dewar, pyramid (dimensions shown) and gradiometer holders prior to mounting and assembly of the system. (note shown also is the mini Dewar which allows room temperature AMR sensors to be positioned at the centre of the pyramid designed for use with a feedback system). (b) a picture of an assembled flip-chip gradiometer showing the position of the heater coils.

Figure 44. Wiring for the full system, with a total 108 wires (54 twisted pairs).

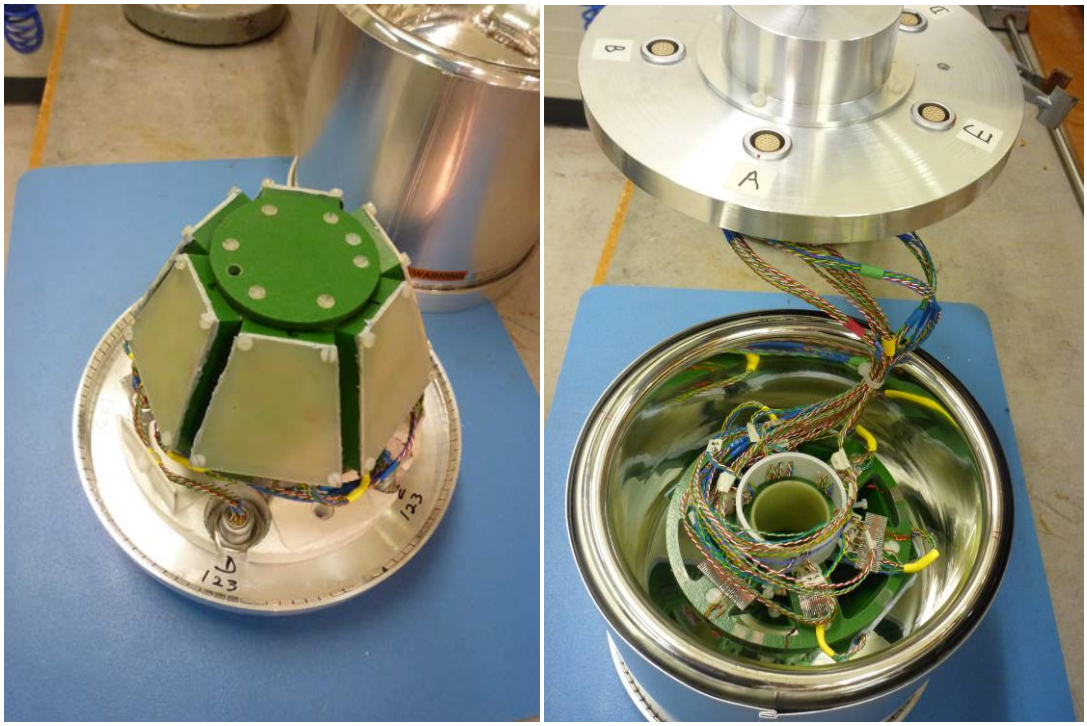

Figure 45. The hexagonal pyramid with six gradiometers dismounted and mounted inside the Dewar. The wiring is connected to the outside via five 24-way LEMO connectors.

6.3 Ancillary reference sensors – 3 mm SQUID magnetometers

The gradiometers finite common mode rejection causes motion noise when the system is subject to magnetic field change, such as seen during motion in the Earth's magnetic field. The ability to accurately measure background field changes as the system is in motion is crucial for our compensation to work effectively. This system contains nine 3 mm dc SQUID magnetometers (Figure 46 (a)) which are positioned around the system to give an extremely accurate measure of the local background field. There are six in-plane magnetometers on each face and three orthogonal magnetometers at the top of the truncated hexagonal pyramid, as shown in Figure 46 and Figure 43 (a). Figure 46 (c) shows a noise spectra for a typical magnetometer unshielded and shielded (inside mumetal) in our laboratory and unshielded in a remote test location (West Head). The calibration procedure aims to correlate changes in the magnetic field with the response from the gradiometers to determine a set of coefficients.

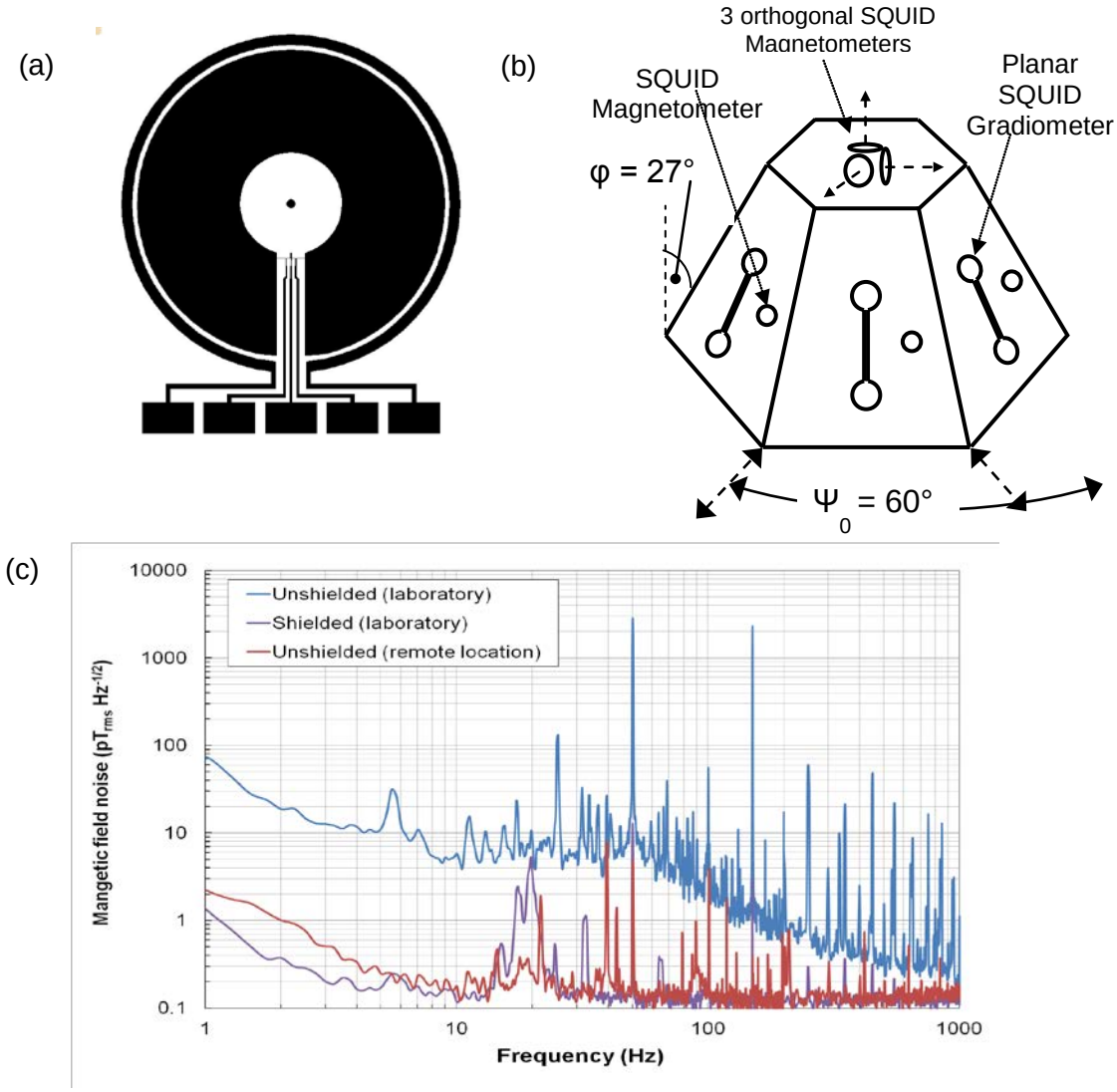

Figure 46 (a) shows the YBCO pattern on the 3 mm dc SQUID magnetometers used as reference sensors. (b) Shows the positioning of the field sensors on system using a wire diagram representation (which includes the gradiometer sensors also) and (c) shows the field noise spectra for a typical 3 mm magnetometer, unshielded and shielded in the lab and also in a remote test location (West Head).

6.4 Wiring

The full system (Figure 47) has a total of 108 wires (54 twisted pairs). For the Tensor gradiometer (× 6 devices) there are six wires for each flip-chip gradiometer, four electrical connections (±V, ± I) to the SQUID and two for the modulation coil (6 × 6 = 36). For the in-plane compensation Magnetometers (× 6 devices) again there is six wires for each magnetometer, four electrical connections to the SQUID and two for the modulation coil (6 × 6 = 36). For the orthogonal magnetometers (× 3 devices), there are again six wires for each device (6 × 3 = 18). The system contains 21 heaters in total, however the three heaters on each gradiometer holder are wired in series and act as one heater, therefore there are effectively nine heaters with two wires for each heater set, (9 × 2 = 18). Note that the feedback and the modulation signal are coupled to the SQUID using the same coil. Note using the Magnicon electronics only ± V connections are required for operation however additional electrical connections were provided to allow the devices to be compatible with the Star Cyroelectronics FLL system also which requires four connections to the SQUID. Figure 47(a) shows the SQUID wiring diagram for the Magnicon setup along with a pin connection diagram for the 24 way LEMO connector (b).

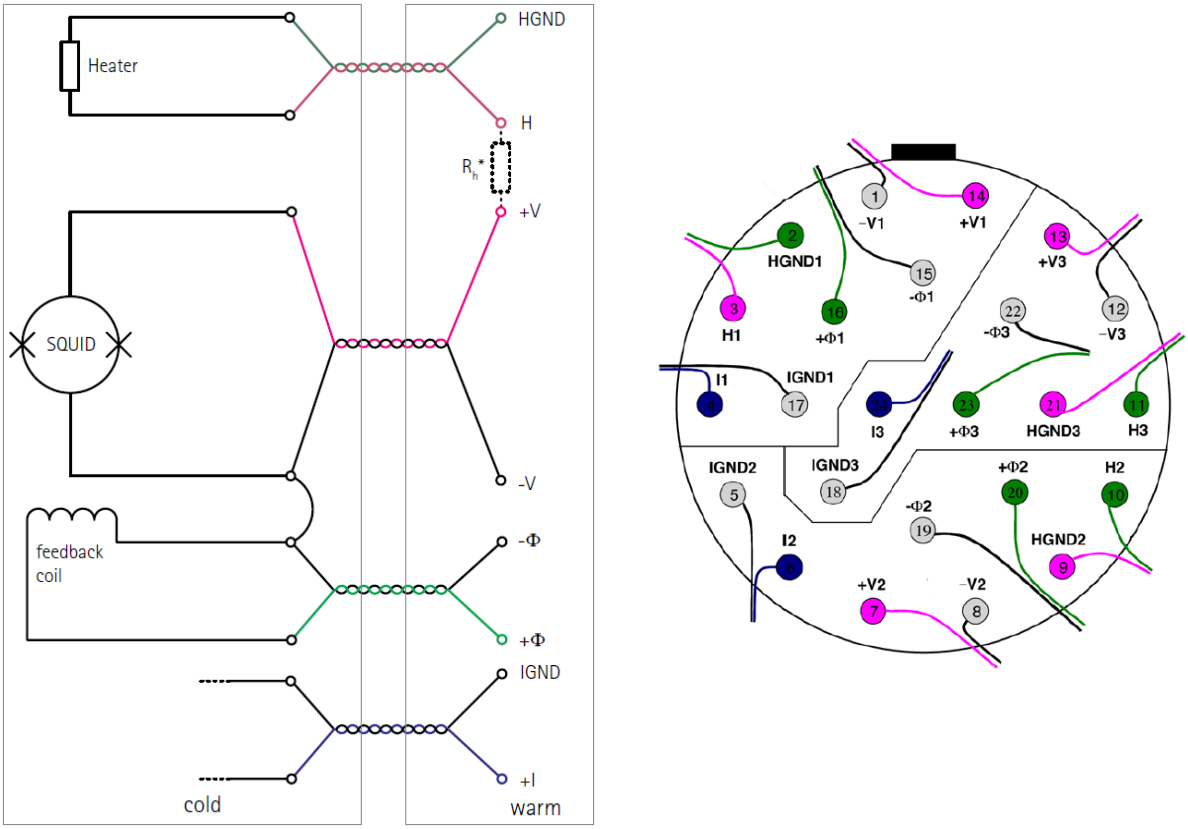

Figure 47. (a) The wiring diagram for the dc SQUID gradiometers using Magnicon electronics and (b) the pin connection diagram for the 24-way 3-channel LEMO connector.

6.5 RF shielding

One of the main problems in a lot of SQUID measurement setups is rf interference. Sources of rf interferences can be e.g. television signal transmitters, mobile phones, and electrical devices. All SQUID sensors are sensitive to these disturbances which can cause the I-V curve to be somewhat rounded and the SQUID modulation may be reduced or even fully suppressed if the rf interference level is high enough and/or allowed to reach the SQUID. In all cases, even if the device is of a very high quality and can be operated magnetically unshielded, a good electrical rf shield around the sensor is crucial. Additionally it is important, to have a good electrical connection between the plug socket for the FLL electronics and the rf shield of the Dewar.

Initially the Dewar was encased using an aluminium shield. A base plate and lid, with a thickness of ~3 mm, were fabricated to work in conjunction with the original manufactures aluminium side cladding (~ 1.5 mm thick) providing a good solid and highly attenuating rf shield. However, after initial calibration of the system using applied low frequency magnetic fields we observed large phase shifts in the gradiometer outputs as shown in Figure 48 (a) where an 8 Hz uniform magnetic field is applied to the system. This was due to large circulating eddy currents being generated in the aluminium causing small localised magnetic fields to produced which are out of phase with the applied signal.

After identifying the problem, immediate steps were taken to replace the aluminium with a suitable alternative. We fabricated a moulded plastic casing to house the Dewar the inside of which was coated with several layers of thin silver paint. This method has been used in the past with a good deal of success. Figure 48 (b) shows gradiometer responses to an 8 Hz uniform magnetic field using the new rf shielding demonstrating a significant reduction in phase lag between the measured signals.

We are currently evaluating new rf shielding materials, such as pure copper polyester fabric which is only 0.08 mm thick and provides 80 dB attenuation (10 – 3000 MHz) of rf signals and can be easily incorporated into the Dewar.

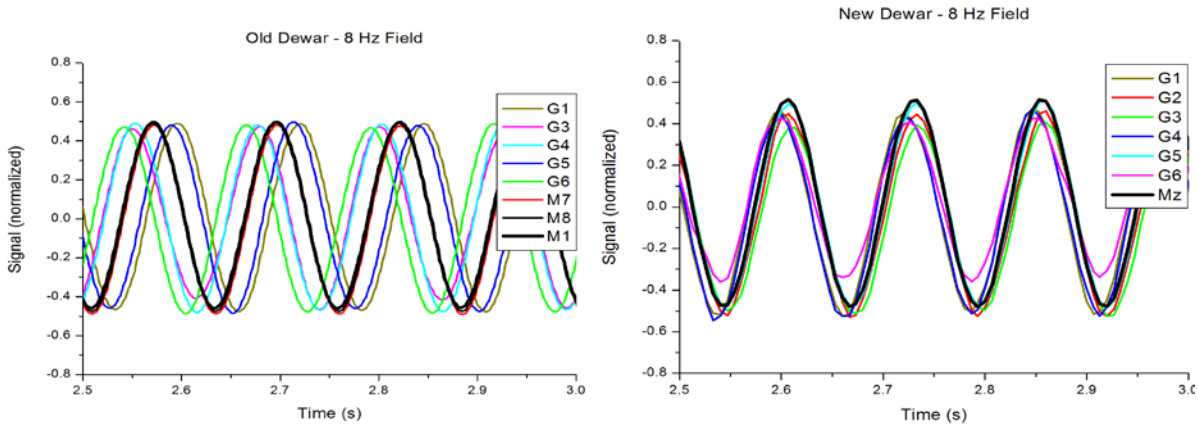

(a) (b)

Figure 48. Plots showing the normalised response of the gradiometers to an applied 8 Hz uniform magnetic field for (a) the original aluminium shielding and (b) the new silver shielding.

6.6 Acquiring data – dual channel 24-bit ADC

The data acquisition system electronics was designed to interface to high temperature SQUID electronics supplied by Magnicon, the SEL-1. The SEL-1 is controlled using an RS-485 serial interface with a command set consisting of string based instructions. Each Magnicon unit is capable of controlling 3 axes and up to 254 units may be connected in parallel. The analogue output from the Magnicon is a +-10V signal over a BNC cable and a 10 KHz anti-aliasing filter may be enabled using a switch on each unit.

Our in-house electronics consists of an Altera Cyclone III FGPA connected to an ADS1258 24 bit analogue to digital converter (Figure 49 (a)). This A/D chip has 16-channel multiplexed input and can digitise at a maximum rate of 23.7kSPS/Channel. The converter uses a delta-sigma conversion scheme. Data from the A/D is averaged by the FPGA to reduce the sampling rate down to 30SPS, although this slower rate may be set to other values. The data can then be stored real-time to an SD card or transferred real-time over an RS232 link back to a PC. Real-time acquisition is limited to 2000 SPS/channel over the RS232 link and 4500 SPS/Channel to the SD card. The data logger also has a USB "on the go" port, which in the future may be used for much higher transfer rates or logging to an external USB memory stick.The data acquisition system uses a maximum of 180mA from a 12VDC supply. It is based on the Altera Cyclone III starter kit. The FPGA design incorporates a softcore NIOS II 32bit processor and custom components written in Verilog for the ADS1258, a digital temperature sensor (TSIC506) and a UUencoder module to translate data from 8-bits to 7-bits for the serial link. Two serial ports are on the data acquisition system, one for interfacing to the Magnicons using an RS485-RS232 converter and the other to connect to the PC. The Magnicon instruction set was expanded to allow software on a PC to control both the FPGA and the Magncon using the one port. The FPGA can receive commands meant for the Magnicon on the PC port and pass them on to the serial connection for the Magnicon and then pass back any responses. This enables only a single serial link to a PC for remote data logging.

A dual ADS1258 FPGA based data logger is being developed to supersede the previous system in order to decrease the noise resolution per channel. It uses the same system as described above, but is capable of interfacing to 32 channels and by running the ADS2158 chips in parallel, it can effectively double the maximum sampling rate when sampling multiple channels.

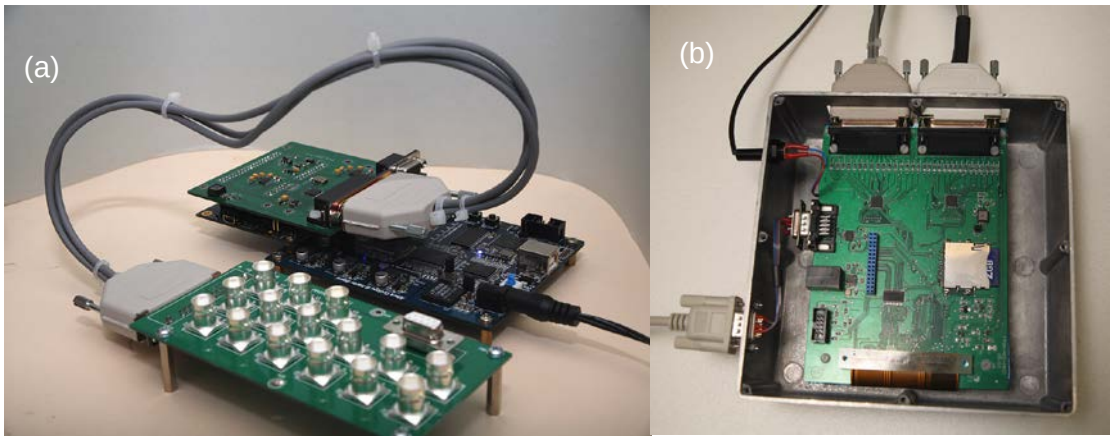

Figure 49. (a) Picture of the in-house developed 24-bit ADC and (b) the 24-bit dual channel ADC.

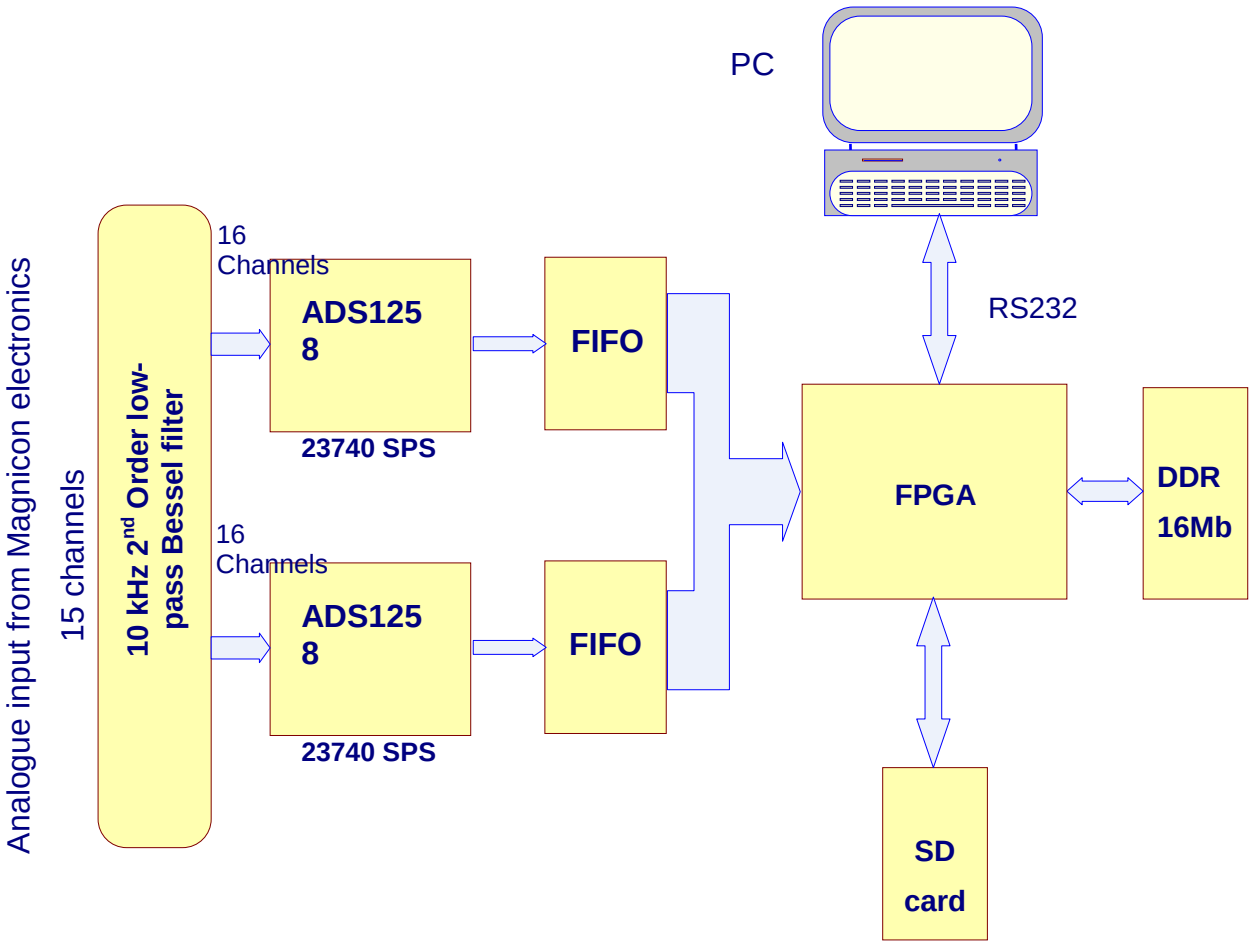

Figure 50. A flow diagram of the in-house developed dual ADS1258 24-bit ADC.

6.7 Theoretical aspects of calibration, referencing and field compensation

The magnetic tensor gradiometer system comprises of an array of six planar gradiometers, symmetrically disposed about a single downward-pointing axis, which we label Z. Each gradiometer sensor lies on the slanting face of a hexagonal pyramid, with its long (displacement) axis making an angle of φ with the *z* axis. The planar gradiometers are labelled with indices *k* = 1, 2, …, 6. The normals to the sloping faces are denoted $\hat{\mathbf{n}}_k$. As well as a planar gradiometer, each sloping face of the pyramidal prism is equipped with a referencing SQUID magnetometer M_k (*k* = 1-6) with a sensitive axis along $\hat{\mathbf{n}}_k$. In addition, a two stage global feedback system, comprising triaxial AMR and SQUID compensation magnetometers that are designed to maintain the instrument in low magnetic field via a set of feedback coils, is emplaced within the pyramid.

The Cartesian instrument X, Y, Z axes are defined by the sensitive axes of the triaxial global feedback referencing magnetometer. The X and Y axes lie within the basal plane of the pyramid and are chosen to form a right-handed system, with Z vertical down. The geometry of the array and the labelling of the devices is depicted in plan view in Figure 51. The azimuth of the normal to face *k* with respect to the instrument X axis is denoted ψ_k.

Consider planar gradiometer G_k with long axis (displacement vector) and sensitive axes of the input loops both lying in the vertical plane. The downward-pointing displacement vector is labelled z'_k and makes an angle $\varphi \leq 90°$ with the vertical. The upward pointing sensitive axis, parallel to $\hat{\mathbf{n}}_k$, is labelled x'_k and the y'_k axis is horizontal, chosen to produce a right-handed system. Figure 52 shows a cross-section of a sloping face.

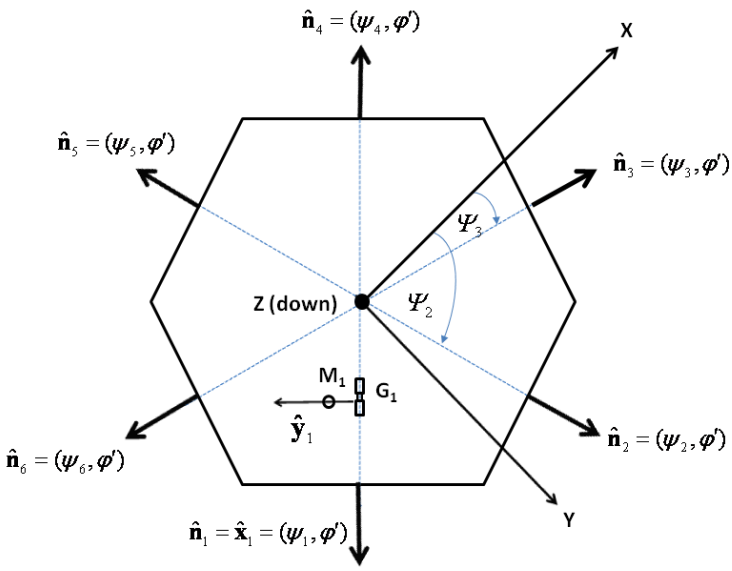

Figure 51. Schematic plan view of the hexagonal pyramidal array of gradient and field sensors, defining the azimuthal angles of upward normals to the sloping faces of the pyramid, relative to the instrument X axis (X referencing magnetometer axis).

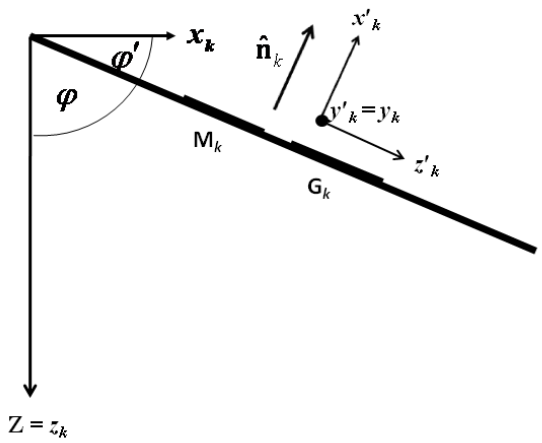

Figure 52. Cross-section of a sloping face of the hexagonal prism, defining co-ordinate axes for individual sensors. The magnetometer and gradiometer on face *k* measure $B_{x'_k}$ and $B_{x'_k z'_k}$ respectively.

The instrument XYZ axes are related to axes $x_k y_k z$ that are obtained by rotating through ψ_k about the *z* axis by:

$$\begin{aligned} \mathrm{X} &= x_k \cos\psi_k - y_k \sin\psi_k, \quad k = 1,2,\ldots,6, \\ \mathrm{Y} &= x_k \sin\psi_k + y_k \cos\psi_k, \quad k = 1,2,\ldots,6, \\ \mathrm{Z} &= z_k, \forall k. \end{aligned} \tag{1}$$

Individual sensor axes are related to $x_k y_k z_k$ by:

$$\begin{aligned} x_k &= x'_k \cos\varphi + z'_k \sin\varphi, \\ y_k &= y'_k, \\ z_k &= -x'_k \sin\varphi + z'_k \cos\varphi. \end{aligned} \tag{2}$$

which implies

$$\begin{aligned} \frac{\partial}{\partial x_k} &= \frac{\partial \mathrm{X}}{\partial x_k}\frac{\partial}{\partial \mathrm{X}} + \frac{\partial \mathrm{Y}}{\partial x_k}\frac{\partial}{\partial \mathrm{Y}} = \cos\psi_k \frac{\partial}{\partial \mathrm{X}} + \sin\psi_k \frac{\partial}{\partial \mathrm{Y}}, \\ \frac{\partial}{\partial y_k} &= \frac{\partial \mathrm{X}}{\partial y_k}\frac{\partial}{\partial \mathrm{X}} + \frac{\partial \mathrm{Y}}{\partial y_k}\frac{\partial}{\partial \mathrm{Y}} = -\sin\psi_k \frac{\partial}{\partial \mathrm{X}} + \cos\psi_k \frac{\partial}{\partial \mathrm{Y}}, \end{aligned} \tag{3}$$

and

$$\frac{\partial}{\partial x'_k} = \frac{\partial x_k}{\partial x'_k}\frac{\partial}{\partial x_k} + \frac{\partial z}{\partial x'_k}\frac{\partial}{\partial \mathrm{Z}} = \cos\varphi\frac{\partial}{\partial x_k} - \sin\varphi\frac{\partial}{\partial \mathrm{Z}}$$
$$= \cos\varphi\cos\psi_k\frac{\partial}{\partial \mathrm{X}} + \cos\varphi\sin\psi_k\frac{\partial}{\partial \mathrm{Y}} - \sin\varphi\frac{\partial}{\partial \mathrm{Z}},$$

(4)

$$\frac{\partial}{\partial z'_k} = \frac{\partial x_k}{\partial z'_k}\frac{\partial}{\partial x_k} + \frac{\partial z}{\partial z'_k}\frac{\partial}{\partial z} = \sin\varphi\frac{\partial}{\partial x_k} + \cos\varphi\frac{\partial}{\partial z}$$
$$= \sin\varphi\cos\psi_k\frac{\partial}{\partial \mathrm{X}} + \sin\varphi\sin\psi_k\frac{\partial}{\partial \mathrm{Y}} + \cos\varphi\frac{\partial}{\partial \mathrm{Z}}.$$

The magnetic field vector **B** and the gradient tensor **G** are, respectively, the first and second order gradients of a magnetic scalar potential *U*, i.e.

$$\mathbf{B} = (B_X, B_Y, B_Z) = \nabla U = (\frac{\partial U}{\partial X}, \frac{\partial U}{\partial Y}, \frac{\partial U}{\partial Z}),$$

$$\mathbf{G} = \begin{bmatrix} B_{XX} & B_{XY} & B_{XZ} \\ B_{XY} & B_{YY} & B_{YZ} \\ B_{XZ} & B_{YZ} & B_{ZZ} \end{bmatrix} = \nabla\nabla U = \begin{bmatrix} \frac{\partial^2 U}{\partial X^2} & \frac{\partial^2 U}{\partial X \partial Y} & \frac{\partial^2 U}{\partial X \partial Z} \\ \frac{\partial^2 U}{\partial X \partial Y} & \frac{\partial^2 U}{\partial Y^2} & \frac{\partial^2 U}{\partial Y \partial Z} \\ \frac{\partial^2 U}{\partial X \partial Z} & \frac{\partial^2 U}{\partial Y \partial Z} & \frac{\partial^2 U}{\partial Z^2} \end{bmatrix}. \tag{5}$$

Therefore the magnetic field component measured by M_k is:

$$B_{x'_k} = B_X\cos\varphi\cos\psi_k + B_Y\cos\varphi\sin\psi_k - B_Z\sin\varphi, \tag{6}$$

and the tensor component measured by the planar gradiometer G_k is related to the gradient tensor components in instrument co-ordinates by:

$$B_{x'_k z'_k} = \frac{\partial^2 U}{\partial x'_k \partial z'_k} = (\cos\varphi\cos\psi_k\frac{\partial}{\partial \mathrm{X}} + \cos\varphi\sin\psi_k\frac{\partial}{\partial \mathrm{Y}} - \sin\varphi\frac{\partial}{\partial \mathrm{Z}})$$
$$\times(\sin\varphi\cos\psi_k\frac{\partial}{\partial \mathrm{X}} + \sin\varphi\sin\psi_k\frac{\partial}{\partial \mathrm{Y}} + \cos\varphi\frac{\partial}{\partial \mathrm{Z}})U$$
$$= \cos\varphi\sin\varphi\left(\cos^2\psi_k\frac{\partial^2 U}{\partial X^2} - \frac{\partial^2 U}{\partial Z^2}\right) + 2\cos\varphi\sin\varphi\cos\psi_k\sin\psi_k\frac{\partial^2 U}{\partial Y \partial X} \tag{7}$$
$$+\left(\cos^2\varphi - \sin^2\varphi\right)\cos\psi_k\frac{\partial^2 U}{\partial Z \partial X} + \cos\varphi\sin\varphi\sin^2\psi_k\frac{\partial^2 U}{\partial Y^2} + \left(\cos^2\varphi - \sin^2\varphi\right)\sin\psi_k\frac{\partial^2 U}{\partial Z \partial Y}$$
$$= \frac{B_{XX}\cos^2\psi_k + B_{YY}\sin^2\psi_k - B_{ZZ}}{2}\sin(2\varphi) + \frac{\sin(2\varphi)\sin(2\psi_k)}{2}B_{XY} + \cos(2\varphi)\cos\psi_k B_{XZ}$$
$$+\cos(2\varphi)\sin\psi_k B_{YZ}.$$

Using the tracelessness property, this simplifies to:

$$B_{x'_k z'_k} = \frac{B_{XX}(1+\cos^2\psi_k) + B_{YY}(1+\sin^2\psi_k)}{2}\sin(2\varphi) + \frac{\sin(2\varphi)\sin(2\psi_k)}{2}B_{XY} + \cos(2\varphi)\cos\psi_k B_{XZ} + \cos(2\varphi)\sin\psi_k B_{YZ}. \quad (8)$$

Expression (8) for k = 1-6 gives six equations relating the calibrated, offset-free, sensor outputs to the gradient tensor elements in the instrument frame. The inverse relationships, giving the gradient tensor elements in terms of the planar gradiometer outputs, can be obtained by inverting this overdetermined system of linear equations to obtain a least squares best-fit solution, assuming the applied gradient is uniform. Clark (2008) provides a matrix-based algorithm for this procedure. A value of φ = 63° was chosen as a mathematically optimal value that is also convenient for fabrication. The inclinations of the sloping face normals $\hat{\mathbf{n}}_k$ are φ' = 90° – φ = 27° and their azimuths with respect to the instrument axes are nominally ψ_1 = 135°, ψ_2 = 75°, ψ_3 = 15°, ψ_4 = 315°, ψ_5 = 255°, ψ_6 = 195°. The direction cosines of $\hat{\mathbf{n}}_k$ with respect to XYZ are (l_k, m_k, n_k) = (cosψ_k cosφ', sinψ_k cosφ', sinφ') = (cosψ_k sinφ, sinψ_k sinφ, cosφ).

6.8 Calibration and referencing corrections of sensor outputs

6.8.1 FIELD CALIBRATION AND IMBALANCE CORRECTIONS

In practice individual sensors depart from ideal behaviour and the array geometry is imperfect. In particular, SQUID devices generally have unknown offsets and intrinsic gradiometers invariably have some common mode response. Offsets can be ignored for calibration purposes, provided AC or switched calibration fields are used. Calibration in alternating fields in fact also allows the offsets to be determined directly at the time of calibration.

Consider initially a uniform applied field **F** = (X, Y, Z). The uncalibrated responses of the magnetometers and gradiometers to this field are respectively

$$V_k^M = \alpha_k F_{x'_k} + m_k = \alpha_k \mathbf{F}.\hat{\mathbf{n}}_k + \mu_k,$$
$$V_k^G = \beta_k F_{x'_k} + g_k = \beta_k \mathbf{F}.\hat{\mathbf{n}}_k + g_k, \quad (9)$$

where the α_k are calibration constants for the magnetometers, the β_k define the common mode response of the gradiometers and the μ_k, g_k are (usually unknown) offsets.

If the applied uniform field is sinusoidal, **F** = $\mathbf{F}_0\cos\omega t$, then the output voltages are

$$V_k^M = \alpha_k(\mathbf{F}_0.\hat{\mathbf{n}}_k)\cos\omega t + \mu_k = \alpha_k(X_0 l_k + Y_0 m_k + Z_0 n_k)\cos\omega t + \mu_k,$$
$$V_k^G = \beta_k(\mathbf{F}_0.\hat{\mathbf{n}}_k)\cos\omega t + g_k = \beta_k(X_0 l_k + Y_0 m_k + Z_0 n_k)\cos\omega t + g_k. \quad (10)$$

If the tensor gradiometer is carefully aligned with respect to the Rubens coil, the absolute values of the components (X_0, Y_0, Z_0) of the applied field vector amplitude $\mathbf{F}_0$ can be calculated from the coil geometry. Any slight initial misalignment can be corrected by adjusting the instrument orientation until an applied field along one coil axis, say Z, produces negligible signal in the X and Y field sensors that lie in the orthogonal plane. The instrument

can then be rotated about the vertical axis until a field applied along the X axis produces negligible response in the Y sensor. The direction cosines (with respect to the applied field) of the sensitive axes of the devices on the sloping faces are known from the array geometry.

If the main referencing magnetometer is already well calibrated, however, the values of (X_0, Y_0, Z_0) are measured directly as the amplitudes of the sinusoidal outputs, obviating the need to accurately align the instrument in the Rubens coil set. Offsets in the referencing magnetometer outputs do not affect determination of the absolute applied field components.

A simple calibration of the face-mounted devices can be effected by placing the gradiometer array upright in the centre of the Rubens coil set and applying a sinusoidal vertical field, with all DC field components maintained at low values. Then the device responses are sinusoidal signals with amplitudes A_0, B_0 such that

$$V_k^M = \alpha_k Z_0 n_k \cos\omega t + \mu_k = A_0 \cos\omega t + \mu_k,$$
$$V_k^G = \beta_k Z_0 n_k \cos\omega t + g_k = B_0 \cos\omega t + g_k. \tag{11}$$

The calibration constants are therefore given by

$$\alpha_k = \frac{A_0}{Z_0 n_k}, \beta_k = \frac{B_0}{Z_0 n_k}, \tag{12}$$

and the offsets are the outputs averaged over an integral number of cycles.

A more comprehensive calibration that incorporates deviations from ideal geometry can be effected by applying uniform alternating fields along three different, nominally orthogonal, directions. The field components can be applied successively or, alternatively, simultaneously applied along all three axes with different frequencies for each axis.

In the general case the three different applied fields need not be along the instrument axes, or even be strictly orthogonal. If uniform alternating fields with component amplitudes (X_1, Y_1, Z_1), (X_2, Y_2, Z_2) and (X_3, Y_3, Z_3), as measured by the instrument referencing magnetometer, are applied to the tensor gradiometer, the in-phase outputs from devices on the kth face are

$$\begin{bmatrix} V_k^M(X_1,Y_1,Z_1) \\ V_k^M(X_2,Y_2,Z_3) \\ V_k^M(X_3,Y_3,Z_3) \end{bmatrix} = \alpha_k \begin{bmatrix} X_1 & Y_1 & Z_1 \\ X_2 & Y_2 & Z_2 \\ X_3 & Y_3 & Z_3 \end{bmatrix} \begin{bmatrix} l_k \\ m_k \\ n_k \end{bmatrix} = \alpha_k \begin{bmatrix} X_1 & Y_1 & Z_1 \\ X_2 & Y_2 & Z_2 \\ X_3 & Y_3 & Z_3 \end{bmatrix} \hat{\mathbf{n}}_k,$$

$$\begin{bmatrix} V_k^G(X_1,Y_1,Z_1) \\ V_k^G(X_2,Y_2,Z_3) \\ V_k^G(X_3,Y_3,Z_3) \end{bmatrix}_{\mathbf{G}=\mathbf{0}} = \beta_k \begin{bmatrix} X_1 & Y_1 & Z_1 \\ X_2 & Y_2 & Z_2 \\ X_3 & Y_3 & Z_3 \end{bmatrix} \begin{bmatrix} l_k \\ m_k \\ n_k \end{bmatrix} = \beta_k \begin{bmatrix} X_1 & Y_1 & Z_1 \\ X_2 & Y_2 & Z_2 \\ X_3 & Y_3 & Z_3 \end{bmatrix} \hat{\mathbf{n}}_k. \tag{13}$$

Inverting the matrices on the RHS gives empirical estimates of the orientations of the sensitive axes of the devices on each face, as well as the calibration constants:

$$\alpha_k \hat{\mathbf{n}}_k = \begin{bmatrix} \alpha_k l_k \\ \alpha_k m_k \\ \alpha_k n_k \end{bmatrix} = \begin{bmatrix} X_1 & Y_1 & Z_1 \\ X_2 & Y_2 & Z_2 \\ X_3 & Y_3 & Z_3 \end{bmatrix}^{-1} \begin{bmatrix} V_k^M(X_1,Y_1,Z_1) \\ V_k^M(X_2,Y_2,Z_3) \\ V_k^M(X_3,Y_3,Z_3) \end{bmatrix},$$

$$\beta_k \hat{\mathbf{n}}_k = \begin{bmatrix} \beta_k l_k \\ \beta_k m_k \\ \beta_k n_k \end{bmatrix} = \begin{bmatrix} X_1 & Y_1 & Z_1 \\ X_2 & Y_2 & Z_2 \\ X_3 & Y_3 & Z_3 \end{bmatrix}^{-1} \begin{bmatrix} V_k^G(X_1,Y_1,Z_1) \\ V_k^G(X_2,Y_2,Z_3) \\ V_k^G(X_3,Y_3,Z_3) \end{bmatrix},$$

$$\alpha_k = -\mathrm{sgn}(\alpha_k n_k)\sqrt{(\alpha_k l_k)^2 + (\alpha_k m_k)^2 + (\alpha_k n_k)^2}, \tag{14}$$

$$\beta_k = -\mathrm{sgn}(\beta_k n_k)\sqrt{(\beta_k l_k)^2 + (\beta_k m_k)^2 + (\beta_k n_k)^2}, \tag{15}$$

$$\hat{\mathbf{n}}_k = \frac{1}{\alpha_k} \begin{bmatrix} X_1 & Y_1 & Z_1 \\ X_2 & Y_2 & Z_2 \\ X_3 & Y_3 & Z_3 \end{bmatrix}^{-1} \begin{bmatrix} V_k^M(X_1,Y_1,Z_1) \\ V_k^M(X_2,Y_2,Z_3) \\ V_k^M(X_3,Y_3,Z_3) \end{bmatrix} = \frac{1}{\beta_k} \begin{bmatrix} X_1 & Y_1 & Z_1 \\ X_2 & Y_2 & Z_2 \\ X_3 & Y_3 & Z_3 \end{bmatrix}^{-1} \begin{bmatrix} V_k^G(X_1,Y_1,Z_1) \\ V_k^G(X_2,Y_2,Z_3) \\ V_k^G(X_3,Y_3,Z_3) \end{bmatrix}. \tag{16}$$

where the sign ambiguity in the calibration constants has been resolved by noting that the *Z* components of the $\hat{\mathbf{n}}_k$ are negative.

This procedure calibrates changes in outputs of face-mounted magnetometers in terms of magnetic field changes and determines the offsets at the time of calibration as the time-averaged magnetometer outputs. It also determines the corrections that need to be applied to correct the gradiometer outputs for common mode contributions due to imperfect balance. A first order imbalance correction, based on the outputs (*X*, *Y*, *Z*) of the triaxial referencing magnetometer, is given by

$$V_k'^G = V_k^G - \beta_k(Xl_k + Ym_k + Zn_k), \tag{17}$$

where $V_k'^G$ is the imbalance-corrected gradiometer output.

Offsets in the referencing magnetometer outputs feed in to the gradiometer offset. *Changes* in the gradiometer output, due to changing applied fields and gradients, are not affected by a constant offset.

In the presence of strong gradients, the field at each gradiometer can differ somewhat from the field measured at the instrument referencing magnetometer. It is therefore probably more accurate to perform the balancing corrections using the face-mounted magnetometers, using the formula

$$V_k'^G = V_k^G - \gamma_k V_k^M, \tag{18}$$

where the constants γ_k can be obtained directly from the ratios of gradiometer to magnetometer signal amplitudes during calibration carried out in uniform alternating fields:

$$\gamma_k = \frac{\beta_k}{\alpha_k} = \frac{B_0}{A_0}. \tag{19}$$

6.8.2 GRADIENT CALIBRATION AND OFFSET CORRECTIONS

Gradiometer calibration can be carried out using the Rubens coil set to apply uniform alternating gradients to the instrument. If the alternating applied gradient, $\mathbf{G} = \mathbf{G}_0 \cos\omega t$, is produced by vertical field coils activated in series opposition, then by symmetry and the tracelessness condition

$$\mathbf{G} = \mathbf{G}_0 \cos\omega t = \begin{bmatrix} -B_{ZZ}/2 & 0 & 0 \\ 0 & -B_{ZZ}/2 & 0 \\ 0 & 0 & B_{ZZ} \end{bmatrix} \cos\omega t. \tag{20}$$

The amplitude of the *balance-corrected* gradiometer outputs is then

$$V_k'^G = -\frac{3}{2} C_k B_{ZZ} \sin\varphi \cos\varphi = -\frac{3}{2} C_k B_{ZZ} n_k \sqrt{1-n_k^2}, \tag{21}$$

where C_k is a gradient calibration constant that converts the off-diagonal component to which the planar gradiometer is sensitive (i.e. $B_{x_k' z_k'}$) to voltage. It is desirable to use balance-corrected outputs for the gradient calibration, even if the applied field is kept very low, because the presence of a first order gradient across the finite size array produces nonzero fields at the gradiometer locations. Since the magnitude of the applied gradient is known from calculation or measurement, C_k can be calculated simply from the above equation. The common mode rejection ratio (CMRR) can be estimated as

$$\mathrm{CMRR} = \frac{\beta_k b}{C_k}, \tag{22}$$

where b is the baseline of the gradiometer.

6.8.3 EFFECT OF GRADIOMETER OFFSETS ON GRADIENT TENSOR DETERMINATION

The six calibrated gradiometer outputs are each linear combinations of elements of the gradient tensor in the instrument frame. If the outputs are free of offsets, then

$$\mathbf{G}' = \begin{bmatrix} B_{x_1' z_1'} \\ B_{x_2' z_2'} \\ B_{x_3' z_3'} \\ B_{x_4' z_4'} \\ B_{x_5' z_5'} \\ B_{x_6' z_6'} \end{bmatrix} = \mathbf{MG} = \mathbf{M} \begin{bmatrix} B_{xx} \\ B_{xy} \\ B_{xz} \\ B_{yy} \\ B_{yz} \end{bmatrix}, \tag{23}$$

which has solution

$$\mathbf{G} = \begin{bmatrix} B_{xx} \\ B_{xy} \\ B_{xz} \\ B_{yy} \\ B_{yz} \end{bmatrix} = \left(\mathbf{M}^{\mathrm{T}}\mathbf{M}\right)^{-1}\mathbf{M}^{\mathrm{T}} \begin{bmatrix} B_{x_1'z_1'} \\ B_{x_2'z_2'} \\ B_{x_3'z_3'} \\ B_{x_4'z_4'} \\ B_{x_5'z_5'} \\ B_{x_6'z_6'} \end{bmatrix} = \mathbf{M}^{*} \begin{bmatrix} B_{x_1'z_1'} \\ B_{x_2'z_2'} \\ B_{x_3'z_3'} \\ B_{x_4'z_4'} \\ B_{x_5'z_5'} \\ B_{x_6'z_6'} \end{bmatrix} = \mathbf{M}^{*}\mathbf{G}', \tag{24}$$

where $\mathbf{M}^*$ denotes the pseudoinverse of the 6×5 matrix **M** (Clark, 2008).

In practice the gradiometer outputs will have unknown offsets o_k that are constant or vary slowly, unless the SQUIDs lose lock or are reset. The calculated gradient tensor elements $\mathbf{G}''$ will also have essentially constant offsets, since

$$\mathbf{G}'' = \mathbf{M}^{*}\left(\mathbf{G}' + \mathbf{o}\right) = \mathbf{M}^{*}\mathbf{G}' + \mathbf{M}^{*}\mathbf{o} = \mathbf{G} + \mathbf{C}, \tag{25}$$

where **G** comprises the offset-free gradient tensor elements, **o** is the vector of planar gradiometer offsets and $\mathbf{C} = \mathbf{M}^{*}\mathbf{o}$ is a constant vector of offsets in the calculated gradient tensor elements.

The offsets of the gradient tensor elements can in principle be determined in several ways:

(i) applying an alternating gradient and averaging outputs over an integral number of cycles

(ii) placing the instrument in a zone that is known to be gradient free

(iii) rotating the instrument into several different orientations within a uniform gradient, in order to separate outputs that transform as a second order tensor from outputs that are independent of orientation.

In practice the presence of unknown offsets in the measured gradient tensor is not a serious issue, because applications require only determination of gradient *anomalies*. Interpretation of data entails subtraction of a baseline, which may represent a regional gradient or instrument offsets, from the measured values. The Werner-Clark deconvolution algorithm solves for a constant or slowly varying base level, so any offsets in measured gradient gradient tensor elements are automatically removed from the data.

6.8.4 EFFECT OF FINITE SIZE OF GRADIOMETER ARRAY

So far we have assumed that the field measured by the referencing magnetometers represents the field to which the gradiometer sensors are exposed. This is only strictly true when there is no field gradient. A refinement of the calibration and referencing corrections can take the finite separation of the magnetometers and gradiometers into account. The effective baseline of each planar gradiometer is about 2 cm. The planar gradiometers measure first order gradients at six distinct locations separated by up to ~10 cm.

Table 1 summarises the effects of these finite baselines on measured gradients. Typical magnitudes of the anomalous field, first order gradient and second order gradient are given, for various source-sensor separations, assuming a dipole source of moment 1 Am². However, the relative errors in the measured first order gradients are independent of the source moment. The relatively large errors across a 10 cm baseline, particularly for nearby sources, demonstrate that referencing corrections are preferably based on the face-mounted magnetometers, which are much closer to the planar gradiometers than the centrally mounted triaxial instrument reference magnetometer.

The modelling used to produce Table 1 also shows that gradients of higher than second order make negligible contribution to the measured magnetic gradient tensor in all cases of practical interest. Thus a theoretical treatment of the effects of finite baselines needs to use a Taylor series expansion of the magnetic field only up to the second order.

Table 6. Effects of finite size of planar gradiometers and of gradiometer array (source moment 1 Am²)

Range (m)	Field (nT)	1st order gradient (nT/m)	2nd order gradient (nT/m²)	% error in Bxz across 2 cm baseline	% error in Bij across 10 cm baseline
2	125	187.5	375	4	20
5	8	4.8	3.84	1.6	8
10	1	0.3	0.12	0.8	4
20	0.125	0.019	0.0038	0.4	2

The magnetic field **B** and first order gradient **G** at point **r** throughout the gradiometer array can be expressed as a Taylor series expansion about a suitably chosen reference point $\mathbf{r}_0$, such as the centroid of the planar gradiometer positions:

$$\begin{aligned}\mathbf{B}(\mathbf{r}) &= \mathbf{B}(\mathbf{r}_0) + (\mathbf{r}-\mathbf{r}_0).\nabla\mathbf{B} + \frac{1}{2}(\mathbf{r}-\mathbf{r}_0).\nabla\nabla\mathbf{B}.(\mathbf{r}-\mathbf{r}_0) + \ldots \\ &= \mathbf{B}(\mathbf{r}_0) + (\mathbf{r}-\mathbf{r}_0).\mathbf{G}(\mathbf{r}_0) + \frac{1}{2}(\mathbf{r}-\mathbf{r}_0).(\nabla\mathbf{G})_{\mathbf{r}_0}.(\mathbf{r}-\mathbf{r}_0) + \ldots\end{aligned} \tag{26}$$

$$\mathbf{G}(\mathbf{r}) = \mathbf{G}(\mathbf{r}_0) + (\mathbf{r}-\mathbf{r}_0).(\nabla\mathbf{G})_{\mathbf{r}_0} + \ldots \tag{27}$$

Using (9) and (26), the required modification of the referencing correction (18) is

$$V_k'^G = V_k^G - \gamma_k V_k^M - \beta_k B_{x_k' y_k} \Delta y_k, \tag{28}$$

where Δy_k is the displacement along the y_k axis of the face-mounted SQUID magnetometer from the planar gradiometer. Using (3) and (4) the gradient tensor element required to use (28) is given by

$$\begin{aligned}B_{x_k' y_k} = &\frac{(B_{YY} - B_{XX})\cos\varphi\sin(2\psi_k)}{2} + (1+\sin^2\psi_k)\sin(2\varphi) + B_{XY}\cos\varphi\cos(2\psi_k) \\ &+ \sin\varphi\sin\psi_k B_{XZ} - \sin\varphi\cos\psi_k B_{YZ}.\end{aligned} \tag{29}$$

The initially estimated gradient tensor elements with respect to the instrument co-ordinate system can be plugged into (29) and the correction (28) performed for each gradiometer output. The recalculated gradient tensor can then be used in (29) and the referencing correction carried out iteratively.

Because second order gradients are not measured directly by this system, the effects of the finite size of the array on determination of the first order gradient tensor cannot be corrected without extra information. However, second order corrections are only important close to

magnetic sources. In the case of practical interest, namely the search for compact magnetic objects, the initially estimated gradient tensor provides a solution for the location and dipole moment of the source. The Werner-Clark deconvolution algorithm ameliorates the effects of second order perturbations by removing smoothly varying background that does not fit a dipole signature. The second order gradients can be calculated analytically from the initially estimated dipole solution. These estimates can then be used in eqn (27) to correct the measured gradient tensor for the finite baseline, producing an improved estimate of the dipole source parameters. If necessary, the procedure can be iterated until there are no further improvements in the estimated first order gradients.

6.9 Lab Calibration - Static testing of the HTSTG in laboratory conditions

Multiple measurements of the system's response to known magnetic fields and gradients using a Rubens cage setup (shown in Figure 53(a)) has made it possible to calibrate the instrument and determine the magnetometer compensation correction terms. Applying known magnetic gradient ac fields to the system at different frequencies and magnitudes allows us to determine the gradient calibration transfer coefficients (which transforms voltage noise or flux noise to magnetic field gradient, V $Hz^{-1/2}$ / Φ_0 $Hz^{-1/2}$ to T m^{-1} $Hz^{-1/2}$). By applying these coefficients to the shielded noise, we can determine the intrinsic gradient sensitivity for each gradiometer. Intrinsic noise measurements are carried out inside layers of mu-metal shielding which represents a low magnetic field environment (picture shown in Figure 53(b)).

Figure 53. (a) The 2.5 m outer diameter, tri-axial Ruben's coil set in the Lindfield CSIRO laboratory and (b) mu-metal shielding used to measure the intrinsic noise of the devices.

The latest calibration and noise measurement has indicated the noise to be sub 2.28 pT m^{-1} $Hz^{-1/2}$ at 10 Hz, for all six devices which is plotted in Figure 54. The measured sensitivity of the six gradiometers ranged between 1.25 – 2.28 pT m^{-1} $Hz^{-1/2}$ at 10 Hz. The actual noise level at 10 Hz is somewhat skewed due to the presence of a broad peak in the noise spectra between ~15-30 Hz. This is due to a large rotating magnetic in the next room. Measured unshielded, in the noisy laboratory environment, the gradient noise increased to ~4.30-5.46 pT m^{-1} $Hz^{-1/2}$ at 10 Hz, which is shown in Figure 55 for all six gradiometers.

Applying known uniform ac magnetic fields at different frequencies and magnitudes along three different, nominally orthogonal directions we can determine the common mode response or balance of the devices.

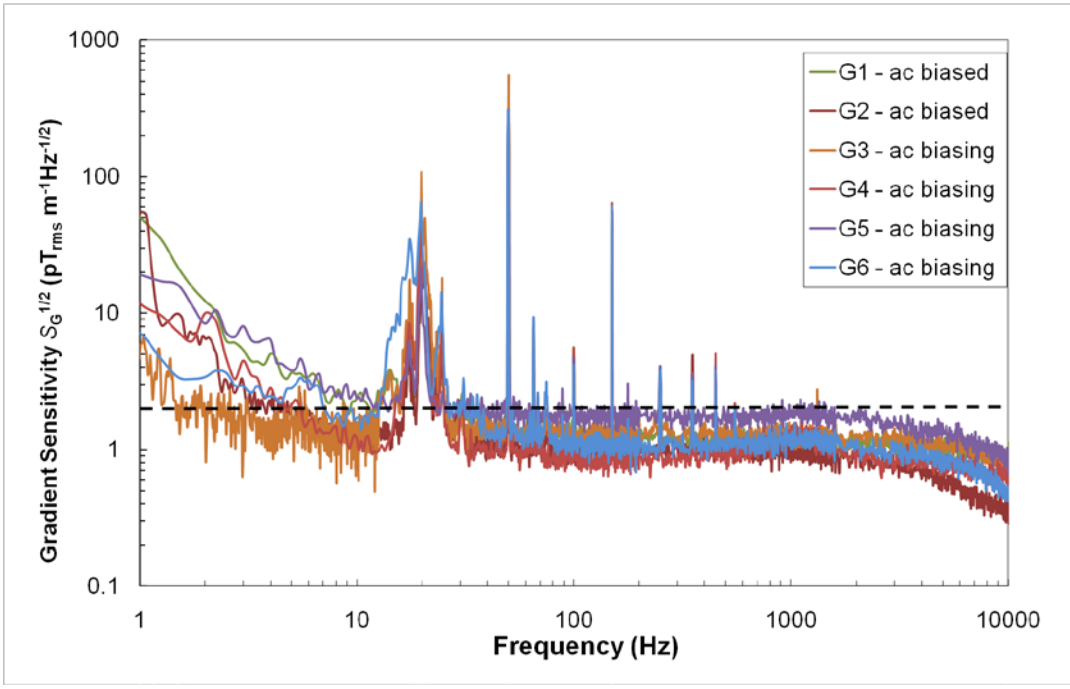

Figure 54. Gradient noise plot of all six gradiometers, used in the Magnetic Tensor Gradiometer, measured while magnetically shielded in the laboratory. The plots show that all six sensors have a noise performance either better than or close to the specified 2 pT/m / √Hz at 10 Hz. The magnetic shielding did not completely eliminate all background magnetic interference as is seen by the signals at ~ 15 Hz, 50 Hz (and higher order harmonics).

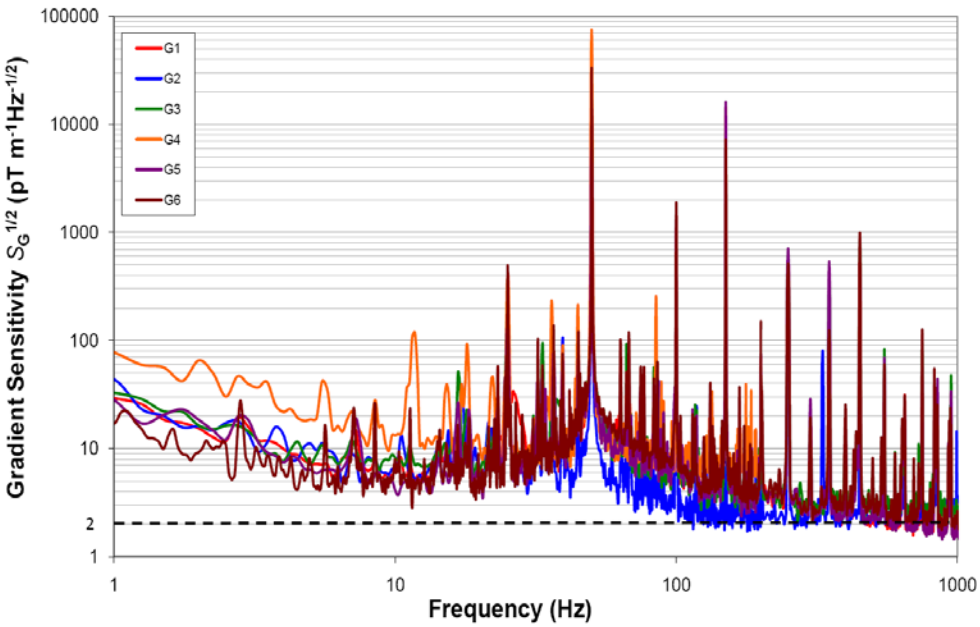

Figure 55. Gradient noise plot of all six gradiometers, used in the Magnetic Tensor Gradiometer, measured while unshielded in the noisy laboratory environment.

Table 7. A summary of the results obtained for each gradiometer device (designated G1-G6). The table gives the gradient sensitivity achieved at two different stages of the project for shielded and unshielded environments. Note for the December 2010 measures the unshielded measurements were performed using non-optimum dc biasing only.

	Gradiometer Sensitivity $S_G^{1/2}$ ($pT_{rms}m^{-1}Hz^{-1/2}$)						
	December 2010		**November 2011**				
	$S_G^{1/2}$ **@ 10 Hz** Shielded Lab ac biased	$S_G^{1/2}$ **@ 10 Hz** Unshielded Lab dc biased	$S_G^{1/2}$ **@ 10 Hz** Shielded Lab ac biased	% difference from specified 2 $pTm^{-1}Hz^{-1/2}$	$S_G^{1/2}$ **@ 10 Hz** Unshielded Lab ac biased	$S_G^{1/2}$ **@ 10 Hz** Unshielded (West Head) ac biased	$S_G^{1/2}$ **@ 30 Hz** Shielded Lab ac biased
G1	2.19*	55*	1.55 (-29%[1])	-22.5 %	4.57	2.62 (+31%[2])	1.23(-38%[2])
G2	3.30	45	2.13 (-35%[1])	+6.5 %	4.67	2.50 (+25%[2])	1.13(-43%[3])
G3	2.07	48	1.80 (-13%[1])	-10.0 %	5.46	1.85 (-19%[2])	1.42(-29%[3])
G4	2.77*	51*	1.25 (-55%[1])	-37.5 %	4.30	1.51 (-24%[2])	1.04(-48%[3])
G5	2.26	44	2.28 (+1%[1])	+14.0 %	5.05	2.72 (+36%[2])	1.89(-5%[3])
G6	1.95	42	1.68 (-14%[1])	-16.0 %	4.62	1.72 (-28 %[2])	1.36(-32%[3])

*** values are inferred from average antenna gain factor (see table 4). [1] Percentage difference between sensitivity determined individually (using indirect method) and sensitivity determined as a system (direct method). [2] Percentage difference between the specified required sensitivity and that measured unshielded at West Head. [3] Percentage difference between the specified required sensitivity and that measured shielded in the lab at 30 Hz.**

Table 6 summarises each gradiometer performance in various environments at 10 Hz (30 Hz shielded noise figures are shown to demonstrate the white noise of the devices showing that all devices have sub 2 pT/m/√Hz at 30 Hz). Gradient sensitivity measurements shown in Decemeber 2010 column were determined individually using the method described in Section 5.4.4. By November 2011 our ability to fully optimise the device unshielded using ac biasing had been achieved and with the full system assembled calibration was completed by applying uniform gradient fields to the system. The table also includes measurements taken unshielded at a remote low noise location (West Head). Figure 56 illustrates the gain achieved by coupling the gradiometric antenna to the readout gradiometer where shown is gradient noise for the readout gradiometer (G5) both with and without the antenna, inside mu-metal shielding and unshielded (using ac biasing). In Table 7 is a list of gradient sensitivity before and after the gradiometric antenna was coupled with the gain factor included. The gradient noise figures are quoted for 1 kHz measurements unless otherwise indicated. Figure 56 shows the noise spectra for gradiometer G5 with and without the antenna, inside mu-metal shielding and unshielded (using ac biasing).

Table 8. The achieved increase in gradient sensitivity using the gradiometric antenna.

	Read-out Gradiometer (A_{EFF} ~ 0.122/0.164 mm^2) (Baseline *l* = 0.37 cm)	**Gradiometric Antenna** (A_{EFF} ~ 0.64 mm^2) (Baseline *l* = 2.25 cm)		
	Gradient sensitivity $S_G^{1/2}$ @1 kHz ($pTm^{-1}Hz^{-1/2}$)	Gain factor	$S_G^{1/2}$ @ 1 kHz ($pT_{rms}m^{-1}Hz^{-1/2}$) Shielded	$S_G^{1/2}$ @ 10 Hz ($pT_{rms}m^{-1}Hz^{-1/2}$) Shielded
G1	54	29.4	1.13	2.13
G2	49	28.7	1.23	1.55
G3	61	30.9	1.42	1.80
G4	44	30.2	1.04	1.25
G5	85	32.4	1.89	2.28
G6	63	33.5	1.36	1.68

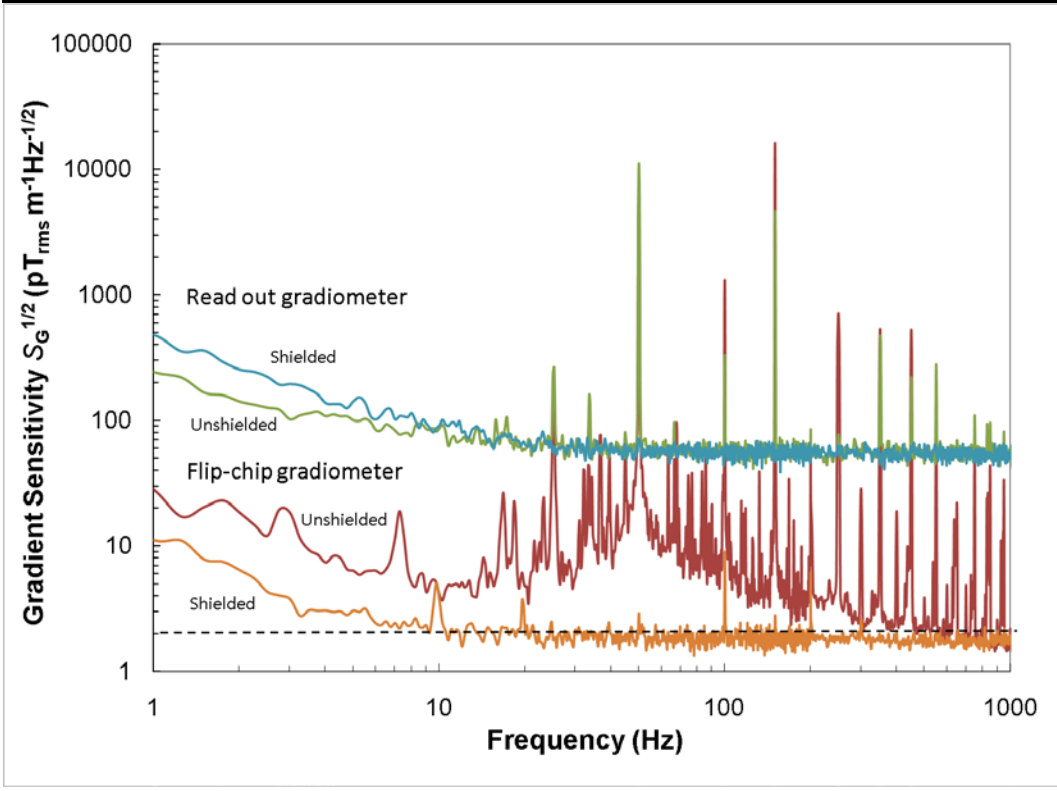

Figure 56. The measured gradient sensitivity of a flip-chip gradiometer (G5) shown both with and without the antenna, inside mu-metal shielding and unshielded (using ac biasing).

6.10 Dynamic testing of the HTSTG in laboratory conditions

Dynamic testing of the tensor gradiometer involved the introduction of a slow to medium tilt angle in a single plane to simulate the movement expected in a submerged tow vessel .

Initial tilt-table tests have been successfully run with an individual flip-chip gradiometer and its associated in-plane magnetometer while mounted on the test probe and while mounted on the pyramid. After full assembly of the tensor gradiometer these measurements were repeated for all devices simultaneously in the laboratory. The tensor gradiometer system was mounted on the tilt table at the centre of the Ruben's coil set as seen in Figure 57(b). The initial tilt angle was +/- 11.5º about the instrument's x-axis (E-W), which is defined by the orthogonal SQUID magnetometer M9 located at the base of the pyramid (as seen in Figure 57 (a)) simulating a roll of at a rate of ~ 4 °/s, well beyond the expected motion of a submarine vehicle in tow during a magnetic survey. No fields or gradients were applied for the initial tilt table tests. The gradiometers were measuring the Earth's field plus any additional fields found in the laboratory.

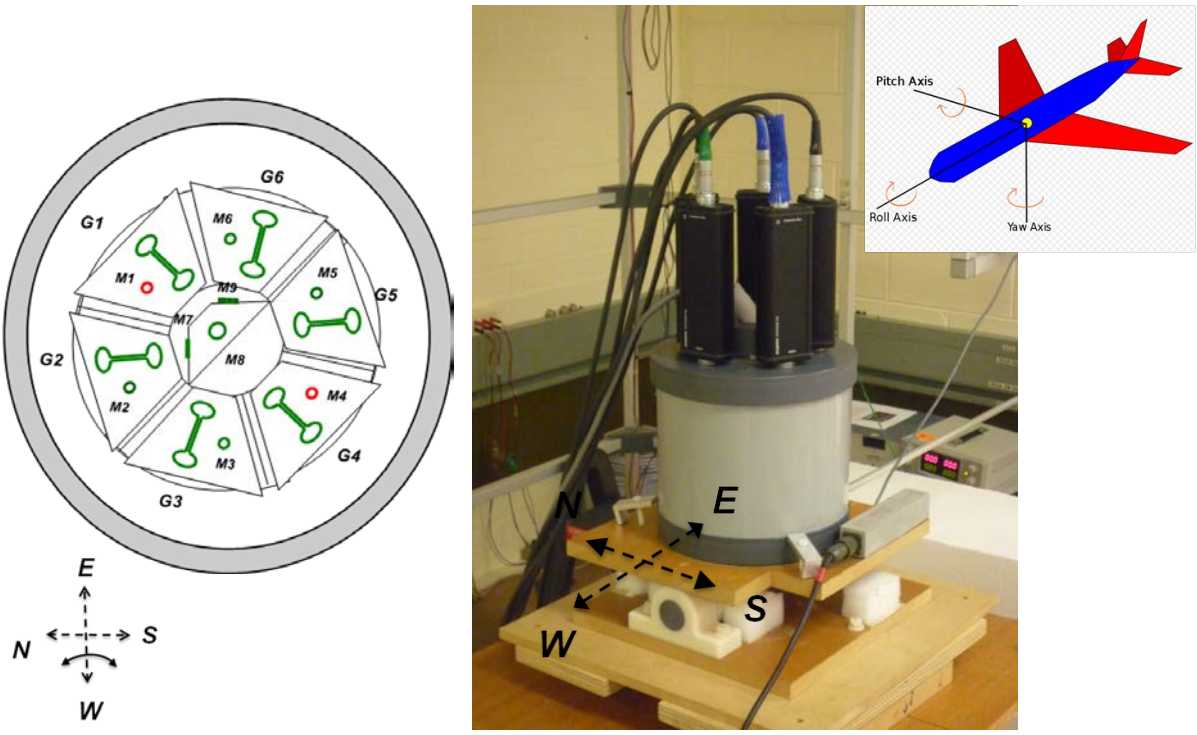

Figure 57. (a) Top view of the system showing the orientation of the sensors (green indicates operating sensors red non-operational) and with respect to the plane of tilting. (b) The tensor gradiometer system mounted on the tilt table at the centre of the Ruben's coil set showing the tilt as a roll on a westerly heading.

These tests have shown that these devices remain stable and in-lock while undergoing motion in the Earth's magnetic field. Tilting the devices through large angles with the plane normal to the Earth's field (representing field changes of max ~ 18 μT), although yielding large dc shifts in the gradiometer output (due to the finite balance), has shown little noise increase after motion has stopped. The measured data is shown in Figure 58. The only processing that has been applied to the data is a moving averaging filter to remove 50 Hz noise. The SQUIDs remained in lock while moving in the Earth's field. In addition, the measurements are repeatable through several cycles of tilting, without drift; the measurements were only recorded over a 20 minute time period.

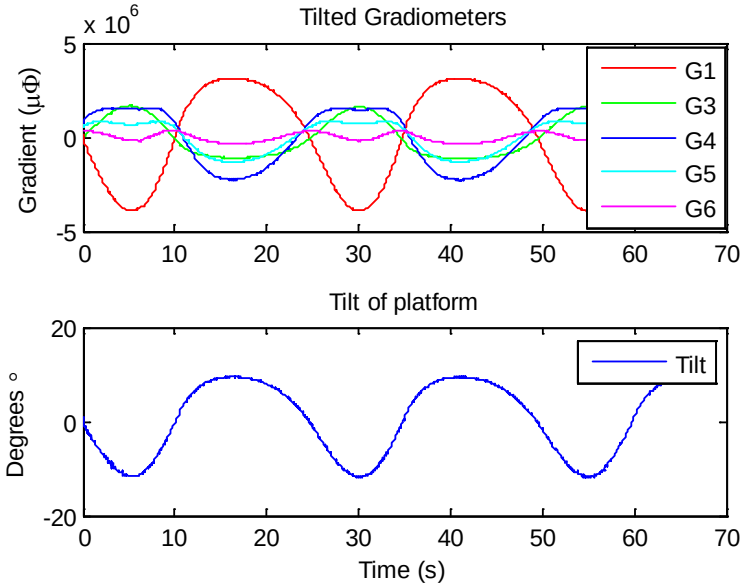

Figure 58. Top plot: the raw output from the gradiometers (note G2 not included) while tilted in the lab. Bottom plot: the tilt angle as a function of time.

The only limiting factor with these large angle measurements was the high sensitivity of the SQUID magnetometers used (see section 6.3) which limited motion to ± 2-5 °. Increasing the angle beyond this meant the magnetometers would reach the limits of their dynamic range and the outputs would clip. For this reason the tilt angle was restricted to ± 2 °. The next step was to determine the effectiveness of the compensation algorithm at removing the unwanted common mode response or motion noise. Figure 59 (a) shows the raw gradiometer output (G4 shown only for clarify) for small angle tilting (± 2 °) in the lab plotted with the estimated common mode response determined from a linear combination of the magnetometers and using the compensation coefficients (determined during calibration).

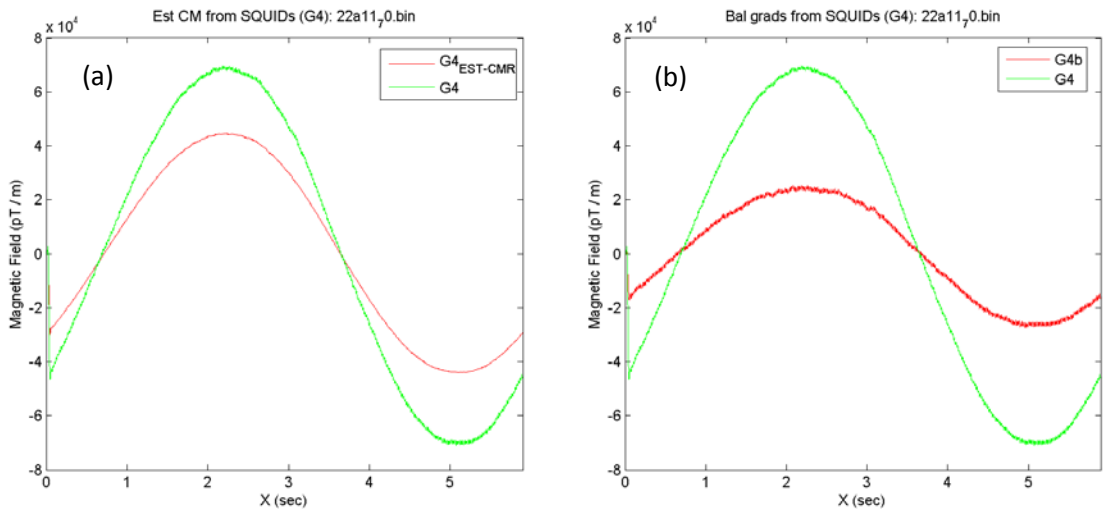

Figure 59. (a) the gradiometer output (G4) (green) and the estimated common mode signal calculated from the balancing routine using the reference SQUID magnetometers (red) and (b) the gradiometer output (green) and the balanced gradiometer signal (red) the system tilting unshielded in the open lab.

The balanced output is plotted in Figure 59 (b) alongside the raw output. The balanced output still contains significant common drift as the system is tilted, however we realise the balancing algorithms are actually working extremely well once we apply a uniform field vertical to the device as it is tilting as plotted in Figure 60. The balanced signal removed up to 95% of the uniform signal therefore indicating that the cause of the drift in the balanced output is largely due to and consistent with large background gradient fields in the laboratory.

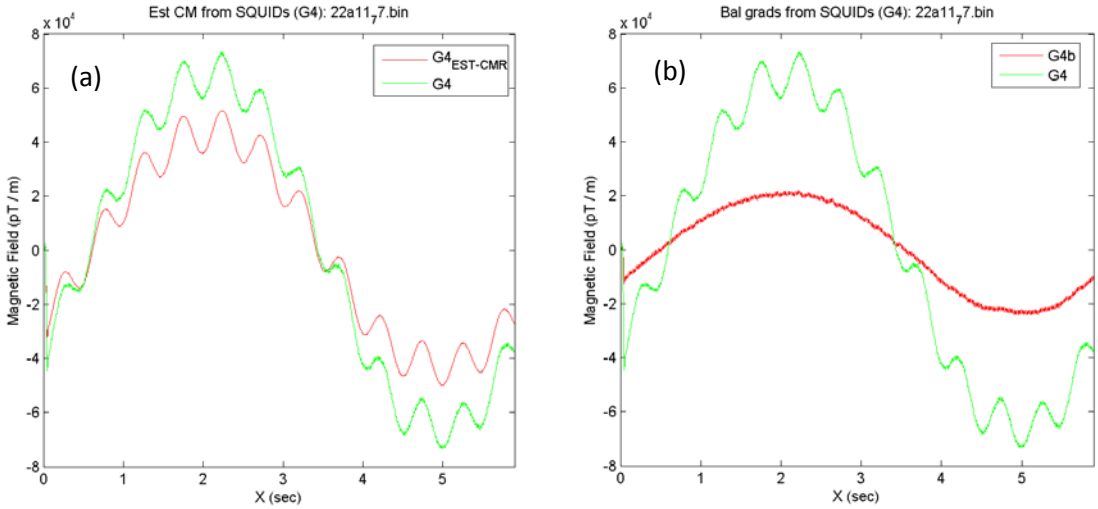

Figure 60. (a) the gradiometer output (G4) (green) and the estimated common mode signal calculated from the balancing routine using the reference SQUID magnetometers (red) and (b) the gradiometer output (green) and the balanced gradiometer signal (red) the system tilting unshielded in the open lab with an applied uniform field at 2 Hz.

Compensation works well in the laboratory as shown in Figure 60 (b). However, large residual gradients in the lab made it necessary to find a magnetically quiet test site to demonstrate the best system performance. Nonmagnetic sandstone underlies the chosen site (West Head). This site has low background gradients.

6.11 Balance – Common Mode Rejection

The capability of a gradiometer to reject unwanted uniform fields is characterized by its common mode rejection or balance b, which can be expressed as $b = A_{PAR}/A_{MAG}$, where A_{PAR} is the device's parasitic effective area to uniform fields and A_{MAG} is the effective area of the gradiometer operating with one pick-up cut (*i.e.* the device operating as a magnetometer). The devices parasitic effective area constitutes a combination of the uniform field response from the SQUID in the centre of the gradiometer having uniform effective area A_{SQ}, asymmetric coupling from the readout gradiometer (one ear coupled better than the other due to non-parallel contact between the substrates), and essentially any uniform field response arising from defects or imperfections in the pick-up loop structure that may occur during fabrication, including bending or bowing of the gradiometric antenna can contribute an effective area A_{DEF}. The effective parasitic are is then $A_{PAR} = A_{SQ} + A_{DEF.}$.

Determining the common mode response or balance of the planar gradiometer involves recording the gradiometers response to known applied ac uniform fields. The common mode response was measured by applying three orthogonal fields B_x, B_y and B_z to the device as

shown in Figure 61. For the individual measurements B_x was minimised and the response to B_y and B_z were measured. The same method of calibration was applied to the fully assembled system but as we are unable to align the device axes with coil axes, the system calibration provides us simply a total device balance shown in the last column of Table 9. The numbers shown in Table 9 represents the ratio of common mode response to field applied, for example G5 has a 1 part in 4103 response to vertical (z-axis) applied fields. Surprisingly the balance to B_z axis fields was quite poor and will require further attention.

Table 9. Lists both the individual balance and the system calibration determined balance.

	Individual Balance $b = (A_{PAR}/A_{EFF})$			System Calibration Balance
	Z-axis	Y-axis	Total	Total
G1	-	-	-	969
G2	582	1527	544	466
G3	277	329	212	152
G4	491	1149	452	321
G5	4103	2409	2077	216
G6	305	2151	302	808

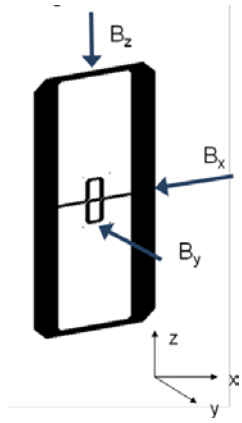

Figure 61. LHS: Rubens coil set used to apply the uniform field to the device and RHS shows a diagram of the fields applied to the device.

7 West head field trial

In order to determine the actual unshielded gradiometer noise performance in a real environment (unshielded in the laboratory represents a magnetically hostile environment) and to demonstrate the best performance of the balancing algorithm it was necessary to find a magnetically quiet test site. The site for the August 2011 trial was located approximately one hour drive from the Lindfield site in the Ku-ring-Gai Chase national park at a place called West Head. This site was chosen for its remote location from human habitation and deep underlying nonmagnetic sandstone deposits giving low magnetic background gradients. The OceanMAG system was setup approximately 200 m off the road down a walking track (Towlers track) shown in the inset Figure 63 (a). The system was securely fixed to the tilt table which was dug in to provide a stable initial horizontal surface. The battery driven dc motor, used to drive the tilt table, was mounted on a tripod located ~1.7 m away and all associated operating equipment was located ~3 m from the sensor as shown in Figure 63 (b). An electrical conduit used for guiding the magnetic puck was setup along the horizontal, x = 2.01 m and z = -0.20 from the sensor with the closest point of approach being midway along the 16 m conduit. The track was orientated ~ 32° E of N and the systems as depicted in Figure 64 which shows a schematic diagram of the magnetic puck run setup used in the West Head trial to simulate a magnetic anomaly passing by the system. The close up top down view of the inside of the Dewar shows the relative positioning of all the sensors with respect to the track with magnetometer M9 orientated parallel.

All thirteen operational SQUIDs (6 gradiometers and 7 magnetometers) were slightly retuned in AC biasing mode and locked. Operation of the devices in this low noise environment was extremely straightforward; the SQUIDs remained completely stable throughout the five hours of operation despite motion in the Earth's field and did not lose lock at any stage. Figure 62 shows the gradient noise spectra for all six gradiometers, measured individually using the spectrum analyser after initial cool down of the system (noise was again measured later with little or no change observed). G2 and G5 show slightly increased noise along with some anomalous noise signals which was attributed to the strong gusts of wind on the day causing some vibrational noise (seen on all devices at various times to varying degrees). The system was subsequently surrounded by tarpaulin to provide some shelter.

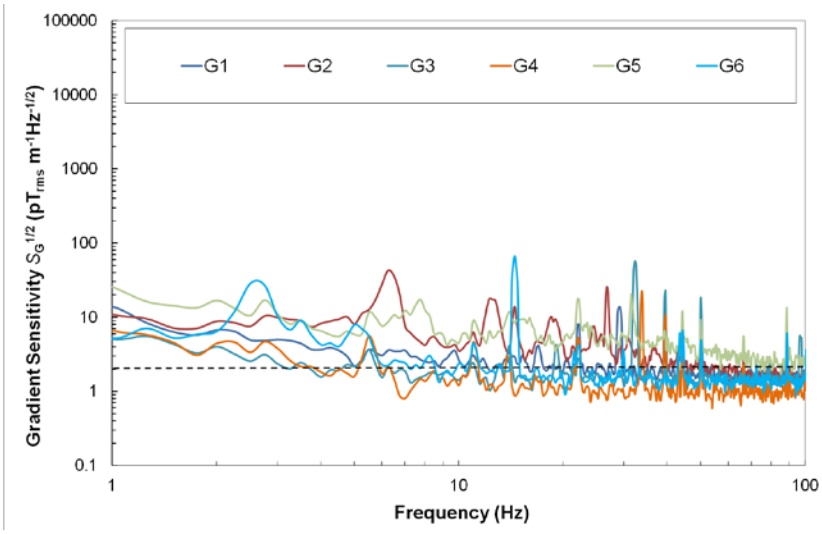

Figure 62. Gradient noise spectra of all six planar gradiometers taken after initial cool down at West Head field trial site.

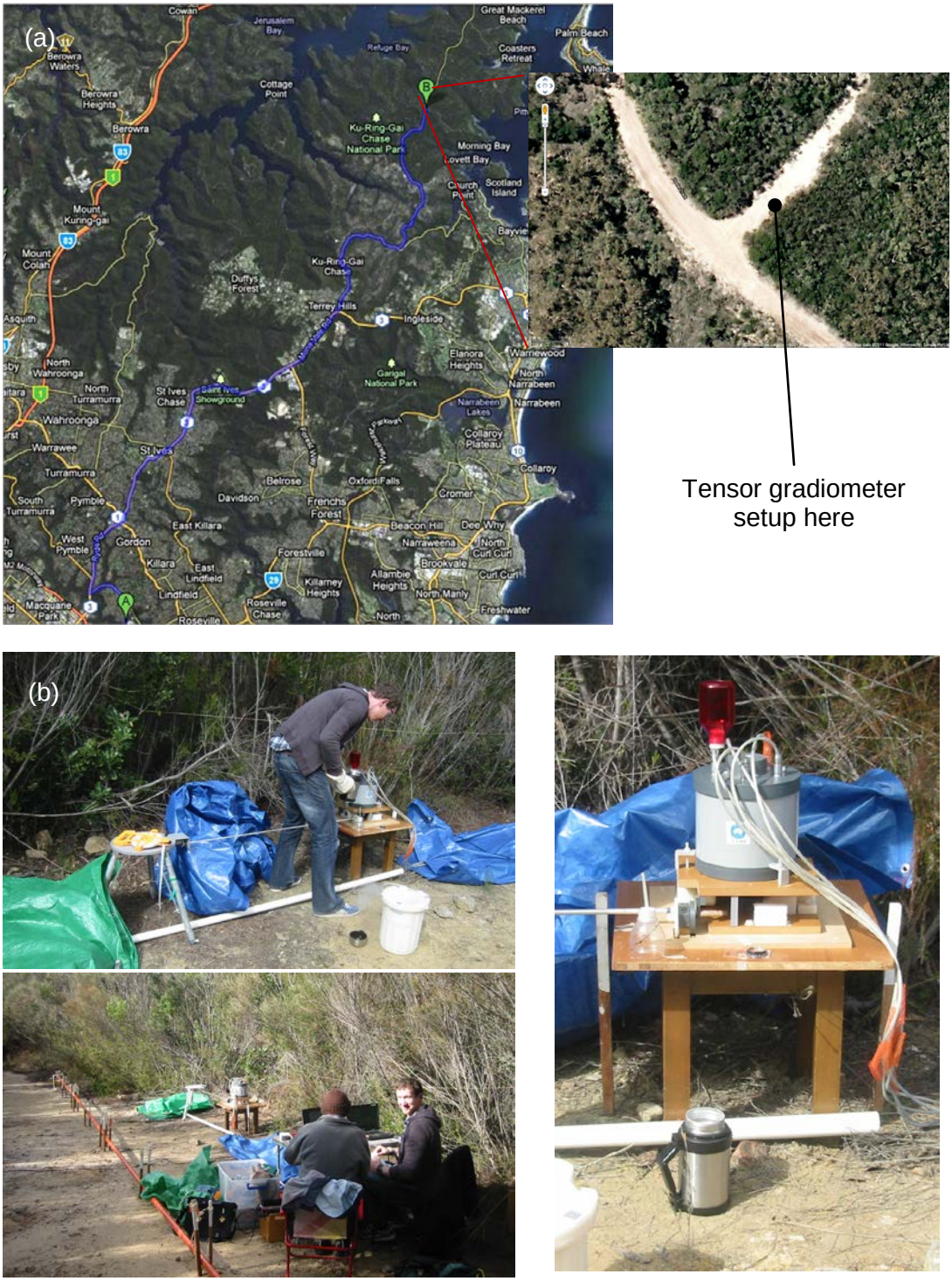

Figure 63. (a) A Google map image showing the route take to the West Head trial site from the Lindfield labs with the inset showing the exact location of the system. (b) shows a number of photos from the trial. Top left: intial cooling of the system using LN_2 showing the system mounted on the tilt table and drive shaft to a dc motor mounted on a tripod. Right shows a close up of the system.

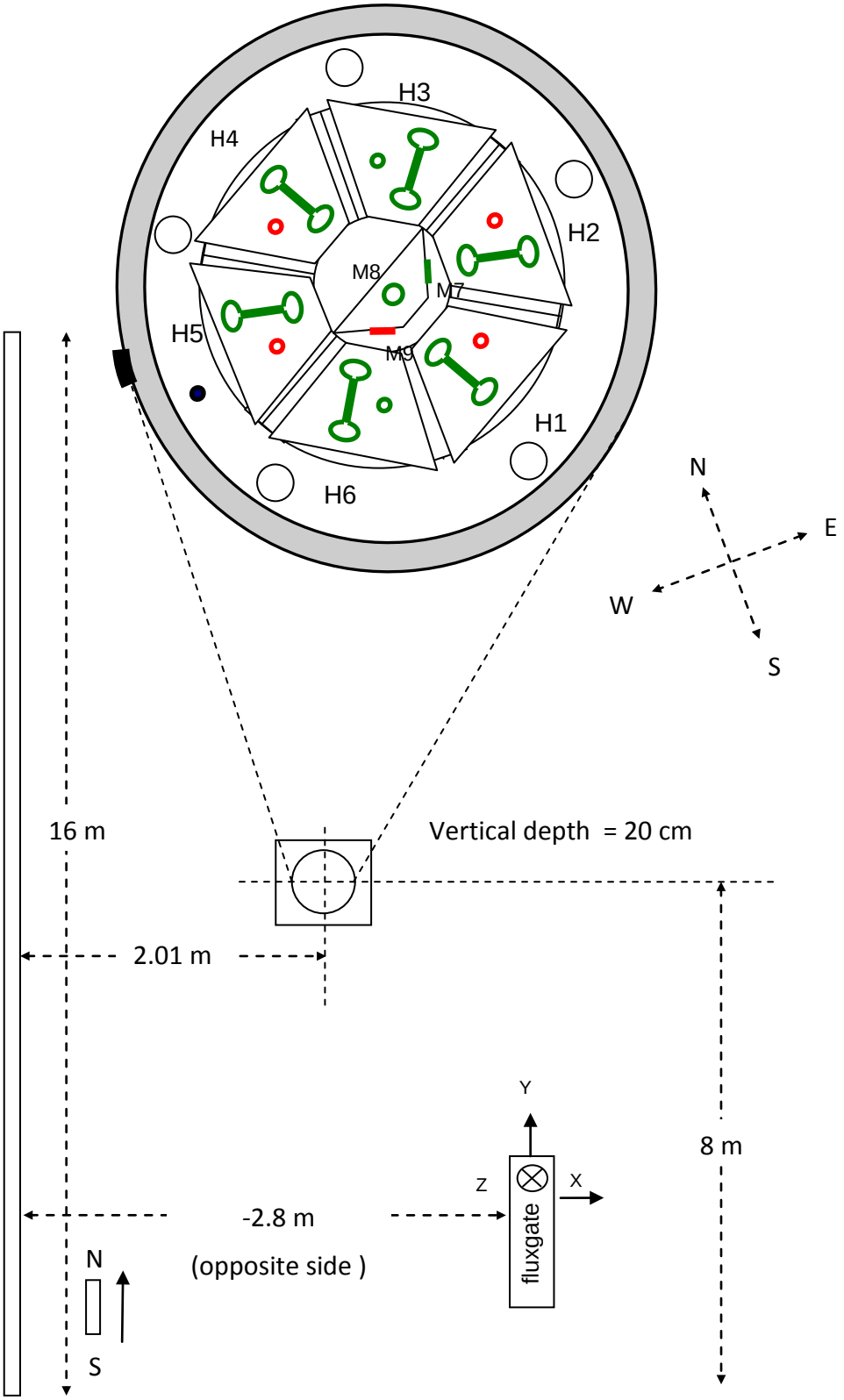

Figure 64. Schematic diagram of the magnetic puck run setpup used in the West Head trial to simulate a magnetic anomaly passing by the system. The close up top down view of the inside of the Dewar shows the relative positioning of all the sensors with respect to the track with magnetometer M9 orientated parallel.

Figure 65 shows a comparison of the gradient noise measured by G1 in three environments; inside three layers of mu-metal shield (in the lab), unshielded in the lab and unshielded at the West Head test site. This clearly shows that we can intrinsically achieve the required sensitivity in an unshielded environment provided the background gradient noise is low. This sensitivity could also be achieved using compensation/balancing routine which will be discussed later.

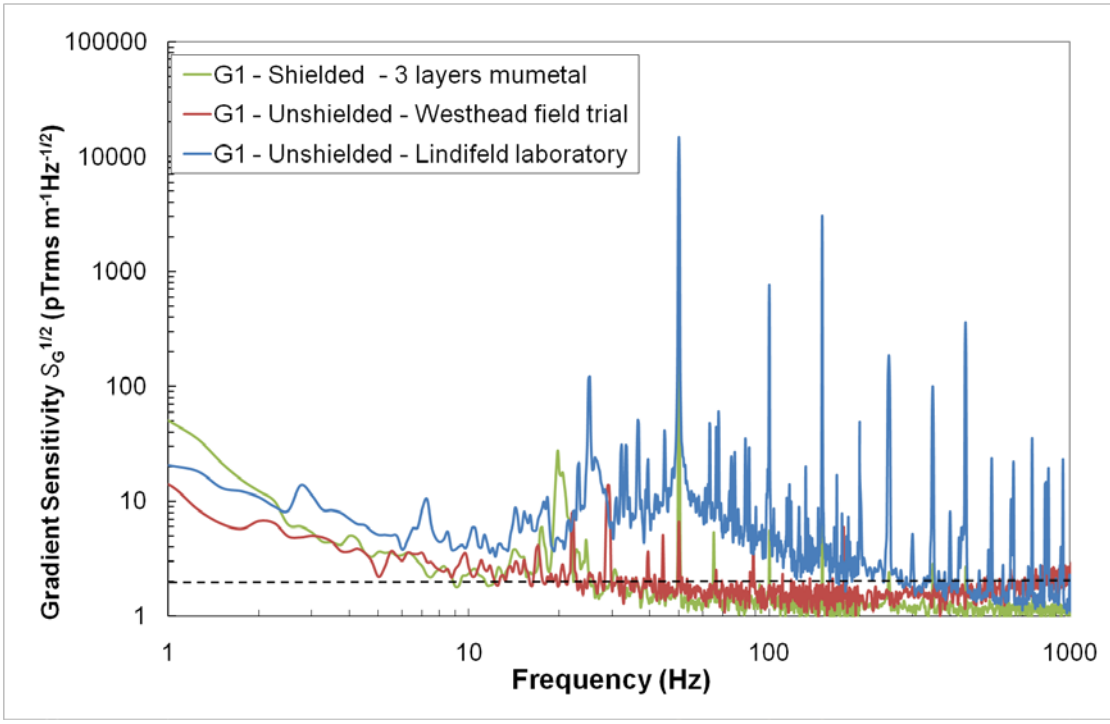

Figure 65. Gradient noise spectra for G1 measured inside three layers of mu-shielding in the lab, unshielded in the lab and unshielded at the West Head test site.

7.1 Measurement details

All subsequently measurements were made using the dual ADC which recorded 18 channels of data; 9 channels on each ADC, ADC 1 – gradiometers G1-6 plus three orthogonal fluxgate channels positioned 2.8 m the opposite side of the track and ADC 2 – M1-9.

The measurements included 1. magnetic dipole passes with the system stationary to simulate the passing of a magnetic anomaly such as a UXO, 2. Introducing small angle tilting through about ±1-2° in the geomagnetic field where the gradiometers were subjected to field variations of up to ~1000 nT along their common-mode sensitivity axes, in this case simulating the movement expected in a submerged tow vessel (also used as an in-situ calibration method). 3. Magnetic dipole passes with the system undergoing tilting, in order to fully evaluate the accuracy of our compensation algorithms.

A magnetic dipole pass consisted of the magnetic puck (a shuttle containing a 6 A.m^2 magnet) being pulled along the 16 m electrical conduit using a electric drill wound pulley system in order to attain fairly uniform travelling speed. The average time it took the puck to traverse the 16 m length was ~6 s giving an average speed ~ 2.66 m/s, however some variation was observed. The captured file length was 8 s for the puck runs. A summary of the

measurements obtained on the field trial is shown in Table 10. Sampling rates of either 1 kHz or 100 Hz was used where the lower rate was used in order to quickly visualise the data in the software.

Table 10. List of the various runs taken at West Head.

Run Number	Measurement	Gain setting (Ω)		File length (s)	Sampling rate (Hz)
		Gradiometers	Magnetometers		
1-5	Noise	30 k	30 k	32	1000
6-7	Noise	2.97 k	2.97 k	32	1000
8-10	Dipole pass	30 k	30 k	8	100
11-13	Dipole pass	30 k	30k	8	1000
14	Tilting	30 k	30 k	8	100
15-16	Tilting	30 k	2.97 k	8	100
17	Tilting	30 k	2.97 k	32	1000
18	Noise	30 k	2.97 k	32	1000
19	Noise	30 k	2.97 k	8	100
20	Dipole + tilting	30 k	2.97 k	8	100
21-22	Tilting	30 k	2.97 k	8	100
23,27	Dipole + tilting	30 k	2.97 k	8	100
24-26	Dipole + tilting	30 k	2.97 k	8	1000
Rotated system anti-clockwise by ~45 °					
28	Tilting	30 k	2.97 k	8	100
29	Tilting	30 k	2.97 k	32	1000
30-31	Dipole + tilting	30 k	2.97 k	32	1000
32-33	Dipole + tilting	30 k	2.97 k	8	100

7.2 Magnetic dipole passes with the system stationary

The data used for this analysis was taken from run #12 where both magnetometers and gradiometers were in high sensitivity/low dynamic range setting. For this stationary measurement, the tilt table was clamped into a horizontal position. The system was orientated with SQUID magnetometer M9 parallel with the track as shown in Figure 64. Figure 66 (a) shows the raw gradient fields measured by the six gradiometers as the magnetic puck is passed by at a average speed of ~ 2.66 m/s, however some variation in the speed of the puck over the length of the run was expected. From this data then the five independent tensor components are extracted (Figure 66 (b)). For this stationary case, with no compensation applied, the calculated scaled moment (Figure 66 (c)) is a reasonably good match to a forward modelled calculation of the scaled moment.

Figure 66 (d) shows the tracking of the magnet for puck run #12 using the tensor components shown in (b), the inversion gives successive positions for a 2 s (~5 m) series around the closest point of approach (CPA). The dashed line presents the true path of the puck. The dots represent the magnet positions every 0.02 s. This shows the puck is being tracked extremely well at positions within ± 1m of the CPA.

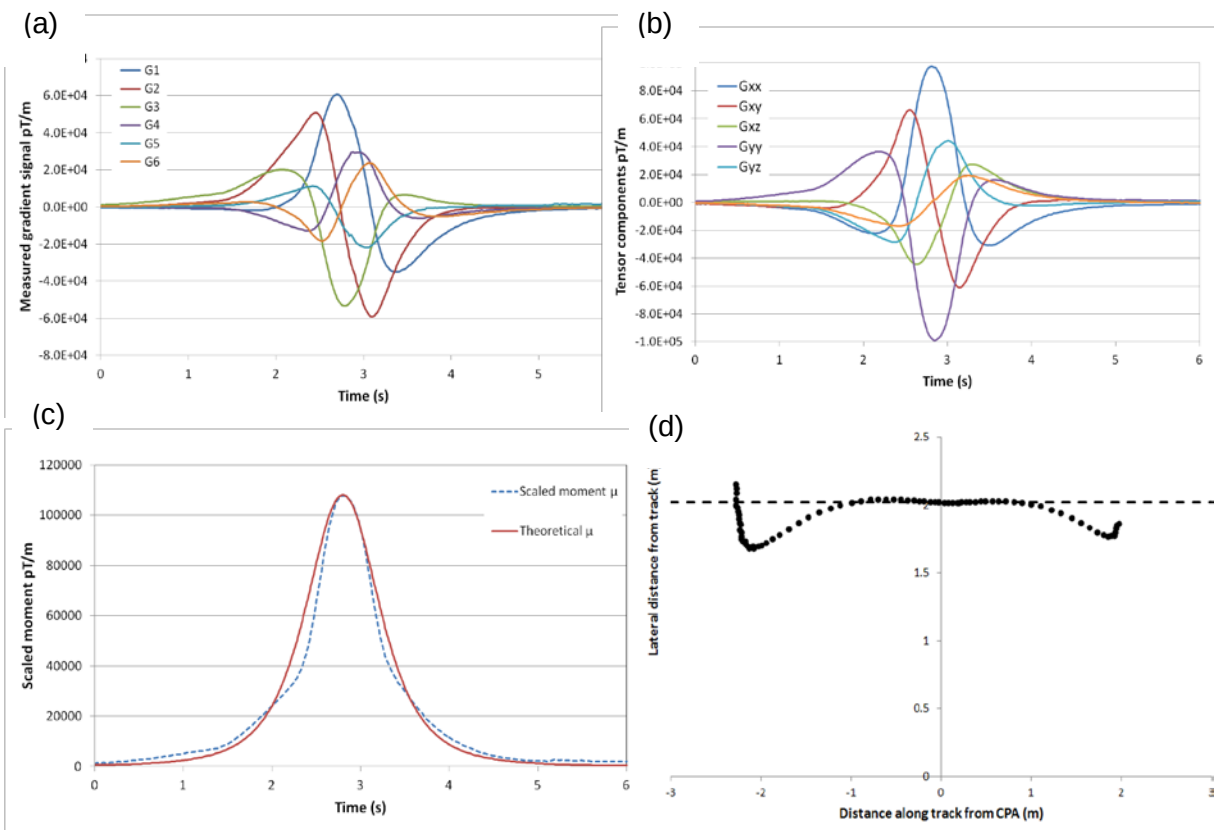

Figure 66. (a) the raw gradient fields measured by the six gradiometers as the magnetic puck is passed by at a average speed of ~ 2.66 m/s, (b) the extracted five independent tensor components, (c) calculated scaled moment plotted with the theoretical moment and (d) the tracking of the magnet for puck run #12 using the tensor components.

This plot shown is essentially a plan view. It is a projection onto the subhorizontal (dip 6°) plane that contains the track and the sensor. This is a reasonable representation because the major eigenvectors systematically rotate within this plane as the magnet passes and the intermediate eigenvector (which theoretically should be perpendicular to the plane that contains the moment vector and the source-sensor displacement vector) is ~perpendicular to this plane, as it should be. The plunge of the intermediate eigenvalue at the CPA is +84°, tilted away from the puck, which is spot on where it should be. The upshot is: the 3D solutions are very close to the plane of the projection, so all the information is essentially shown in this plot.

Solutions obtained at greater distance diverge significantly from the true path. This is not thought to be a SNR issue but rather to do with systematic errors in the tensor components due to inaccuracies in the calibration. The intervals between successive positions suggest systematic variations in the speed of the puck, although the average speed over this interval is about right. There was some real speed variation.

7.3 Small angle tilting in the geomagnetic field

During test runs of tilting through about ±1-2 ° in the geomagnetic field the gradiometers were subjected to field variations of up to ~1000 nT along their common-mode sensitivity axes. These motion trials showed that due to the gradiometers finite balance each individual gradiometer had some residual sensitivity to the background field. This produced strong quasi-sinusoidal common mode signals as seen in Figure 67 (a), which allowed a test of the effectiveness of the referencing corrections. Data run #29 was used in this analysis. Figure 67 (b) shows the corresponding change in field for each of the seven magnetometers (shown also is Mx, My and Mz vector fields calculated from the combined output of all seven sensors) as the system was rocked back and forth.

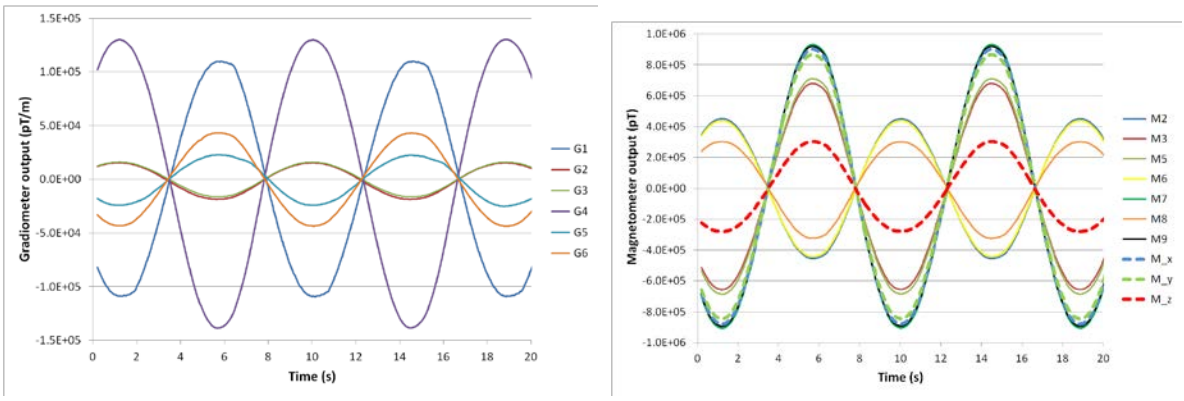

Figure 67. While the system was in motion, the non-ideal common mode rejection of the Earth's background fields shown in (a) for all planar gradiometers. Correction for this unwanted signal was provided via the signals associated with the linked movement of vector magnetometers shown in (b) for the in-field calibration.

Correction coefficients were determined by applying known uniform fields to the system, generated inside the Lindfield CSIRO laboratory using the Ruben's coil sets, and correlating each gradiometer response to the measured magnetometers outputs. These "lab" determined coefficients were then applied to run #29 as seen in Figure 68 (a)-(f) (corresponding to G1-G6 respectively). The LHS shows the raw gradiometer response to tilting versus the estimated common mode response, calculated from the output of the magnetometers and the lab coefficients. On the RHS, the raw gradiometer response is again plotted but with the balanced gradient this time.

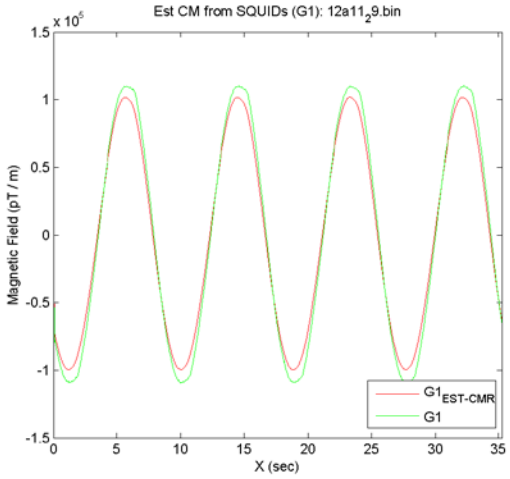
Est CM from SQUIDs (G1): 12a11_29.bin
x 10^-5
Magnetic Field (pT / m)
X (sec)
G1EST-CMR
G1

(a)

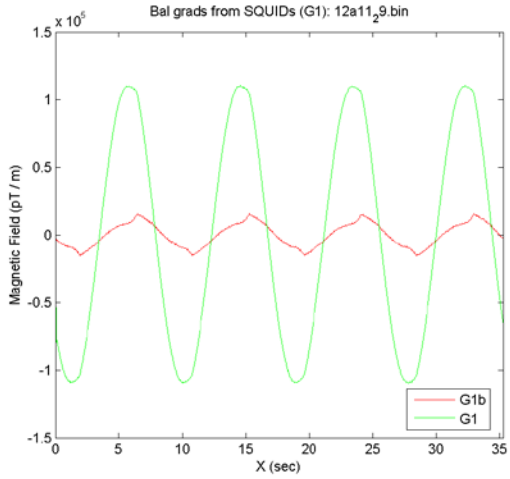
Bal grads from SQUIDs (G1): 12a11_29.bin
x 10^-5
Magnetic Field (pT / m)
X (sec)
G1b
G1

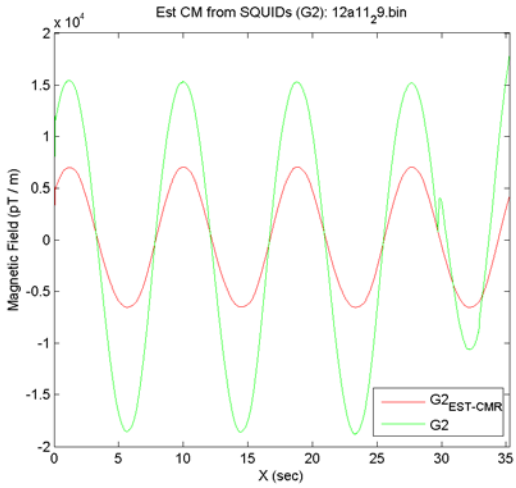
Est CM from SQUIDs (G2): 12a11_29.bin
x 10^-4
Magnetic Field (pT / m)
X (sec)
G2EST-CMR
G2

(b)

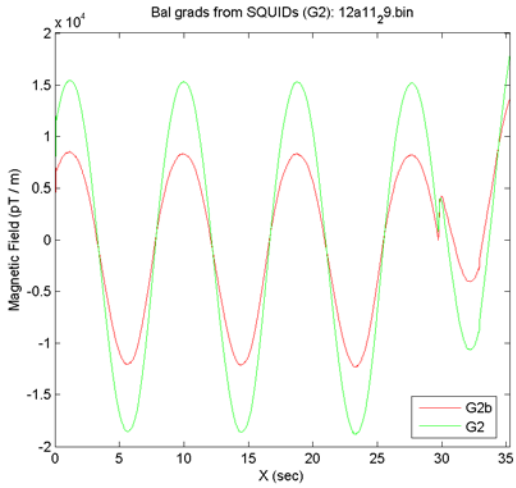
Bal grads from SQUIDs (G2): 12a11_29.bin
x 10^-4
Magnetic Field (pT / m)
X (sec)
G2b
G2

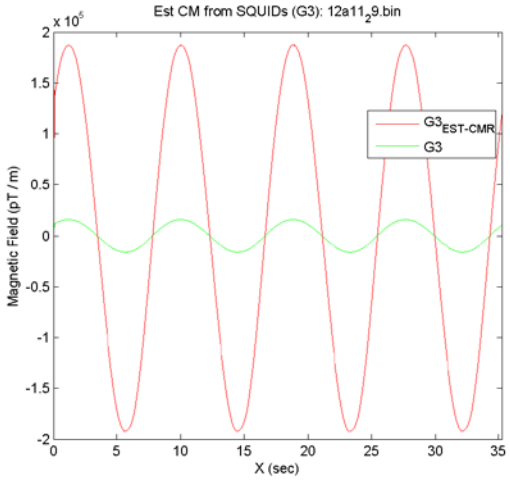
Est CM from SQUIDs (G3): 12a11_29.bin
x 10^-5
Magnetic Field (pT / m)
X (sec)
G3EST-CMR
G3

(c)

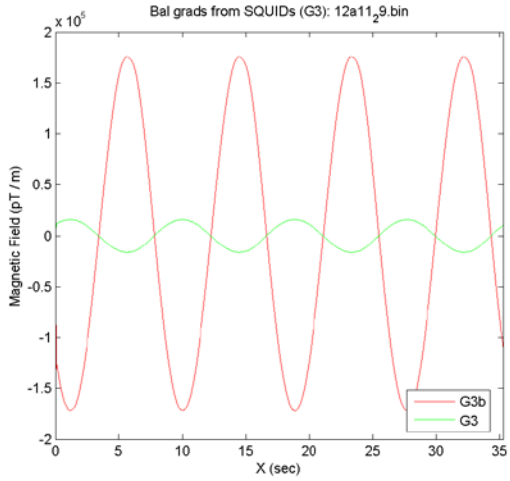
Bal grads from SQUIDs (G3): 12a11_29.bin
x 10^-5
Magnetic Field (pT / m)
X (sec)
G3b
G3

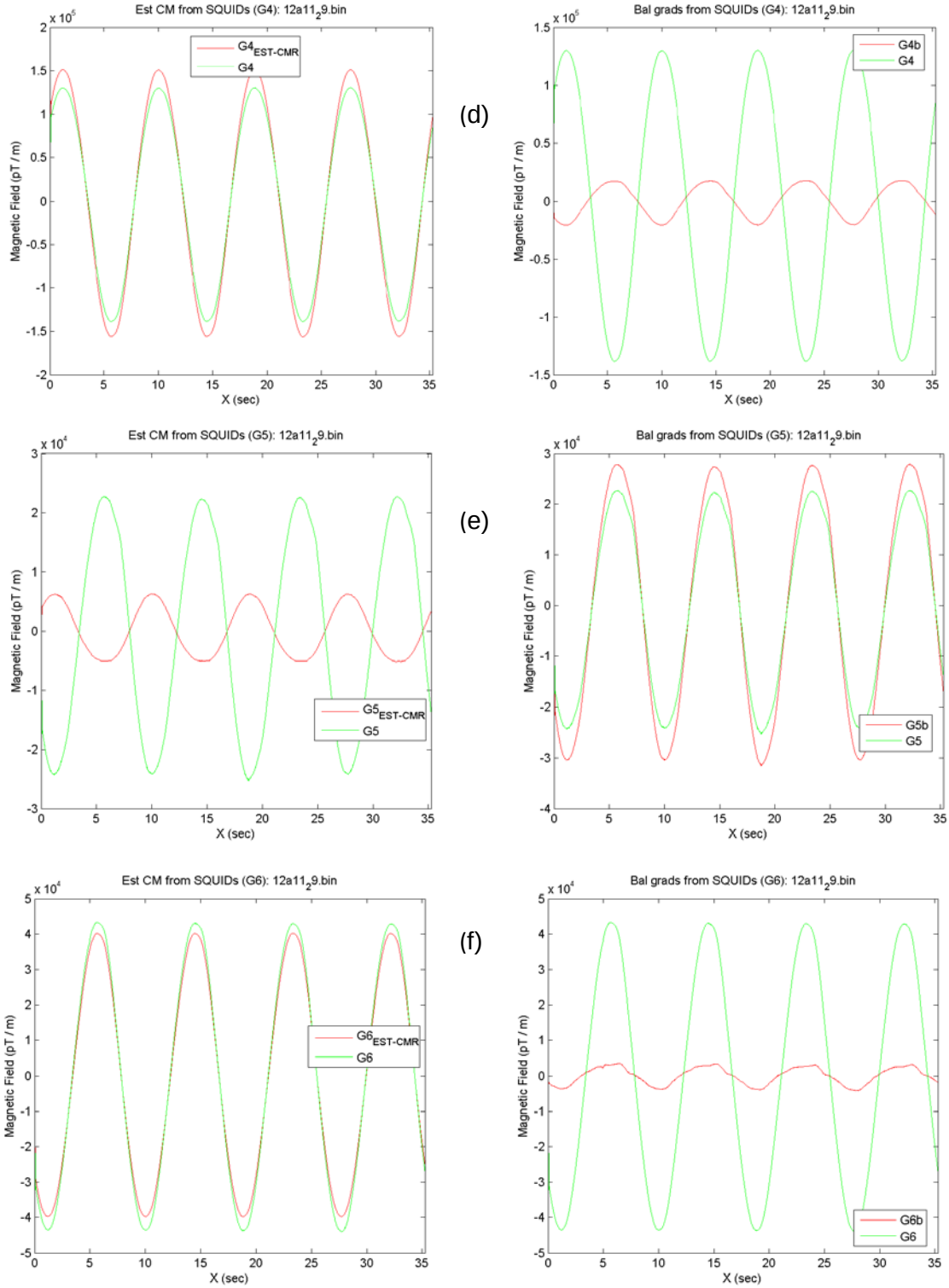

Figure 68. (a)-(f). Corresponds to gradiometer G1-G6 respectively, LHS: shows the gradiometer output (green) and the estimated common mode signal calculated from the "lab" balancing routine using the reference SQUID magnetometers (red). RHS: The gradiometer output (green) and the balanced gradiometer signal (red)

As we can see from the balanced outputs of each gradiometer the “lab” determined coefficients have trouble to completely remove the common mode signal. In some cases (G3 and G5), the balanced output contains more motion noise than the raw data. Whereas in other cases (G1 and G6), the balancing routine does reasonably well. In any case it appears that the intercalibration of the gradiometers and the referencing coefficients determined in the lab (which correct the measured gradiometer outputs for common mode signals) is to some extent inaccurate. One reasonable explanation for this that the calibration was perturbed by induced magnetization of ferrous materials in the walls, subfloor or ceiling spaces in the lab, which produced anomalous fields and gradients in phase with the slowly varying coil fields.

7.4 Magnetic dipole passes with the system undergoing tilting

Run #30 was used for the analysis of the magnetic dipole pass with tiling in the geomagnetic field. This essentially combined both measurements 1 and 2 to ultimately test the ability to track a moving target whilst the sensor system is undergoing motion. Figure 69 shows the results for each of the six gradiometers G1-6 (from top to bottom, left to right). Each plot shows the raw gradient measured signal (blue), the estimated common mode signal obtained from the lab calibration (red) and the balanced gradiometer output (green).

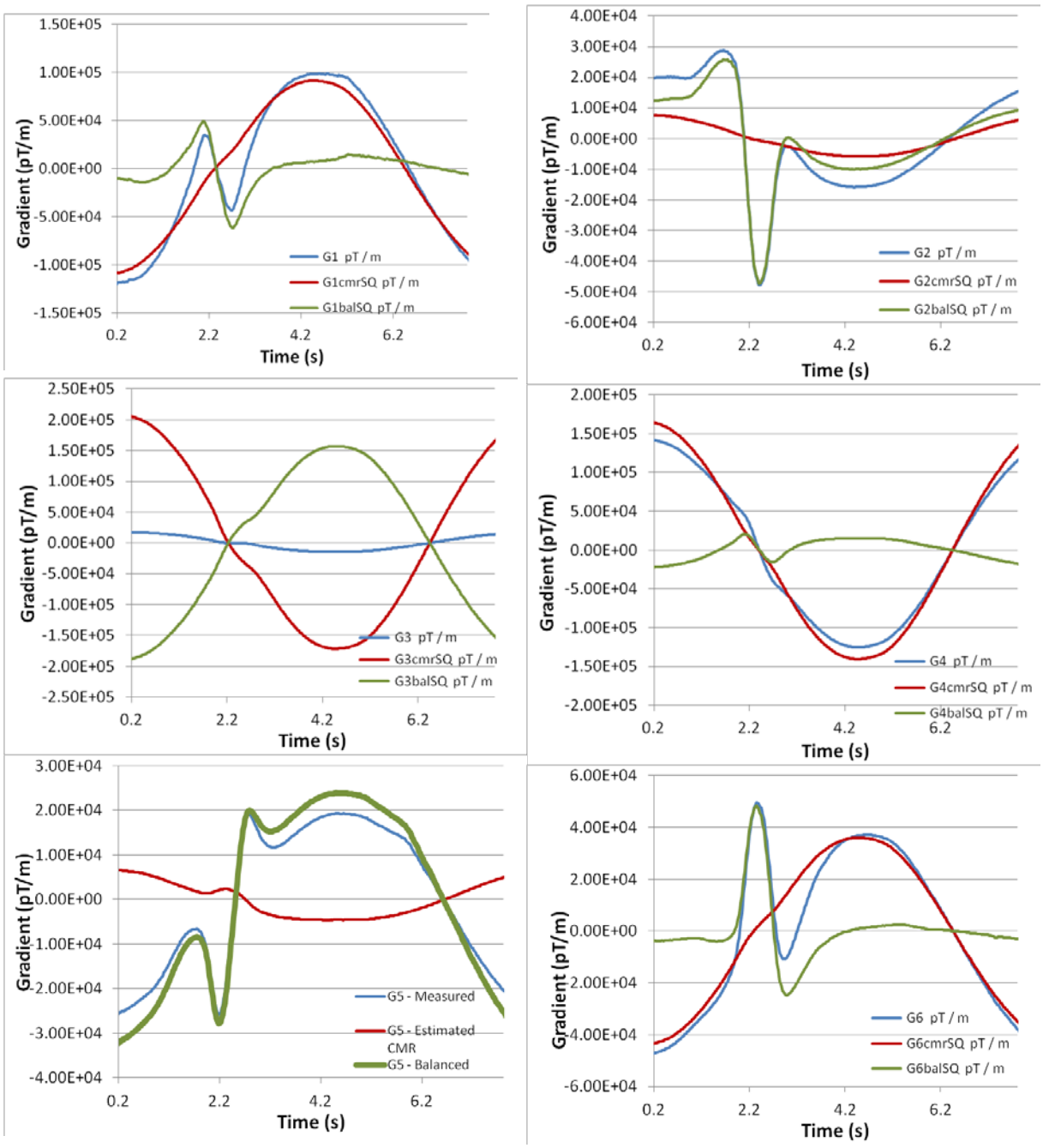

Figure 69. shows the raw gradient measured signal (blue) for each of the six gradiometers G1-6, the estimated common mode signal obtained using lab field calibration (red) and the balanced gradiometer output (green).

Again as in the case of Run #29 shown previously, the estimated common mode signal doesn't reliably compensate for the changes seen by the gradiometer. This is especially true for G2, G3 and G5. G1, G4 and G6 have reasonably good cancelation of the common mode. Run #29 provided time series of magnetometer and gradiometer outputs during tilting in a constant low gradient. As an alternative to the coefficients obtained from the lab, this data was used to derive two new sets of referencing coefficients, one that included time derivatives of outputs from three approximately orthogonal magnetometers M7, M8 and M9, and a second that only fitted terms proportional to those magnetometer outputs to the time variations of gradiometer signals. These sets of referencing coefficients were then applied to data acquired in run #30.

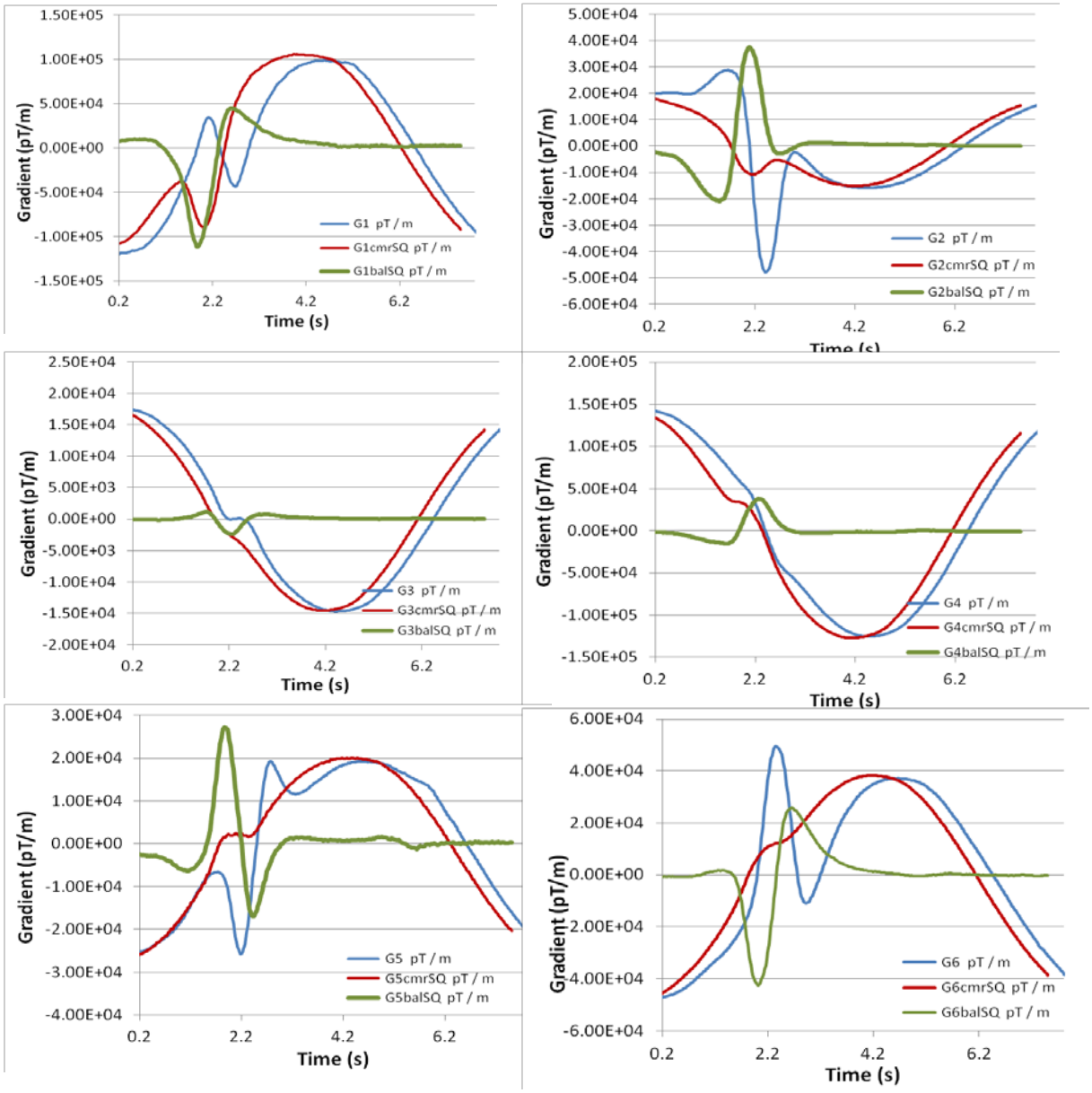

Figure 70. shows the raw gradient measured signal (blue) for each of the six gradiometers G1-6, the estimated common mode signal obtained using the field calibration *with* time derivatives (red) and the balanced gradiometer output (green)

Figure 70 shows as before the raw gradient measured signal (blue) for each of the six gradiometers G1-6, the estimated common mode signal obtained using the field calibration included time derivatives of outputs from three approximately orthogonal magnetometers M7, M8 and M9 (red) and the balanced gradiometer output (green). Figure 71 shows the same data but without the time derivative component included.

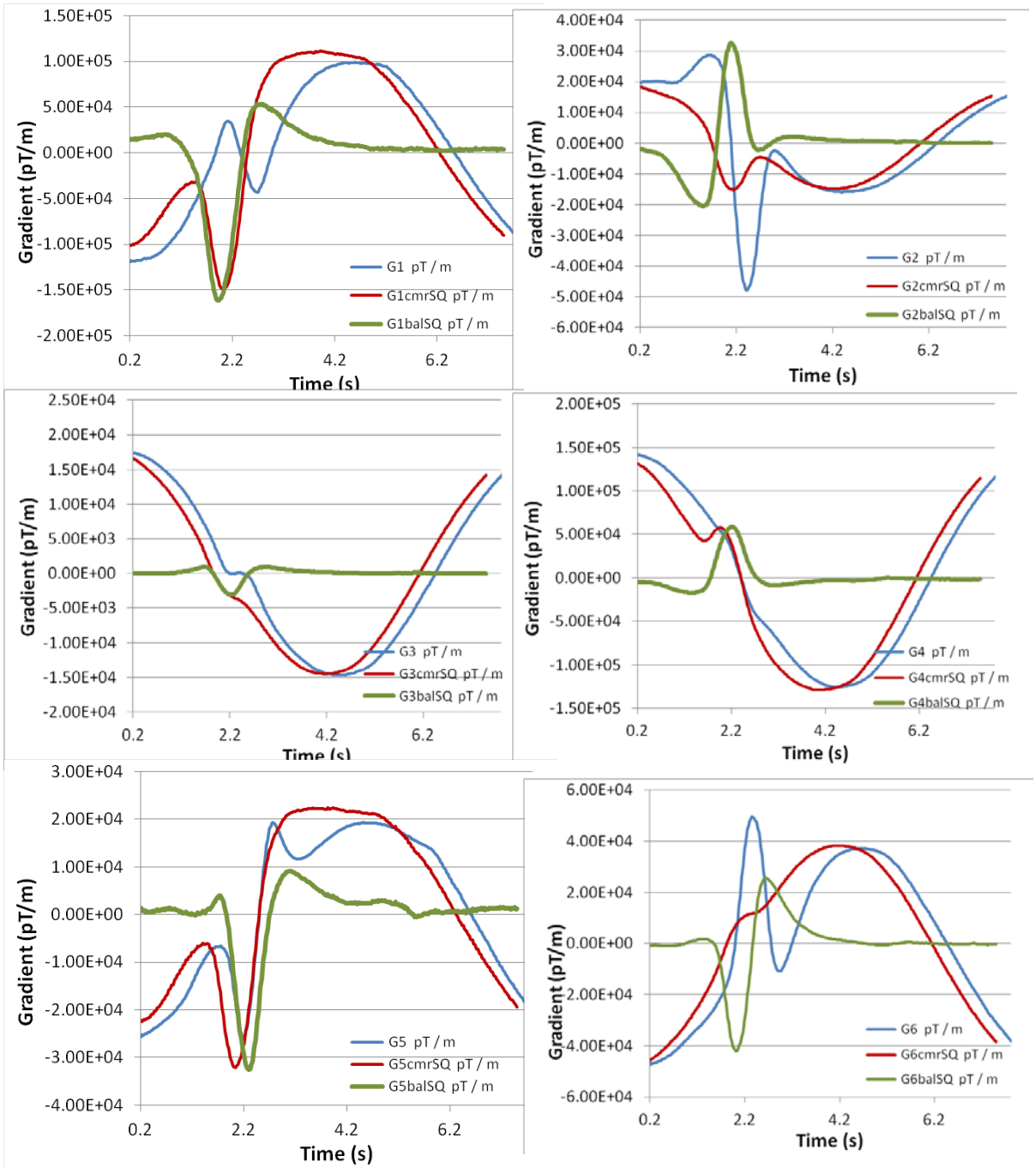

Figure 71. shows the raw gradient measured signal (blue) for each of the six gradiometers G1-6, the estimated common mode signal obtained using the field calibration *without* time derivatives (red) and the balanced gradiometer output (green).

Figure 72 shows a comparison of the common mode signal obtained from all three calibration techniques.

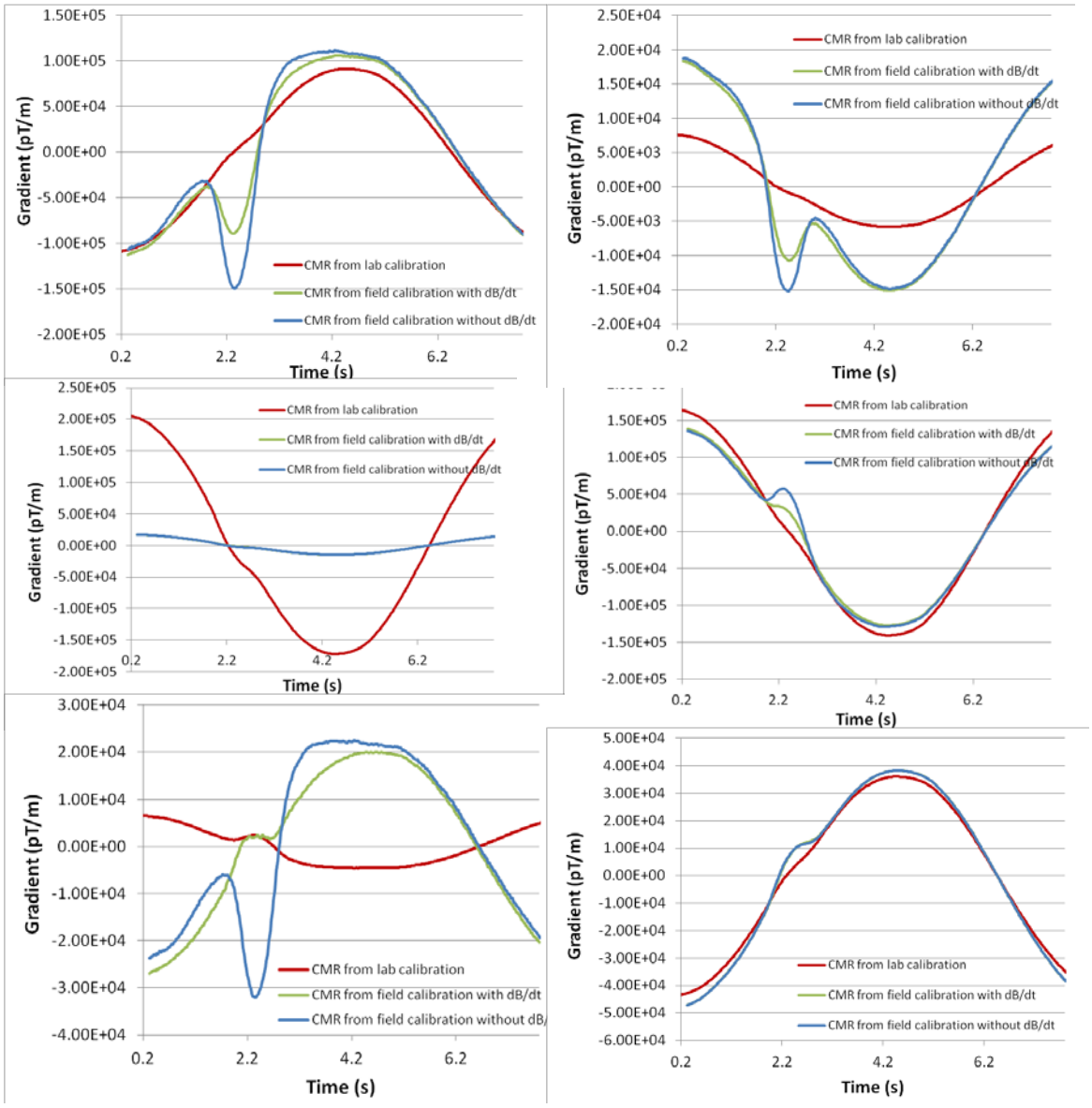

Figure 72. Shows the estimated common mode signal obtained from the lab (red), the field calibration with dB/dt term included (green) and without the dB/dt term included (red) for each of the six gradiometers G1-6.

7.5 Analysis of results

To highlight the difference the inclusion or exclusion of time derivative components we can look at two gradiometers G6 and G5 individually. Figure 73 shows the uncorrected gradient measured by sensor G6 during run #30. Between about two seconds and four seconds from the beginning of the run the signature of the passing dipole is clearly visible, superimposed on a large, slowly varying curve that represents the common mode signal associated with tilting in the geomagnetic field. Figure 74 shows the residual signal after referencing correction. The dipole signature has been cleanly isolated and the residual gradient is small and constant when the dipole is distant from the sensor. For G6 there is no significant difference between referencing-corrected data with and without incorporation of time derivatives (see Figure 74).

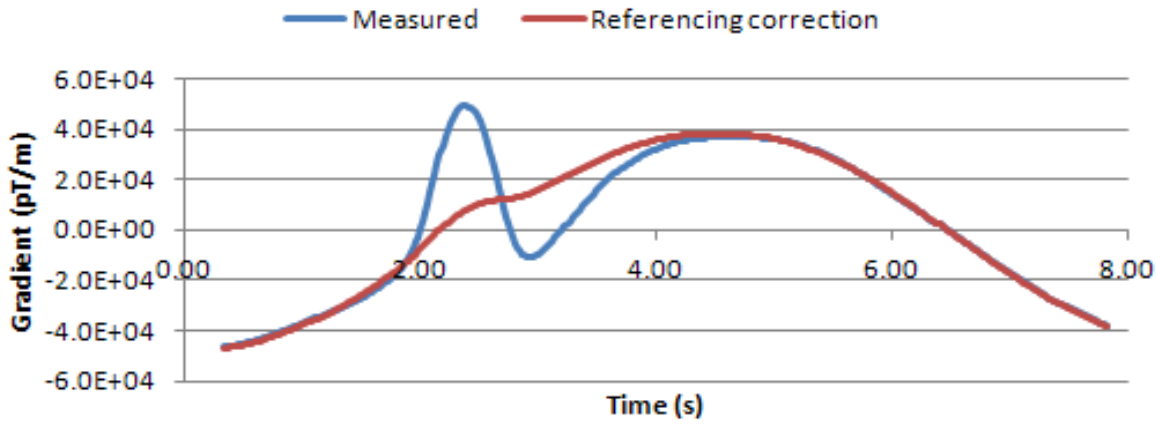

Figure 73. Comparison of the measured signal from G6 with the output predicted from the referencing magnetometer outputs, *including* time derivative terms.

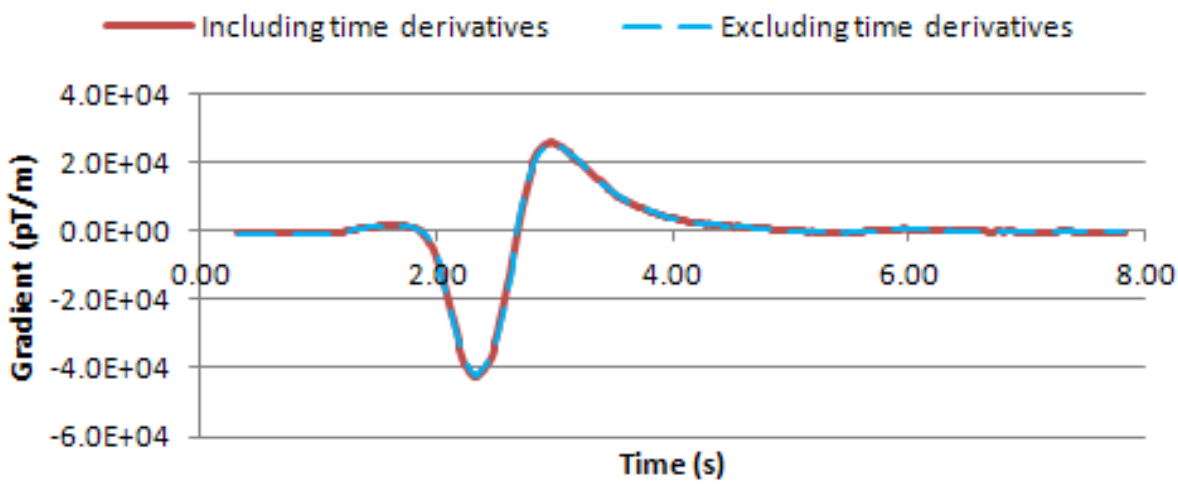

Figure 74. Residual signals from G6 after removal of the referencing correction including and excluding time derivatives. In this case incorporation of time derivative terms makes negligible difference.

For some other gradiometers, however, there observable differences in the residual dipole signatures when time derivatives are included in the analysis (Figure 75 and Figure 76). This occurs because the passage of the dipole produces relatively rapid time variations in the measured fields when the dipole is close, superimposed on the more gradual change in fields due to the tilting. For G5 the time derivative terms contribute a dipole-like signature around the time of closest approach, with negligible contribution when the dipole is distant. The amplitude of this contribution is 13% of the total range of the referencing correction. Most of the discrepancy between the referenced signals, with and without time derivative terms, is probably due to the fact that the non-unique referencing coefficients, which efficiently remove the tilting, do not effectively remove the common mode responses to **B** and d**B**/dt produced by the magnet itself. This also implies that the "reference-corrected" gradient tensor elements are not perfectly accurate, due to the incorrectly removed magnet fields. Correctly determined "universal" referencing coefficients would suppress common mode contributions, irrespective of their origin.

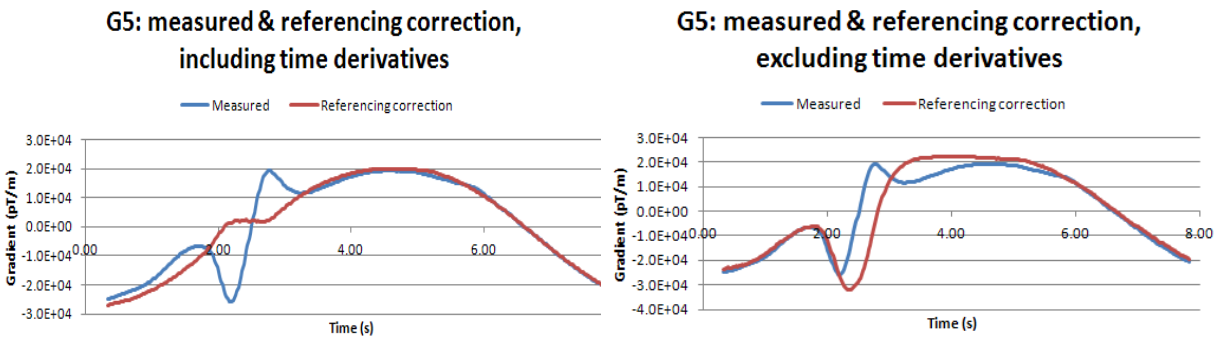

Figure 75. Comparison of the measured signal from G5 with the output predicted from the referencing magnetometer outputs, with time derivative terms (left) and without them (right).

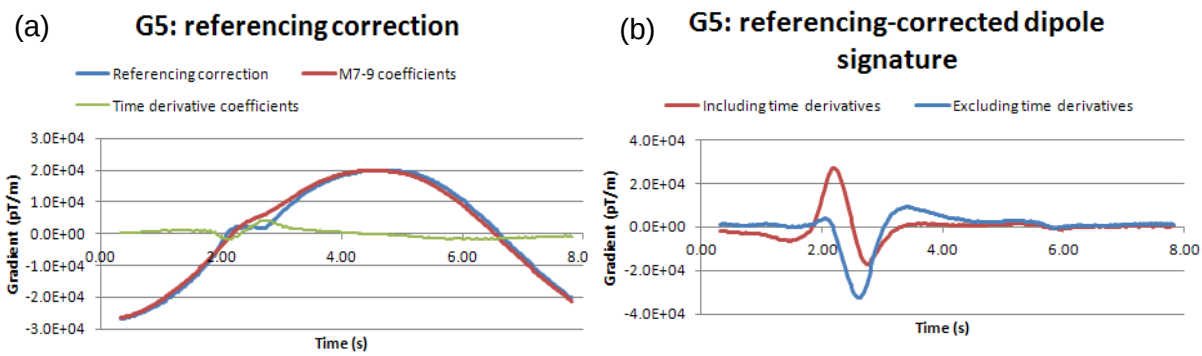

Figure 76. (a) Referencing correction for G5 (blue), decomposed into contributions of magnetometer readings (red) and time derivative terms (green). (b) Residual signals from G5 after removal of the referencing correction. In this case incorporation of time derivative terms makes a significant difference.

Figure 77 shows referencing-corrected signals for all gradiometers, using the lab coefficients and field obtained coefficients with and without inclusion of time derivative terms. Overall the dipole signature appears to be well separated from the tilting effects.

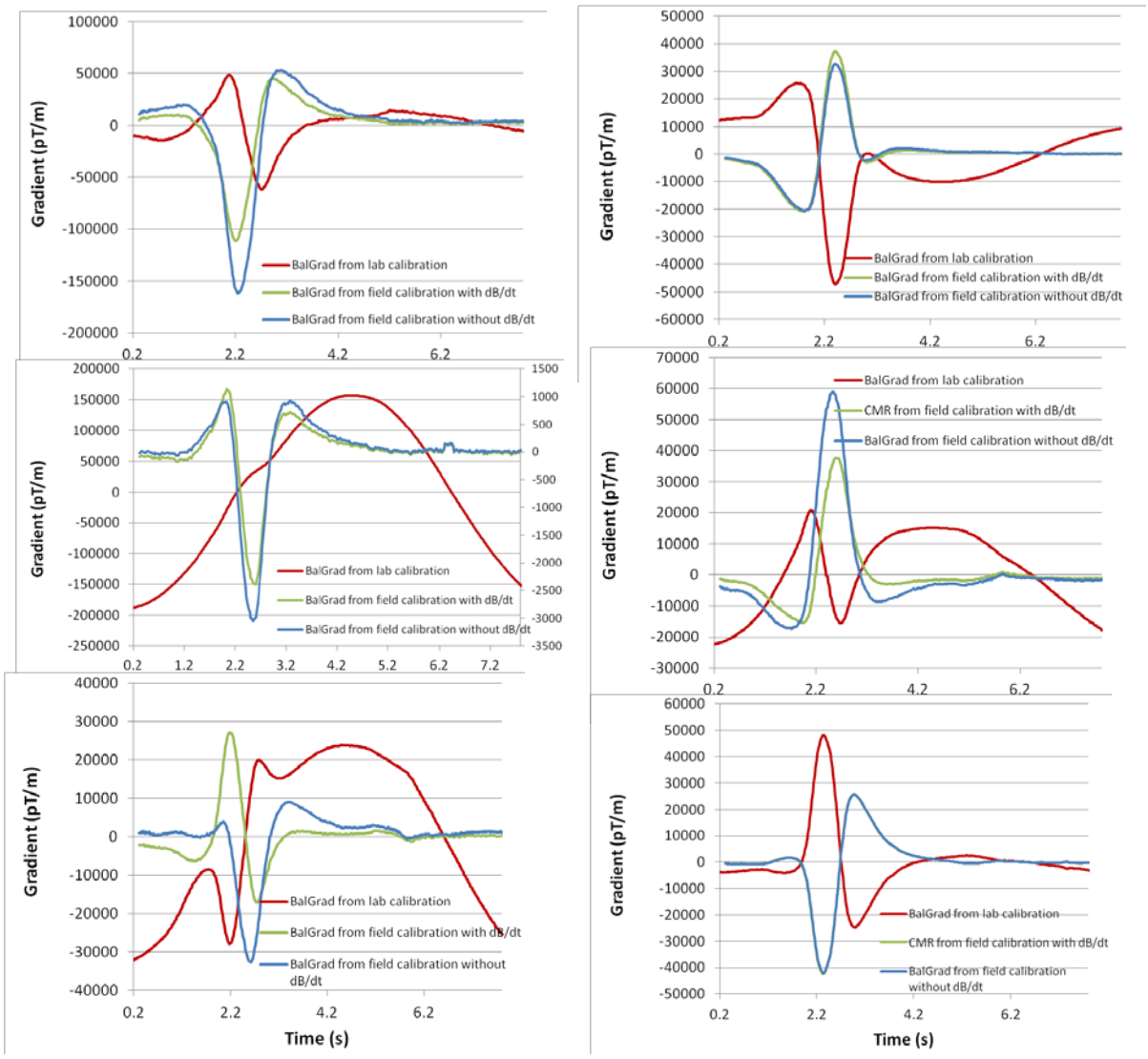

Figure 77. Referencing-corrected signals for all gradiometers, using the lab coefficients and field obtained coefficients with and without inclusion of time derivative terms.

Figure 78 (a) gives the extracted tensor components from the balanced gradiometer outputs using time derivative field derived coefficients. Comparison of the referencing-corrected gradient tensor elements with forward modelling of these elements for a magnet moving uniformly at its measured average speed, seen in Figure 78 (c), showed quite good agreement in anomaly shapes, but with some systematic differences in relative anomaly amplitudes. These differences are attributed to inaccuracies in the intercalibration of the different gradiometers, due to the perturbations of the laboratory gradients. Assuming this to be the case, the anomaly amplitudes were renormalised to match the correct relative amplitudes and then used to invert for the magnet positions at successive measurement times. The results seem to support this assumption, because the inverted magnet positions track the inferred motion quite well, which would not be the case if the forms of the tensor element anomalies were badly distorted. The major eigenvectors lie close to the plane containing the track and the sensor, which dips ~6° towards the track, and systematically

rotate as the magnet moves past. The intermediate eigenvectors are consistently subvertical, approximately perpendicular to this plane, as they should be according to dipole tracking theory. Thus the inverted positions always lie close to this plane when the dipole signature is clearly present. The results, projected onto this plane are plotted below, see Figure 78 (c). The dots represent successive positions at 0.02 s intervals and the dashed line represents the actual path. For an approximately 5 m segment of the track around the closest point of approach, the magnet appears to move progressively along a path that meanders around the correct track. The smoothness of the path suggests that random noise is not significantly affecting the results, so the errors appear to be systematic. This is not surprising given (i) the roughness of the "calibration", and (ii) the imperfect removal of common mode effects arising from the dipole fields, for which the appropriate referencing coefficients had not been determined.

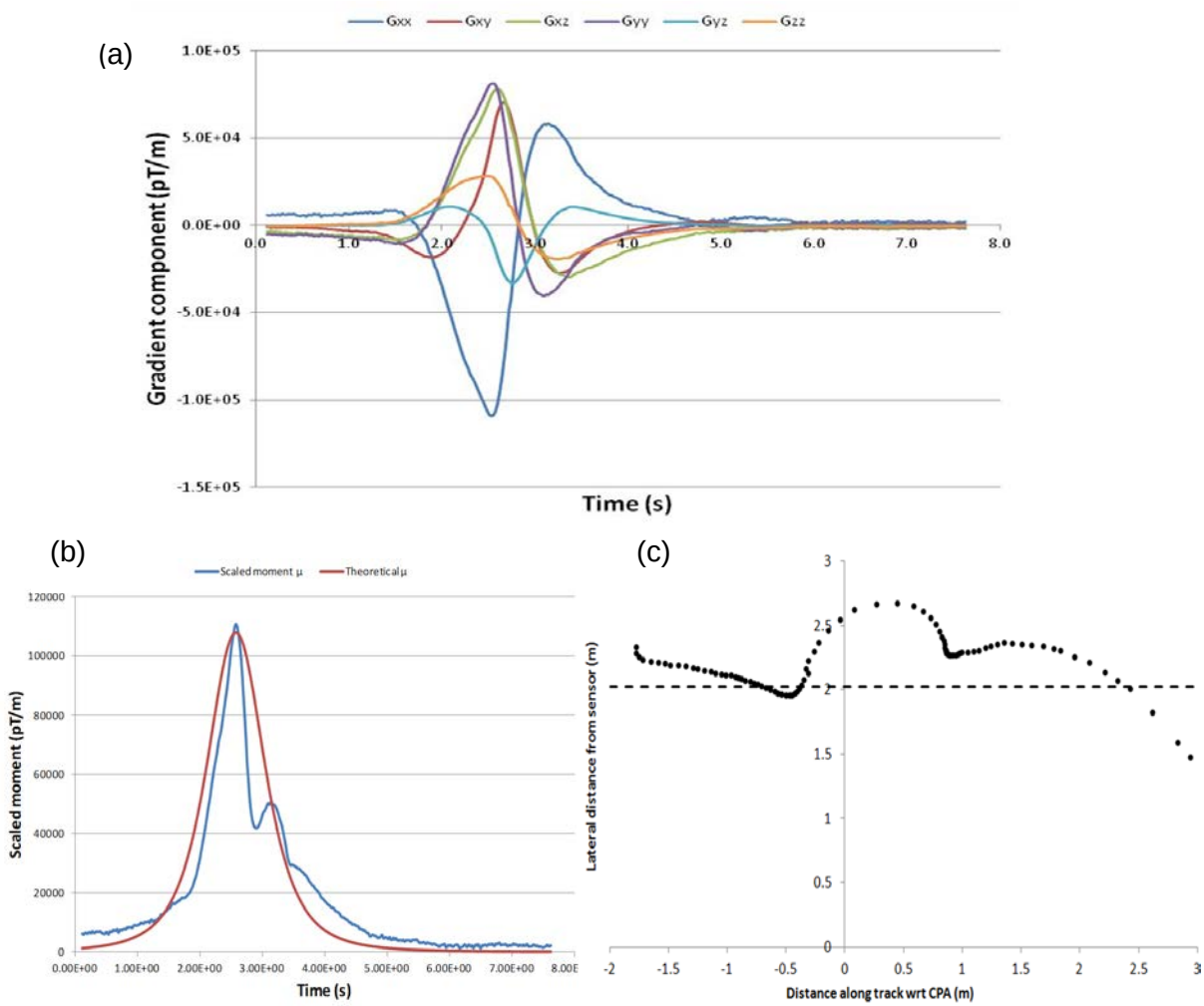

Figure 78. (a) the extracted five independent tensor components from the balanced gradiometer outputs using time derivative field derived coefficients, (c) calculated scaled moment plotted with the theoretical moment and (d) the tracking of the magnet for puck run #30 using the tensor components.

Figure 79 (a) shows a similar analysis for a stationary sensor, without any referencing corrections being applied (previously shown in section 7.2). The results are quite good, but apparent changes in speed (some of which may be real) and relatively small, but systematic, errors in position are evident. These probably arise from the common mode effects of the

magnet fields, which are uncompensated in these data. Figure 79 (b) shows results for the same run, this time using inappropriate referencing coefficients derived from tilt test. The systematic trend away from the correct track shows the importance of determining the correct referencing coefficients.

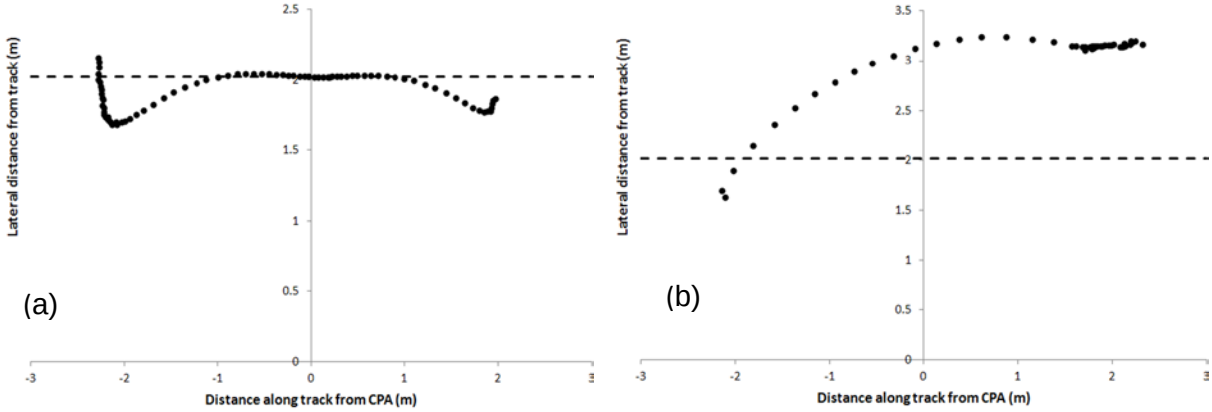

Figure 79. Non-tilting platform – calculated path of moving magnet, without referencing corrections (a) and with inappropriate referencing corrections for magnet fields, derived from tilt tests (b).

Applying the coefficients generated using the relationship between the unwanted, common mode, gradiometer signals and the response of the magnetometers while the system was tilted in the Earth's field at West Head allowed us to accurately remove significant proportions of the gradtiometers common mode response. The coefficients proved to be non-unique, as rotating the sensor approximately 45° on the moving platform produced another set of compensation coefficients. The reason for this is multicollinearity of gradiometer outputs and referencing magnetometer signals, which all vary in tandem as the system tilts. The best fit referencing coefficients for tilting within a single plane are therefore ambiguous – many alternative choices would work as well for that motion. A universally applicable set of referencing coefficients requires tilting in several different directions to resolve this ambiguity, or else application of accurately known, highly uniform fields and gradients in a magnetically clean environment.

Table 10 shows results for run #29, for which all referencing magnetometers stayed in lock and did not clip. The rms common mode signals for the six gradiometers ranged from

~12 nT/m to ~97 nT/m. Referencing using outputs from three orthogonal referencing magnetometers (M7, M8, M9) successfully removed more than 99% of the common mode signal. Including other magnetometers in the regressions made little difference. The residual common mode signals after referencing correction contain a small quadrature component. When time derivatives of the M7-9 outputs were included in the referencing, the residuals were slightly smaller.

The referencing coefficients were determined by performing a multilinear regression of the gradiometer outputs against: (i) M7-9 magnetometer outputs, and (ii) outputs from M7-9 and their time derivatives; from the run 29 tilting run, without magnet pass. These coefficients were then applied to run 30 and 31, which had a magnet pass during tilting. The coefficients are highly nounique, due to multicollinearity of all the referencing inputs, so they can only faithfully remove similar motions. The long wavelength tilting variation is removed fairly well in runs 30 and 31. Residual errors are probably due to the the magnet fields and their time

derivatives, which are not fully removed by the particular set of referencing coefficients from the run 29 tilt test.

Table 11. Results from applying the in-field derived coefficients to Run 30.

SUMMARY	pT/m	WITH d/dt	WITHOUT d/dt	WITH d/dt	WITHOUT d/dt
GRADIOMETER	RMS OUTPUT	RMS DIFF.	RMS DIFF.	RE (%)	RE (%)
G1	80001	726	989	0.91	1.24
G2	12165	250	282	2.03	2.29
G3	11504	38	39	0.33	0.34
G4	96629	516	596	0.53	0.62
G5	17058	542	682	3.18	4.00
G6	31062	320	323	1.03	1.04

	WITH d/dt	WITHOUT d/dt	WITH d/dt	WITHOUT d/dt
average gradient	stdev(rmsdiff)	stdev(rmsdiff)	RE (%)	RE (%)
41403.16667	244.87929	338.0872175	0.59145063	0.816573332

The rms residual for an equally weighted combination of gradiometer outputs (as is used in calculation of the gradient tensor) is ~240 pT/ m (at a 50 Hz sampling rate) for an uncorrected common mode signal of ~41 nT/ m. This represents removal of 99.4% of the common mode response by the referencing. Meeting the required specification for the instrument, however, requires further reduction of the common mode response by two orders of magnitude.

These measurements of the uncompensated common mode response in the gradiometer outputs due to small tilts, of about 1°, in the full geomagnetic field indicate that the required sensitivity specification can be met if the field seen by the devices is substantially reduced. If motions can be restricted to 5°, with associated uncompensated field variations less than ~5000 nT, averaging 5 samples at intervals of 0.02 s will give rms noise of ~2 pT/m, ten times a second, provided a field cancellation factor of ~500 can be achieved.

Field cancellation factors of this order can probably be achieved by relatively open feedback coil geometry, for example tri-axial Helmholtz or Rubens coil configurations (see next section). The requirements for field uniformity across the instrument are not too stringent, provided the responses of the individual devices are calibrated in terms of measured feedback currents.

8 Global Feedback System

A global feedback system is being developed to cancel the Earth's field at the sensors. This will not only reduce the dynamic range required by the SQUID devices but will also compensate for in-motion orientation errors and reduce 1/f noise of the SQUID devices by maintaining them continuously in a low field. We are using a 3-axis room temperature AMR sensor (Honeywell HMC1053 shown in Figure 80 along with an associated noise spectrum) as well as three single-axis high-T_c SQUID magnetometers to use as reference magnetometers for the feedback system. The AMR sensors have a magnetic field noise of ~6 nT/ √Hz at 1 Hz and the SQUID magnetometers ~ 0.2 pT /√Hz at 1 Hz. The concept was to use a two stage feedback system where the room temperature AMR sensors could be used firstly to reduce the background field and provide low field cooling for the SQUIDs. A mini-Dewar was designed so as the AMR sensors could be positioned at roughly the centre of the hexagonal pyramid (see Figure 43). Secondly the orthogonal SQUID magnetometers would take over to reduce the field noise further and provide extremely fine noise motion compensation.

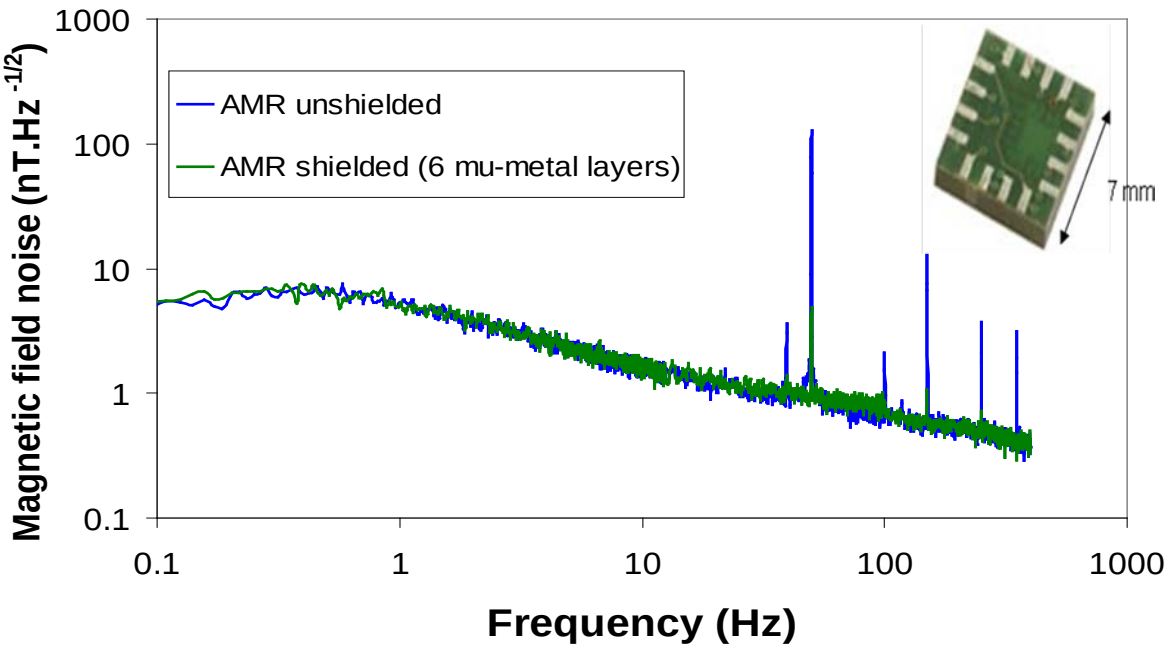

Figure 80 Noise spectra for the AMR sensor in shielding and unshielded to provide first stage noise reduction with 3 axis device shown in top right hand corner.

We are currently comparing a number of feedback coil systems, looking at the uniformity that can be achieved with a compact system suitable for underwater towing. Initially we expected to achieve the required uniformity we would require a tri- axial spherical coil set as shown in Figure 81 (a). Fabrication of which would prove extremely difficult. However, as non-uniformity across the system can be calibrated out, a coil set such as the Helmholtz coils shown in Figure 81 (b) could be used to provide adequate field compensation. Figure 81 (b) shows a tri-axial coil set used in a previous system and is available for immediate use.

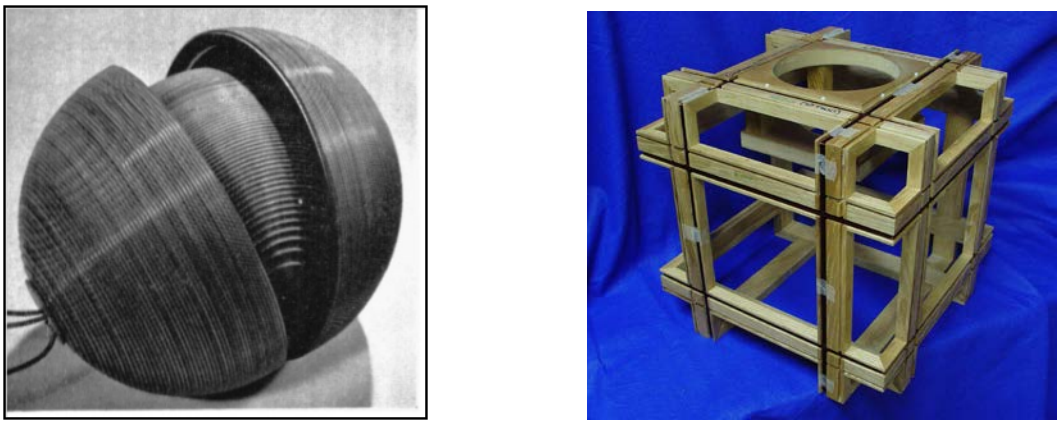

Figure 81 (a) A pair of nested spherical coils wound on hemispherical formers (Everett & Osemeikhian, 1966) and (b) a tri-axial Hemholtz coil set .

9 Wave Induced effects on Tensor measurement

9.1 Summary of work

The deconvolution algorithm for gradient tensor data acquired along an essentially linear track, in the presence of background interference, was generalized for data points that are irregularly distributed. This may be of importance when usable data are only available from a few points, or for curved or variable height tracks. Secondly, a quantitative analysis of the magnetic effects of flow of a conductive fluid around a measurement capsule was undertaken. There are two contributions to the magnetic fields and gradients. The Lorentz field associated with relative motion of the sensor and water produces an electric current, which is diverted around the insulating capsule. A magnetic field and associated gradient are produced by this perturbed electric current flow. Additionally, the diversion of water flow around the capsule also produces a local perturbation of the Lorentz field, with associated induced currents and a secondary magnetic field. This analysis will allow corrections for the flow of seawater around a towed sensor capsule, and for water motions associated with waves and currents. Modelling of EM effects of seawater flow around a measurement capsule was presented at the MARELEC and Oceans '10 conferences. The analysis has been applied to calculating the combined effect of perturbing both the wave-induced electric current density and wave-induced water motion on the electric and magnetic fields, when a measurement capsule is inserted into the seawater or is towed through the water. DLC algorithms for current dipoles in a conductive medium such as seawater and for line currents in cables, for example have also been developed. Although these sources are not the primary targets for this system, the methods may prove useful in underwater environments with cultural noise.

The following sections discusses how measurements of quasistatic electric and magnetic fields and their gradients in the ocean are affected by electric current flow in the conductive medium, which is distorted by insulating capsules that enclose sensors and their associated electronics. We also present simple new methods for direct inversion of gradient tensor data for the location and magnetic moment vector of compact targets

9.1.1 ELECTRIC AND MAGNETIC FIELDS IN AND AROUND AN INSULATING SPHERICAL CAPSULE

Electric and magnetic fields within a medium of conductivity σ are perturbed by the measurement process. In particular, sensors located within or around an insulating measurement capsule measure fields that are modified by the diversion of conduction currents around the capsule. In air or free space the gradient tensor is symmetric, as well as traceless. In the presence of conduction currents the curl of **B** is non-zero and the gradient tensor is asym-metric. This raises the question of what is actually measured by magnetometers and gradiometers immersed in the electrically conductive ocean. In particular, how does the signal measured within a sealed capsule (within which the gradient tensor is symmetric) relate to the field components and the asymmetric gradient tensor that existed in the surrounding medium prior to insertion of the measurement package?

If a uniform applied electric field gradient is present, the unperturbed field is given by:

$$\mathbf{E}_0(\mathbf{r}) = \overline{\mathbf{E}}_0 + \nabla\mathbf{E}_0.\mathbf{r}, \tag{1}$$

where $\overline{\mathbf{E}}_0 = \overline{E}_0\hat{\mathbf{x}}$ is the average electric field over a volume symmetrically disposed about the origin and the electric gradient tensor $\nabla\mathbf{E}_0 = [\partial E_j / \partial x_i] = [E_{ij}]$,(i, j = x, y, z) is symmetric and traceless. The corresponding unperturbed potential is:

$$V_0(\mathbf{r}) = -\overline{\mathbf{E}}_0.\mathbf{r} - \frac{1}{2}\mathbf{r}.\nabla\mathbf{E}_0.\mathbf{r}. \tag{2}$$

If a spherical cavity of radius a is inserted into the unperturbed current flow, the solution of the Neumann boundary value problem for the potential is (Clark, 2009a):

$$V(\mathbf{r}) = -\frac{3}{2}\overline{\mathbf{E}}_0.\mathbf{r} - \frac{5}{6}\mathbf{r}.\nabla\mathbf{E}_0.\mathbf{r}, \qquad (r \le a) \tag{3}$$

$$V(\mathbf{r}) = -\overline{\mathbf{E}}_0.\mathbf{r}\left(1 + \frac{a^3}{2r^3}\right) - \frac{1}{2}\mathbf{r}.\nabla\mathbf{E}_0.\mathbf{r}\left(1 + \frac{2a^5}{3r^5}\right). \qquad (r \ge a) \tag{4}$$

The corresponding internal field is:

$$\mathbf{E}(\mathbf{r}) = \frac{3}{2}\overline{\mathbf{E}}_0 + \frac{5}{3}\nabla\mathbf{E}_0.\mathbf{r}, \tag{5}$$

which shows that the average electric field within the cavity is equal to 1.5 times the unperturbed field that existed at the location of the cavity centre, prior to its emplacement, and that the electric field gradient is constant within the cavity and is amplified by 5/3 compared to the applied gradient. The anomalous external field due to the cavity has a quadrupole term associated with the applied gradient, which supplements the dipole field that is associated with the average applied field over the cavity. The corresponding results for the anomalous magnetic field components are:

$$\left.\begin{aligned}
B'_x &= \frac{\mu_0\sigma}{3}\left[\left(E_{zz}-E_{yy}\right)yz - E_{xy}xz + E_{xz}xy + E_{yz}(y^2-z^2)\right] \\
B'_y &= \mu_0\sigma\left[\frac{\overline{E}_0 z}{2} + \frac{\left(E_{xx}-E_{zz}\right)xz + E_{xy}yz - E_{xz}(x^2-z^2) - E_{yz}xy}{3}\right] \\
B'_z &= \mu_0\sigma\left[-\frac{\overline{E}_0 y}{2} + \frac{\left(E_{yy}-E_{xx}\right)xy + E_{xy}(x^2-y^2) - E_{xz}yz + E_{yz}xz}{3}\right]
\end{aligned}\right\} \quad (r \le a), \tag{6}$$

$$\left.\begin{aligned}
B'_x &= \frac{\mu_0\sigma a^5}{3r^5}\left[\left(E_{zz}-E_{yy}\right)yz - E_{xy}xz + E_{xz}xy + E_{yz}(y^2-z^2)\right] \\
B'_y &= \frac{\mu_0\sigma a^3}{r^3}\left[\frac{\overline{E}_0 z}{2} + \frac{a^2}{3r^2}\left[\left(E_{xx}-E_{zz}\right)xz + E_{xy}yz - E_{xz}(x^2-z^2) - E_{yz}xy\right]\right] \\
B'_z &= \frac{\mu_0\sigma a^3}{r^3}\left[-\frac{\overline{E}_0 y}{2} + \frac{a^2}{3r^2}\left[\left(E_{yy}-E_{xx}\right)xy + E_{xy}(x^2-y^2) - E_{xz}yz + E_{yz}xz\right]\right]
\end{aligned}\right\} \quad (r \ge a). \tag{7}$$

At the centre of the cavity the anomalous magnetic field $\mathbf{B}' = \mathbf{0}$, so the magnetic field at this point is equal to the unperturbed magnetic field that existed at the same point in the conductive medium, prior to insertion of the measurement capsule. Within the cavity the resultant magnetic gradient tensor (the sum of the ambient unperturbed gradient tensor and the asymmetric anomalous tensor obtained by differentiating (6)) is symmetric. Second order gradients are constant within the cavity. For the case of a uniform applied field, the anomalous external electric and magnetic fields are those of an elementary current dipole, with moment $\mathbf{p} = I\Delta\mathbf{x} = -2\pi\mathbf{j}_0 a^3$, immersed in an infinite homogeneous conductive medium, in the limit as frequency goes to zero (Kraichman, 1970, p.3-2).

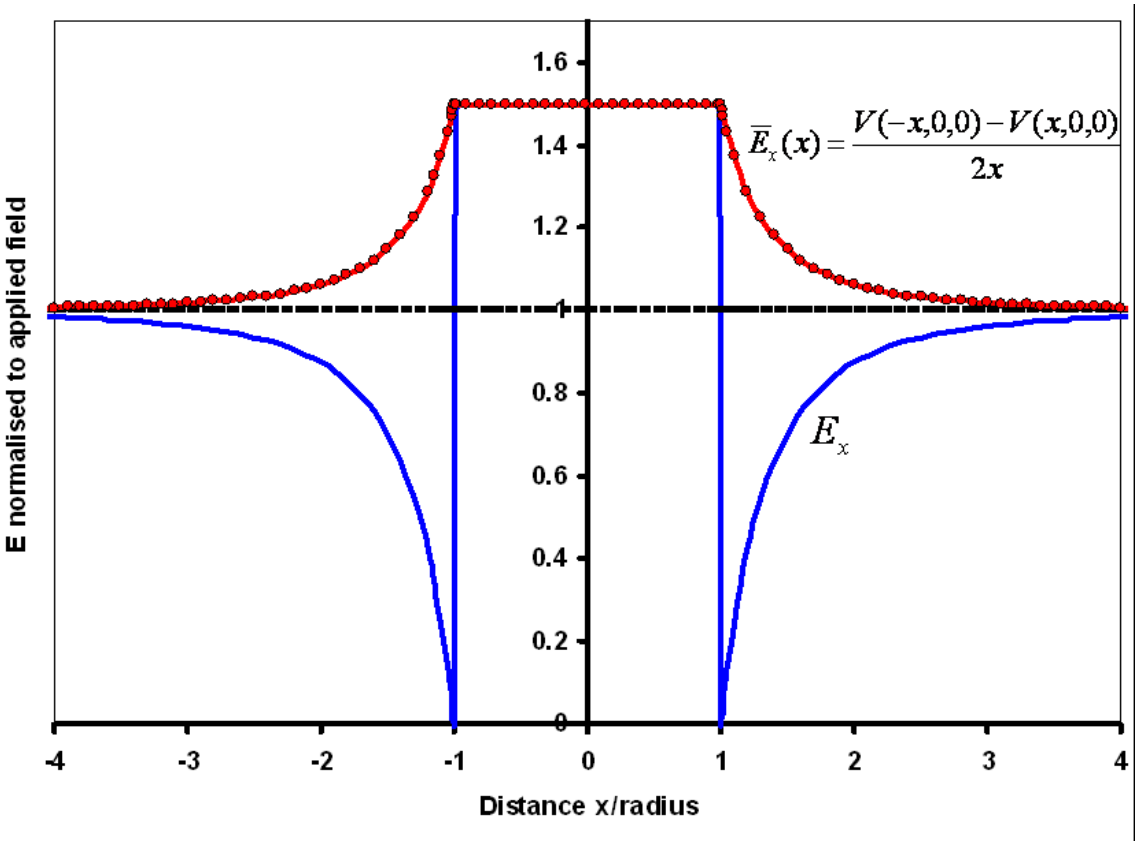

Figure 82. Electric field profile, parallel to the uniform applied field, passing through the centre of a spherical cavity.

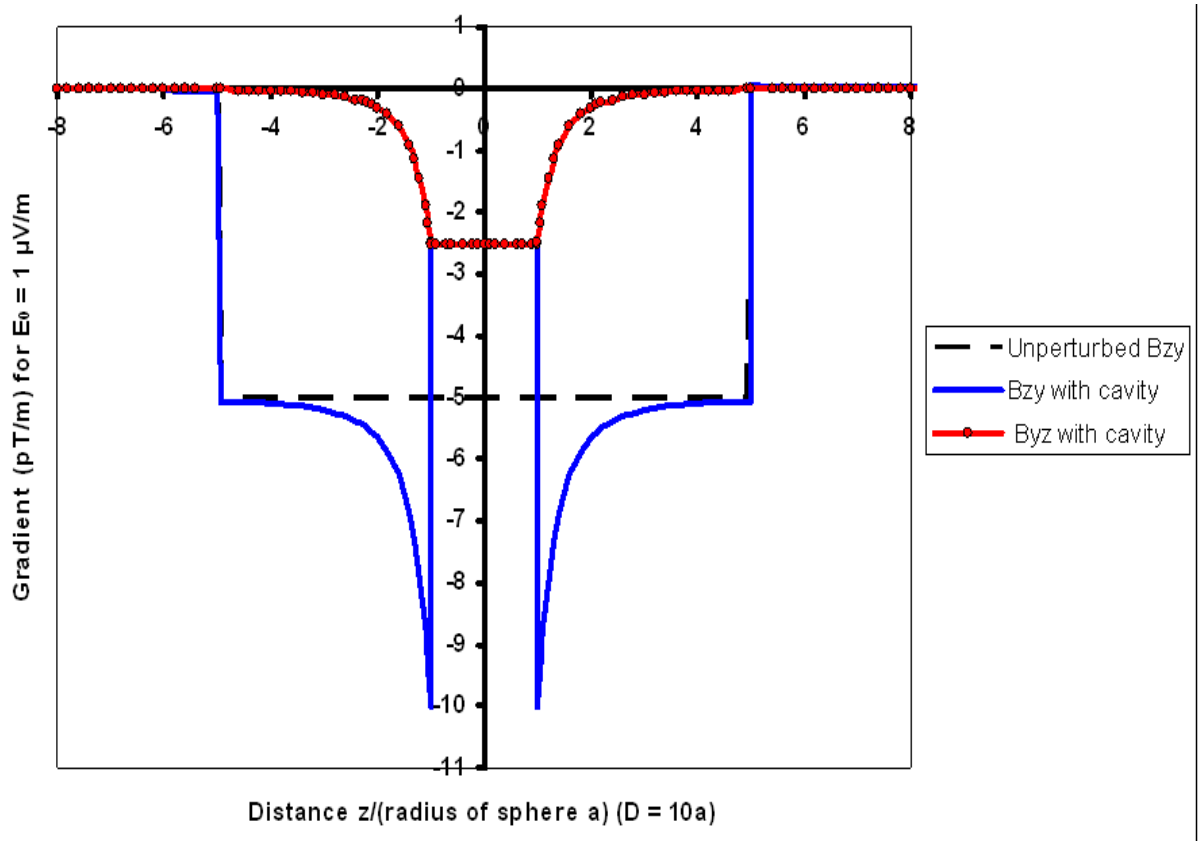

Figure 83. Magnetic gradient tensor elements along a vertical profile through the centre of a spherical cavity within a horizontal current flow distribution of limited depth extent.

Figure 82 shows the electric field along a profile parallel to a uniform applied field, passing through the centre of the cavity. **E** is discontinuous at the cavity boundary. The average value of the electric field $\overline{E}_x$ (given by the potential difference between electrodes at $\pm x$, divided by the baseline) is also shown. $\overline{E}_x$ is independent of the electric field gradient and represents the quantity measured by a standard marine electrometer, i.e.

$$\overline{E}_x(x) = \frac{V(-x,0,0) - V(x,0,0)}{2x} = \begin{cases} \overline{E}_0\left(1 + \dfrac{a^3}{2|x|^3}\right), & (|x| \geq a), \\ 1.5\overline{E}_0, & (|x| \leq a). \end{cases} \tag{8}$$

Figure 83 shows the variation of the magnetic gradient tensor elements along a vertical profile through a spherical cavity, within a horizontal current flow confined to an infinite horizontal slab of thickness equal to five times the diameter of the cavity. The assumed conductivity of the seawater is 4 Sm^{-1} and magnetic gradients are normalised to an applied electric field of 1μV/m. Within the current flow, but beyond the influence of the cavity, the only

nonzero gradient tensor component is B_{zy}. Within the cavity $B_{zy} = B_{yz}$. The influence of the cavity is significant out to $r \approx 3a$.

In many marine applications electromagnetic sensors are situated near interfaces between media of differing conductivity, such as the seafloor or the sea surface. This situation can be handled by the method of images, as discussed by Clark (2009a).

9.1.2 EFFECT OF AN ELLIPSOIDAL CAVITY

Ellipsoidal cavities can be used to model a wide variety of capsule shapes, whilst conveniently allowing analytic solutions. Consider a triaxial ellipsoidal cavity, centred at the origin, with semiaxes $a > b > c$ along x_1, x_2, x_3 respectively. In terms of ellipsoidal co-ordinates ξ, η, ζ (Kellog, 1953, p.183-184; Stratton, 1941, p.58-59) the potential V_0 associated with a uniform electric field $\mathbf{E}_0$ is:

$$\begin{aligned} V_0 = -\mathbf{E}_0.\mathbf{r} = &-(\mathbf{E}_0)_{x_1}\sqrt{\frac{(\xi+a^2)(\eta+a^2)(\zeta+a^2)}{(a^2-b^2)(a^2-c^2)}} \\ &-(\mathbf{E}_0)_{x_2}\sqrt{\frac{(\xi+b^2)(\eta+b^2)(\zeta+b^2)}{(c^2-b^2)(a^2-c^2)}} - (\mathbf{E}_0)_{x_3}\sqrt{\frac{(\xi+c^2)(\eta+c^2)(\zeta+c^2)}{(b^2-c^2)(a^2-c^2)}}. \end{aligned} \tag{9}$$

Solving the Neumann boundary value problem in ellipsoidal co-ordinates gives for the internal potential:

$$V(\xi \le 0) = -\frac{(\mathbf{E}_0)_{x_1}}{1-D_1}x_1 - \frac{(\mathbf{E}_0)_{x_2}}{1-D_2}x_2 - \frac{(\mathbf{E}_0)_{x_3}}{1-D_3}x_3, \tag{10}$$

which implies a uniform internal field given by:

$$\mathbf{E}(\xi \le 0) = -\nabla V = \left(\frac{1}{1-D_1}\right)(\mathbf{E}_0)_{x_1}\hat{\mathbf{x}}_1 + \left(\frac{1}{1-D_2}\right)(\mathbf{E}_0)_{x_2}\hat{\mathbf{x}}_2 + \left(\frac{1}{1-D_3}\right)(\mathbf{E}_0)_{x_3}\hat{\mathbf{x}}_3. \tag{11}$$

where D_i (i = 1,2,3) are the demagnetising factors of the ellipsoid along its major, intermediate and minor axes (Clark et al., 1986). The demagnetising factors sum to unity. Since

$D_1 \le D_2 \le D_3$, an ellipsoidal cavity has an anisotropic response, except in the degenerate case where all axes are equal and the cavity is spherical. Unless the applied field lies along a principal axis of the ellipsoid, the internal field is not parallel to the applied field, but is deflected away from the major axis and towards the minor axis. For a disc-like cavity

$D_3 \to 1$ as $c/a \to 0$, so the amplification of the applied electric field normal to the disc can

be very large within the cavity.

Define $R_s = \sqrt{(s+a^2)(s+b^2)(s+c^2)}$. The external potential due to an arbitrarily oriented ellipsoidal cavity is given by $V(\xi \geq 0) = V_1(\xi \geq 0) + V_2(\xi \geq 0) + V_3(\xi \geq 0)$, where

$$V_1(\xi \geq 0)_1 = -(\mathbf{E}_0)_{x_1} x_1 \left[1 + \frac{abc/2}{1-D_1} \int_{\xi}^{\infty} \frac{ds}{(s+a^2)R_s} \right] = -(\mathbf{E}_0)_{x_1} x_1 \left[1 + \frac{abc/2}{1-D_1} A(\xi) \right], \tag{12}$$

$$V_2(\xi \geq 0)_1 = -(\mathbf{E}_0)_{x_2} x_2 \left[1 + \frac{abc/2}{1-D_2} \int_{\xi}^{\infty} \frac{ds}{(s+b^2)R_s} \right] = -(\mathbf{E}_0)_{x_2} x_2 \left[1 + \frac{abc/2}{1-D_2} B(\xi) \right], \tag{13}$$

$$V_3(\xi \geq 0)_1 = -(\mathbf{E}_0)_{x_3} x_3 \left[1 + \frac{abc/2}{1-D_3} \int_{\xi}^{\infty} \frac{ds}{(s+c^2)R_s} \right] = -(\mathbf{E}_0)_{x_3} x_3 \left[1 + \frac{abc/2}{1-D_3} C(\xi) \right], \tag{14}$$

The corresponding external field components are obtained from (12)-(14) by differentiation:

$$\begin{aligned} \mathbf{E}_{x_1} &= -\frac{\partial V(\xi \geq 0)}{\partial x_1} = (\mathbf{E}_0)_{x_1} \left\{ \left[1 + \frac{abc/2}{1-D_1} A(\xi) \right] + \frac{abcA'(\xi)x_1}{2(1-D_1)} \frac{\partial \xi}{\partial x_1} \right\} \\ &+ \left[(\mathbf{E}_0)_{x_2} \frac{abcB'(\xi)x_2}{2(1-D_2)} + (\mathbf{E}_0)_{x_3} \frac{abcC'(\xi)x_3}{2(1-D_3)} \right] \frac{\partial \xi}{\partial x_1}, \end{aligned} \tag{15}$$

$$\begin{aligned} \mathbf{E}_{x_2} &= -\frac{\partial V(\xi \geq 0)}{\partial x_2} = (\mathbf{E}_0)_{x_2} \left\{ \left[1 + \frac{abc/2}{1-D_2} B(\xi) \right] + \frac{abcB'(\xi)x_2}{2(1-D_2)} \frac{\partial \xi}{\partial x_2} \right\} \\ &+ \left[(\mathbf{E}_0)_{x_1} \frac{abcA'(\xi)x_1}{2(1-D_1)} + (\mathbf{E}_0)_{x_3} \frac{abcC'(\xi)x_3}{2(1-D_3)} \right] \frac{\partial \xi}{\partial x_2}, \end{aligned} \tag{16}$$

$$\begin{aligned} \mathbf{E}_{x_3} &= -\frac{\partial V(\xi \geq 0)}{\partial x_3} = (\mathbf{E}_0)_{x_3} \left\{ \left[1 + \frac{abc/2}{1-D_3} C(\xi) \right] + \frac{abcC'(\xi)x_3}{2(1-D_1)} \frac{\partial \xi}{\partial x_3} \right\} \\ &+ \left[(\mathbf{E}_0)_{x_2} \frac{abcB'(\xi)x_2}{2(1-D_2)} + (\mathbf{E}_0)_{x_1} \frac{abcA'(\xi)x_1}{2(1-D_1)} \right] \frac{\partial \xi}{\partial x_3}. \end{aligned} \tag{17}$$

Clark et al. (1986) give explicit expressions for the demagnetising factors, the functions $A(\xi)$, $B(\xi)$, $C(\xi)$ and their derivatives with respect to ξ, and the derivatives $\partial\xi/\partial x_i$.

The volume of the cavity $\tau = 4\pi abc/3$. If the components of the unperturbed current flow with respect to the ellipsoid axes are j_1, j_2, j_3 the corresponding anomalous magnetic field is:

$$B_1'(\xi<0)=\frac{\mu_0 j_3 abcB(0)}{2(1-D_3)}x_2-\frac{\mu_0 j_2 abcC(0)}{2(1-D_2)}x_3=\mu_0\left(\frac{j_3 D_2 x_2}{(1-D_3)}-\frac{j_2 D_3 x_3}{(1-D_2)}\right), \tag{18}$$

$$B_2'(\xi<0)=\frac{\mu_0 j_1 abcC(0)}{2(1-D_1)}x_3-\frac{\mu_0 j_3 abcA(0)}{2(1-D_3)}x_1=\mu_0\left(\frac{j_1 D_3 x_3}{(1-D_1)}-\frac{j_3 D_1 x_1}{(1-D_3)}\right), \tag{19}$$

$$B_3'(\xi<0)=\frac{\mu_0 j_2 abcA(0)}{2(1-D_2)}x_1-\frac{\mu_0 j_1 abcB(0)}{2(1-D_1)}x_2=\mu_0\left(\frac{j_2 D_1 x_1}{(1-D_2)}-\frac{j_1 D_2 x_2}{(1-D_1)}\right), \tag{20}$$

$$B_1'(\xi>0)=\frac{\mu_0 j_3 abcB(\xi)}{2(1-D_3)}x_2-\frac{\mu_0 j_2 abcC(\xi)}{2(1-D_2)}x_3=\frac{3\mu_0\tau}{8\pi}\left(\frac{B(\xi)j_3 x_2}{(1-D_3)}-\frac{C(\xi)j_2 x_3}{(1-D_2)}\right), \tag{21}$$

$$B_2'(\xi>0)=\frac{\mu_0 j_1 abcC(\xi)}{2(1-D_1)}x_3-\frac{\mu_0 j_3 abcA(\xi)}{2(1-D_3)}x_1=\frac{3\mu_0\tau}{8\pi}\left(\frac{C(\xi)j_1 x_3}{(1-D_1)}-\frac{A(\xi)j_3 x_1}{(1-D_3)}\right), \tag{22}$$

$$B_3'(\xi>0)=\frac{\mu_0 j_2 abcA(\xi)}{2(1-D_2)}x_1-\frac{\mu_0 j_1 abcB(\xi)}{2(1-D_1)}x_2=\frac{3\mu_0\tau}{8\pi}\left(\frac{A(\xi)j_2 x_1}{(1-D_2)}-\frac{B(\xi)j_1 x_2}{(1-D_1)}\right). \tag{23}$$

The magnetic field within the ellipsoidal cavity is non-uniform, but has a uniform gradient. At the centre of the ellipsoidal cavity ($x_1 = x_2 = x_3 = 0$) the magnetic field is equal to the field that existed at that point before insertion of the cavity. The *resultant* internal magnetic gradient tensor is symmetric and traceless, as required. It is given by:

$$\mathbf{G}=\begin{bmatrix} B_{11}^0 & B_{21}^0+\mu_0 D_2 j_3/(1-D_3) & B_{13}^0+\mu_0 D_1 j_2/(1-D_2) \\ B_{21}^0+\mu_0 D_2 j_3/(1-D_3) & B_{22}^0 & B_{32}^0+\mu_0 D_3 j_1/(1-D_1) \\ B_{13}^0+\mu_0 D_1 j_2/(1-D_2) & B_{32}^0+\mu_0 D_3 j_1/(1-D_1) & B_{33}^0 \end{bmatrix}, \tag{24}$$

The values of the resultant gradient tensor elements depend on $\mathbf{G}_0 = [B_{ij}^0]$, which in turn depends on the configuration of the unperturbed current flow.

9.1.3 APPLICATION TO REMOVAL OF NOISE DUE TO OCEAN SWELLS

Particularly in shallow seas, electric and magnetic fields generated by the magneto-hydrodynamic action of ocean swells can significantly contaminate low frequency marine electromagnetic measurements. The theory of Weaver (1965), which has been well supported by observations, can be used to calculate the electromagnetic effects of swells. Consider gravity wave propagation at frequency *f* along the +*x* direction , which produces slowly oscillating currents parallel to the *y* axis. The components of the oscillating wave-induced field, $\mathbf{B}_{\mathrm{w}}$, in the sea water, prior to insertion of the measurement capsule, are related to magnetic gradient tensor elements measured within a spheroidal insulating capsule with a vertical symmetry axis by (Clark, 2009b):

$$\left.\begin{aligned}(\mathbf{B}_{\mathrm{w}})_x(f) &= \frac{igB_{xx}(f)}{4\pi^2 f^2},\\ (\mathbf{B}_{\mathrm{w}})_z(f) &= \frac{igB_{xz}(f)}{4\pi^2 f^2}\left[\frac{8\pi^2 f^2 z/g+1}{8\pi^2 f^2 z/g+1-4G}\right]\end{aligned}\right\} \tag{25}$$

where $i = \sqrt{(-1)}$, g = 9.8 ms^{-2}, z is the depth and $G = D_1/(1-D_1)$ is a geometric factor related to the demagnetising factor D_1 along a horizontal axis.

When other sources of magnetic field produce negligible gradients, this method effectively isolates the oceanographic magnetic noise and allows it to be removed from the measured magnetic fields using Fourier analysis (Clark, 2009b). Measured electric fields can also be corrected for wave-motion noise, by removing the swell noise $\mathbf{e} = e_y\hat{\mathbf{y}}$ given by:

$$e_y = 2\pi f(\mathbf{B}_{\mathrm{w}})_z / g. \tag{26}$$

9.1.4 NEW METHODS FOR DETERMINATION OF DIPOLE LOCATION AND MOMENT VECTOR

Another important application of magnetic sensors is the detection, location and classification (DLC) of magnetic objects, such as naval mines, UXO, shipwrecks, and archaeological artefacts. Apart from their uses in systematic magnetic surveys, gradient tensor measurements have a specific application to manoeuvrable search platforms that home onto compact magnetic targets (Wiegert and Oeschger, 2005, 2006; Wiegert et al., 2007). Compact magnetic bodies can be well represented by a point dipole source, except very close to the body. A number of methods have been proposed for locating dipole targets from magnetic gradient tensor data (e.g. Wynn et al. 1975; Wilson, 1985; Wynn, 1995, 1997). Methods based on point-by-point analysis of the eigenvectors of the tensor tend to be adversely affected by noise in individual measurements of the gradient tensor elements. Furthermore, there is an inherent four-fold ambiguity in obtaining solutions for dipole location and

orientation of its moment from point-by-point analysis of gradient tensors (Wynn et al., 1975; Wilson, 1985), which must be resolved by comparing solutions from different sensor locations, rejecting those that are not consistent (the so-called "ghost" solutions) and retaining the solutions that exhibit the best clustering. Existing methods of dipole tracking are also not robust to the contamination of the measured signal by variable background gradients, interfering anomalies, instrument drift or departures of the target from a pure dipole source.

Nara et al. (2006) have presented a neat solution to the single point dipole location problem that uses measurements of the anomalous field vector and gradient tensor, if accurate values of both are available. Along a fixed direction $\hat{\mathbf{r}}$, the field vector **b** is equal to a geometric factor, depending only on the magnitude and orientation of **m**, divided by r^3. Using this fact it can be shown that the displacement vector from the dipole to the measurement point *independent* of the orientation of **m**, is given by:

$$\mathbf{r} = -3\mathbf{G}^{-1}\mathbf{b}, \tag{27}$$

even though each tensor element and vector component on the RHS of this expression depends on $\hat{\mathbf{m}}$. Equation (27) is applicable provided det**G** is nonzero, so the matrix representation of the tensor is invertible. Although Nara et al. (2006) did not treat this aspect, once the location of the dipole is known, determination of the moment becomes a straight-forward linear inversion problem. If the anomalous field vector **b** is known to sufficient accuracy, the moment **m** = $m(L, M, N) = (m_x, m_y, m_z)$ can be calculated as (Lima et al., 2006):

$$\mathbf{m} = \frac{r^3}{C}\left[\frac{3\mathbf{b}.\mathbf{r}}{2r^2}\mathbf{r} - \mathbf{b}\right]. \tag{28}$$

where C is a constant that depends on the units that are chosen. If magnetic moment is in Am² and gradients are measured in nT/m, then C = 100 nTm/A. Similarly, given the location **r** = $r(n_1, n_2, n_3)$ of the dipole, the expressions for its gradient tensor elements can be rewritten as

$$\boldsymbol{\rho} = \begin{bmatrix} r^4 B_{xx} \\ r^4 B_{xy} \\ r^4 B_{xz} \\ r^4 B_{yy} \\ r^4 B_{yz} \end{bmatrix} = 3C \begin{bmatrix} 3n_1 - 5n_1^3 & n_2 - 5n_1^2 n_2 & n_3 - 5n_1^2 n_3 \\ n_2 - 5n_1^2 n_2 & n_1 - 5n_1 n_2^2 & -5n_1 n_2 n_3 \\ n_3 - 5n_1^2 n_3 & -5n_1 n_2 n_3 & n_1 - 5n_1 n_3^2 \\ n_1 - 5n_1 n_2^2 & 3n_2 - 5n_2^3 & n_3 - 5n_2^2 n_3 \\ -5n_1 n_2 n_3 & n_3 - 5n_2^2 n_3 & n_2 - 5n_2 n_3^2 \end{bmatrix} \begin{bmatrix} m_x \\ m_y \\ m_z \end{bmatrix} = \mathbf{N} \begin{bmatrix} m_x \\ m_y \\ m_z \end{bmatrix}, \tag{29}$$

where the LHS and the matrix **N** contain only known quantities. This overdetermined matrix equation can be solved in a least squares sense for the components of the moment in terms of these known parameters:

$$\mathbf{m} = \mathbf{N}^{+}\boldsymbol{\rho} = \left(\mathbf{N}^{\mathrm{T}}\mathbf{N}\right)^{-1}\mathbf{N}^{\mathrm{T}}\boldsymbol{\rho}. \tag{30}$$

The method of Nara et al. (2006) can be extended to uniquely determining the dipole location and moment vector from the gradient tensor and the second order gradient (which is a third rank tensor B_{ijk}) at a measurement point. Along a fixed direction $\hat{\mathbf{r}}$, B_{ij} is equal to a geometric factor, depending only on the magnitude and orientation of **m**, divided by r^4. From this it is easily shown that:

$$(\mathbf{r}.\nabla)B_{ij} = -4B_{ij}, \tag{31}$$

which gives an invertible linear relationship between **r**, and first and second order gradient tensor elements. The system of linear equations is overdetermined, so only a subset of the second order gradients is needed to obtain a unique location. For example, if the gradient tensor is measured along a profile segment, parallel to the *x* axis, the dipole location can be calculated directly from the tensor and its along-profile derivative, which can be calculated by numerical differentiation:

$$\mathbf{r} = \begin{bmatrix} x - x_0 \\ y - y_0 \\ -h \end{bmatrix} = -4 \begin{bmatrix} \frac{\partial B_{xx}}{\partial x} & \frac{\partial B_{xy}}{\partial x} & \frac{\partial B_{xz}}{\partial x} \\ \frac{\partial B_{xy}}{\partial x} & \frac{\partial B_{yy}}{\partial x} & \frac{\partial B_{yz}}{\partial x} \\ \frac{\partial B_{xz}}{\partial x} & \frac{\partial B_{yz}}{\partial x} & \frac{\partial B_{zz}}{\partial x} \end{bmatrix}^{-1} \begin{bmatrix} B_{xx} \\ B_{xy} \\ B_{xz} \end{bmatrix}. \tag{32}$$

The moment of the dipole can then be determined from **r** and the gradient tensor as shown above. Thus the dipole location and moment can be found from the first and second order gradient tensors at a single point. This result was inferred empirically by Wynn (1995) and later proved explicitly by him (Wynn, 1997). However that proof does not provide a method for determining the location and moment vector of the dipole. Wynn's (1995) method for inverting the gradient tensor and its along-profile gradients is quite complicated and involves a computationally intensive numerical search algorithm.

The second method presented here analyses data collected along a profile that passes near a dipole target. Unlike most other gradient tensor inversion techniques, this method can correct for contamination of the dipole signature by geological gradients or instrumental drifts, for example. Full details are given in Clark (2008).

Wilson (1985) showed that the scaled moment μ of a dipole, which is a particularly useful rotational invariant because it is independent of magnetic moment orientation and always peaks at the closest point of approach, can be calculated directly from the eigenvalues λ_i of the tensor. A sequence of calculated scaled moments along a profile can be deconvolved

and interference terms estimated and removed, but in practice it is easier and to process a related quantity, which yields more robust solutions. Define another invariant that is independent of the dipole orientation by $\nu = \sqrt{(\mu/3)} = \{[\sqrt{(-\lambda_2^2-\lambda_1\lambda_3)}]/3\}^{1/2}$, where λ_2 is the eigenvalue with the smallest absolute value. For a pure dipole signature ν is proportional to $\sqrt{m}/r^2$. Then at any point around an isolated dipole source ν can be estimated from the measured eigenvalues. In the presence of background gradients or interference from neighbouring bodies, at successive points $x = x_i$ (i = 1, 2,..., n) along a straight and level path, defined by $y - y_0$ = Y,

ν determined from the measured data can be modelled as:

$$\nu_i = \frac{\sqrt{Cm}}{(x_i - x_0)^2 + S^2} + \mathrm{a} + \mathrm{b}x_i + \mathrm{c}x_i^2, \tag{33}$$

where C is a constant that depends on the system of units, $S = \sqrt{(Y^2 + h^2)}$ is the slant distance from the point of closest approach to the dipole, $x = x_0$ is the point of closest approach, h is the depth of the dipole, a is the base level, and b, c are linear and quadratic terms that represent interference from other anomalies. The deconvolution problem is to solve for the unknown parameters x_0, S, m, a, b, c. This is equivalent to conventional Werner deconvolution (e.g. Ku and Sharp, 1983) of the TMI anomaly of a thin sheet.

Once the origin of x and slant distance are determined and the scaled moment, μ_i, and distance to source, r_i, at successive points are known, the measured gradient tensor elements can be modelled by:

$$B_{xx}^{(i)} = -\frac{\mu_i}{r_i^3}\left[2Lx_i^3 + 4M'Sx_i^2 - 3LS^2x_i - M'S^3\right] + \mathrm{a}_{\mathrm{xx}} + \mathrm{b}_{\mathrm{xx}}x_i + \mathrm{c}_{\mathrm{xx}}x_i^2, \tag{34}$$

with similar terms for the other four independent tensor elements, where the distances along the profile, x_i, are now with respect to an origin at the point of closest approach, $M' = MY - Nh$ is the direction cosine of the slant component of magnetization and a quadratic interference term is assumed for each component. The deconvolution problem is to solve for the unknown parameters L, M, N, Y, h and the interference terms a_{ij}, b_{ij}, c_{ij}. This is carried out in a similar way to the deconvolution of the invariant ν (Clark, 2008). At this stage it is recommended to remove the interference terms from the measured tensor elements and recalculate the eigenvalues and ν. Using the new estimates of x_0, S, m the deconvolution of the tensor elements can be repeated. The process is generally rapidly convergent, the revised interference terms become small and the source parameters become more precisely determined.

10 Conclusions and Further Work

- Four of the planar gradiometers met the required sensitivity performance operating in a shielded lab environment (refer Table 7) with the remaining two within 14 % of the target sensitivity at 10 Hz. The target gradient sensitivity of 2 pT /m / √Hz at 10 Hz (unshielded) was chosen based on an analysis of detection range for different size munitions (Clark et al., 2009). This gradient sensitivity gives a detection range of up to 4 m with a minimum dipole moment of 0.01 Am^2 (40 mm calibre). Note the issue of the sensitivity of the complete gradiometer in terms of the individual device sensitivities is somewhat complex (described in Section 6.8). However we can determine that as the gradient falls off as the fourth power of the distance, the detection range falls off as the 1/5 power, i.e. rather slowly [SERDP Report MM-1643]. If ALL the devices were 14% less sensitive than the specification, the detection range would only drop from 4 m to 3.87 m, i.e. by 3%. This degrading of performance is conservative, since most of the devices have better than the specified sensitivity.

- Three of the planar gradiometers met the required sensitivity performance operating in an unshielded environment whilst stationary in the Earth's field at 10 Hz.

- Note the sensitivity of all of the gradiometers was well below the required sensitivity at 30 Hz in a shielded environment (an average of 32 % below)

- While in motion, the common mode response of the planar gradiometers masked the intrinsic sensitivity.

- Common mode rejection of the planar gradiometers was determined to be in the range of 10^2 – 10^3. Variations between the individual gradiometer common mode performance and that actually achieved by each gradiometer in the full system remain unresolved.

- Calibration in the laboratory was successful for determining compensation coefficients for laboratory based experiments. These coefficients did not suffice for field operation due to significant changes in the local background gradient field.

- Calibration in the local gradient field environment is essential to improve the performance of the HTSG system.

- A portable calibration setup is required to enable accurate determination of the compensation coefficients.

Possible alternatives to the initial laboratory calibration technique are under consideration. For example a spinning magnet, placed at differing several source-sensor separations, should provide sufficient data to uniquely separate the common mode and gradient signals and thus provide more accurate calibration and referencing coefficients for the compensation algorithm.

- Investigate the use of field cancellation techniques to reduce the sensitivity of the HTSG to movement in the Earth's field.

Measurements of the uncompensated common mode response in the gradiometer outputs due to small tilts, of about 1°, in the full geomagnetic field indicate that the required sensitivity specification can be met if the field seen by the devices is substantially reduced. If motions can be restricted to 5°, with associated uncompensated field variations less than ~5000 nT, averaging 5 samples at intervals of 0.02 s will give rms noise of ~2 pT/m, ten times a second, provided a field cancellation factor of ~500 can be achieved.

Field cancellation factors of this order can probably be achieved by a relatively open feedback coil geometry, for example triaxial Helmholtz or Rubens coil configurations. The requirements for field uniformity across the instrument are not too stringent, provided the responses of the individual devices are calibrated in terms of measured feedback currents. The requirements for field cancellation can be relaxed somewhat if the CMRR of the devices is improved, which can probably be achieved by improvements in design or fabrication.

Provisions have been made to increase the future gradient sensing capability of the planar gradiometers further by at least a factor of two. Increasing the gradiometric antenna outer dimensions to 48 mm x 48 mm (Design D shown in Figure 84), the geometrical area of each pickup loop area A_P increases from 460 mm^2 to 1152 mm^2 (increase of 150 %). The use of the diagonal increases the baseline to ~ 31.8 mm (increase of 41 %). Figure 83 shows the comparative dimensions of both design C and D. The input coil dimensions remain unchanged. Although this structure has not been fully modelled, a rough estimate suggests we have the potential to improve the gradient sensitivity by as much as ~100% provided we have a constant flux noise. This larger area gradiometer can easily be incorporated in the current pyramid structure with no major modification required.

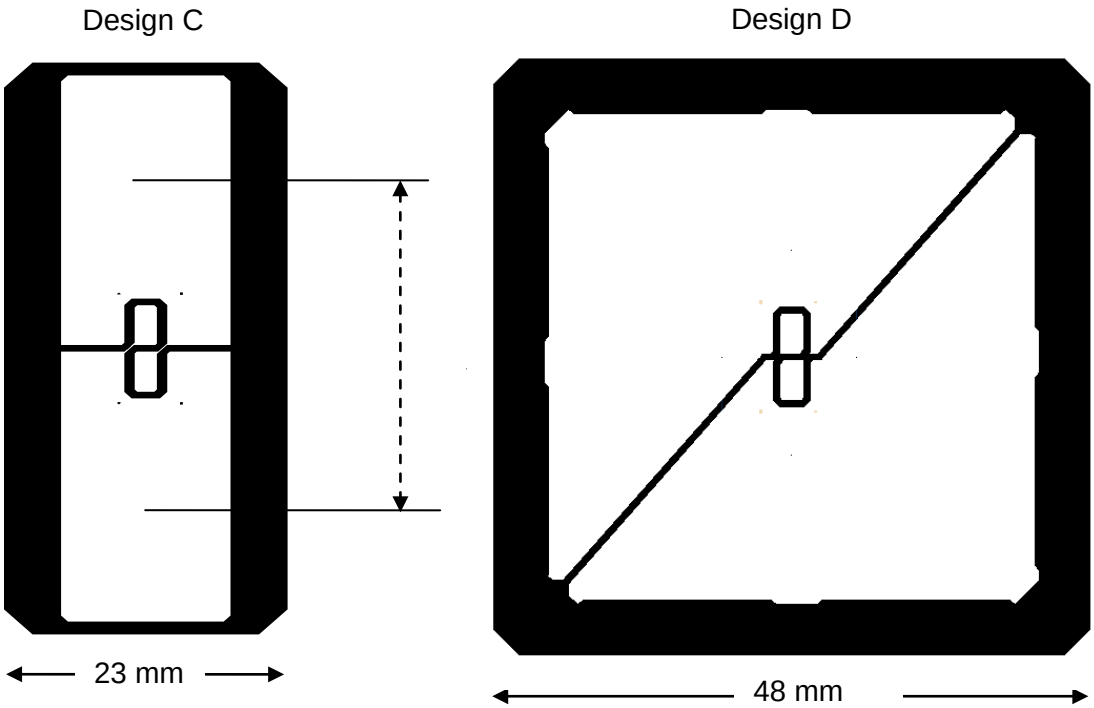

Figure 84 Comparison of the gradiometric antenna design (C) used in the tensor gradiometer system and a newly designed antenna with improved baseline and effective area.

REFERENCES

Clark, D., Young, J., and Billings, S., 2009. SERDP MM-1661 White Paper: Stand-off distance and detection.

Clark, D.A., 2010. Correction of electric and magnetic fields and gradients measured within and around an insulating sensor capsule in seawater. OCEANS '10 IEEE Sydney, Sydney, Australia.

Clark, D., 2008. Magnetic Gradient Tensor Measurement using an Array of Planar Gradiometers on a Pyramidal Prism, CSIRO Report EP101863.

Clark, D.A., Young, J.A., and Schmidt, P.W., 2009. Magnetic tensor gradiometry in the marine environment: correction of electric and magnetic field and gradient measurements in a conductive medium and improved methods for magnetic target location using the magnetic gradient tensor. MARELEC 2009, Stockholm, Sweden.

Clem, T.R., Overway, D.J., Purpura, J.W., Bono, J.T., Koch, R.H., Rozen, J.R., Keefe, G.A., Willen, S., and Mohling, R.A., 2001. High-T_c SQUID gradiometer for mobile magnetic anomaly. *11*, 1, 871-875.

Czipott, P.V., 2002. Magnetic Detection and Tracking of Military Vehicles, http://handle.dtic.mil/100.2/ADA409217.

Eschner, W. and Ludwig, W., 1995a. Planar gradiometers arranged on non-parallel surfaces for determination of a gradient tensor of a magnetic field. U.S. Patent No. 5469056.

Eschner, W. and Ludwig, W., 1995b. Planar gradiometers arranged on non-parallel surfaces for determination of a gradient tensor of a magnetic field. US 5469056.

Faley, M.I., Poppe, U., and Urban, K., 1997. DC-SQUID magnetometers and gradiometers on the basis of quasiplanar ramp-type Jospehson junctions. IEEE Transactions on Applied Superconductivity, *7,* 3702.

Foley, C.P., Mitchell, E.E., Lam, S.K.H., Sankrithyan, B., Wilson, Y.M., Tilbrook, D.L., and Morris, S.J., 1999. Fabrication and characterisation of YBCO single grain boundary step edge junctions. IEEE Transactions on Applied Superconductivity, *9,* 4281-4284,

Humphrey, K.P., Horton, T.J., and Keene, M.N., 2005. Detection of mobile targets from a moving platform using an actively shielded, adaptively balanced SQUID gradiometer. IEEE Transactions on Applied Superconductivity, *15,* 753-756.

Keene, M.N., Humphrey, K.P., and Horton, T.J., 2005. Actively shielded, adaptively balanced SQUID gradiometer system for operation aboard moving platforms. IEEE Transactions Applied Superconductivity, *15,* 761-764.

Kumar, S., Perry, A.R., Moeller, C.R., Skvoretz, D.C., Ebbert, M.J., Ostrom, R.K., Bennett, S.L., and Czipott, P.V., 2004. Real-time tracking magnetic gradiometer for underwater mine detection. OCEANS '04. MTS/IEEE TECHNO-OCEAN '04 *2*, 874-878.

Peiselt, K., Schmidt, F., Linzen, S., Anton, A.S., Hübner, U., and Seidel, P., 2003. High-T_c

dc-SQUID gradiometers in flip-chip configuration. Superconductor Science and Technology, *16,* 1408-1412.,

Stolz, R., Zakosarenko, v., Schulz, M., Chwala, A., Fritzsch, L., Meyer, H.-G., and Köstlin, E.O., 2006. Magnetic full-tensor SQUID system for geophysical applications. The Leading Edge, *25,* 178-180.

Tian, Y.J., Linzen, S., Schmidl, F., Dorrer, L., Weidl, R., and Seidel, P., 1999. High-T_c directly coupled direct current SQUID gradiometer with flip-chip flux transformer. Applied Physics Letters, *74,* 1302-1304.

SkyResearch & CSIRO, SERDP Report MM-1643 "Precision Geolocation of Active Electromagnetic Sensors Using Stationary Magnetic Sensors", page 127, equation 47.

Publication List

Journal articles

1. Keenan, Shane, Blay, Kyle, Romans, Ed. Mobile magnetic anomaly detection using a field-compensated high-Tc single layer SQUID gradiometer. Superconductor Science and Technology. 2011; 24(8):085019.

2. Keenan, S., Young, J. A., Foley, C. P., Du, J. A high-Tc flip-chip SQUID gradiometer for mobile underwater magnetic sensing. Superconductor Science and Technology. 2010; 23(2):025029.

3. Young, J. A., Keenan, S. T., Clark, D. A., Leslie, K. E., Sullivan, P., Fairman, P., et al. A superconducting magnetic tensor gradiometer for underwater UXO detection. Exploration Geophysics. 2010.

Conference papers/Conference proceedings

1. Keenan, S., Young, J. A., Cusack, P., Clark, D., Foley, C. P. OCEANMAG - A fully mobile magnetic gradient tensor measurement system [Abstract]. In: CSIRO Materials Science and Engineering, Lindfield, N.S.W./, editor/s. Applied Superconductivity Conference 2010 (ASC 10); August 1-6, 2010; Washington D.C.. 2010.

2. Young, J. A., Keenan, S. T., Clark, D. A., Sullivan, P., Billings, S. D. Development of a high temperature superconducting magnetic tensor gradiometer for underwater UXO detection. In: CSIRO Materials Science and Engineering, Lindfield, N.S.W./Sky Research Inc., editor/s. OCEANS '10 IEEE Sydney Conference and Exhibition; May 24-27, 2010; Sydney, N.S.W.. 2010.

3. Young, Jeanne, Clark, David. Magnetic tensor gradiometry in the marine environment. In: ICEAA'10; September 20-24, 2010; Sydney, Australia. IEEE; 2010. 701-704.

4. Billings, S., Young, J. A., Keenan, S., Clark, D. MM-1661: Superconducting magnetic tensor gradiometer system for detection of underwater military munitions [Abstract]. In: CSIRO Materials Science and Engineering, Lindfield, N.S.W./, editor/s. SERDP & ESTCP's Partners in Environmental Technology Symposium 2009; December 1-3, 2009; Washington D.C.. 2009.

5. Keenan, S., Du, J., Foley, C. P., Young, J. A. Long baseline high-Tc Planar SQUID gradiometers in flip-chip configuration using step edge junctions for mobile underwater magnetic sensing [Extended Abstract]. In: CSIRO Materials Science and Engineering,

Lindfield, N.S.W./, editor/s. International Superconductive Electronics Conference (ISEC 2009); June 16-19, 2009; Fukuoka, Japan. 2009.

6. Billings, S., Foley, C. P., Young, J. A., Clark, D., Keenan, S., Wright, D. Total-field and SQUID magnetometer sensors for underwater UXO detection. In: CSIRO Materials Science and Engineering, Lindfield, N.S.W./, editor/s. UXO/Countermine/Range Forum 2009; August 24-27, 2009; Orlando, Florida. 2009.

7. Keenan, S., Foley, C. P., Young, J. A. HTS planar SQUID gradiometer based magnetic gradient tensor system. In: CSIRO Materials Science and Engineering, Lindfield, N.S.W./, editor/s. Euroflux Conference; 20-23 September, 2009; Avignon, France. 2009.

8. Young, J. A., Keenan, S. T., Clark, D. A., Leslie, K. E., Sullivan, P., Fairman, P., et al. A superconducting magnetic tensor gradiometer for underwater UXO detection [Abstract]. In: CSIRO Materials Science and Engineering, Lindfield, N.S.W./Sky Research Inc., editor/s. ASEG-PESA 21st Conference and Exhibition; August 22-26, 2010; Sydney, N.S.W.. 2010.